Multi–instrument studies of heavy ion solar energetic particle transport

Peter Zelina

A thesis submitted in partial fulfilment of
the requirements for the degree of
Doctor of Philosophy

Jeremiah Horrocks Institute for Mathematics, Physics and Astronomy
University of Central Lancashire

September 2017

Declaration

I declare that all the work presented in this thesis was carried out at the Jeremiah Horrocks Institute for Mathematics, Physics and Astronomy at the University of Central Lancashire.

I declare that during the preparation of this thesis, I have not been a registered candidate or enrolled student for another award at another University or other academic or professional institution.

I declare that none of the material within this thesis has been used for submission to any other institution for an academic award. Any data contained within this thesis that are not my own are clearly cited in the text and the bibliography.

Peter Zelina

Abstract

In this thesis, an analysis of solar energetic particle (SEP) data from multiple instruments onboard the ACE, SOHO and STEREO spacecraft is presented. The temporal variation and the dependence of heavy ion abundances on solar longitude were studied and quantitatively characterised during SEP events between 2006 and 2016.

Ionic abundances vary over the duration of SEP events, e.g. Fe/O often shows a decrease over time. This behaviour was identified as a common characteristic within the data. The time variation of 36 different ionic pairs was studied for a number of SEP events. The fit constant describing time evolution was found to show ordering by the value of S, given e.g. for Fe/O by $S_{\mathrm{Fe/O}} = (M/Q)_{\mathrm{Fe}} \big/ (M/Q)_{\mathrm{O}}$, where M is the mass number and Q the charge number. The ionic ratios with $S > 1$ decreased over time and those with $S < 1$ showed increases, while ratios with a large S decayed at a higher rate. Anomalous behaviour of ratios involving protons was identified in several events.

The longitudinal dependence of Fe/O simultaneously observed by multiple spacecraft at 1 AU was studied in 12 SEP events. The event–averaged Fe/O values observed by spacecraft at different longitudes varied within a single event, but this variation was less significant than the event–to–event variation. Although the longitudinal dependence was a complicated one, in some events the Fe/O values were higher at a remote observer.

The temporal evolution of heavy ion ratios, which was studied quantitatively for a number of ionic pairs, is consistent with an M/Q–dependent interplanetary trans-

port mechanism. The observed longitudinal dependence of event–averaged Fe/O, where higher Fe/O values are observed at a spacecraft that is not well magnetically connected to the source region, cannot be fully explained by the two–class paradigm for classification of SEP events.

Table of Contents

List of Tables

List of Figures

List of Acronyms

ACE Advanced Composition Explorer

AR active region

AU astronomical unit

CME coronal mass ejection

CPA central position angle

dA CME angular width

DOY day of year

DSA diffusive shock acceleration

EPAM Electron, Proton, and Alpha Monitor

EPD Energetic Particle Detector

ERNE Energetic and Relativistic Nuclei and Electron

ESP energetic storm particle

EUV extreme ultraviolet

GLE ground–level enhancement

GOES Geostationary Operational Environmental Satellite

HED High Energy Detector

HET High Energy Telescope

HXR hard X–ray

ICME interplanetary coronal mass ejection

IMP–8 Interplanetary Monitoring Platform–8

IPM interplanetary medium

ISEE–3 International Sun/Earth Explorer 3

LASCO Large Angle and Spectrometric Coronagraph Experiment

LED Low Energy Detector

LET Low Energy Telescope

LMSAL Lockheed Martin Solar and Astrophysics Laboratory

MHD magnetohydrodynamic

MPA measured position angle

NOAA National Oceanic and Atmospheric Administration

PLASTIC Plasma and Suprathermal Ion Composition

RHESSI Reuven Ramaty High Energy Solar Spectroscopic Imager

SAMPEX Solar, Anomalous, and Magnetospheric Particle Explorer

SDA shock drift acceleration

SEP solar energetic particle

SEPICA Solar Energetic Particle Ionic Charge Analyzer

SIS Solar Isotope Spectrometer

SIT Suprathermal Ion Telescope

SOHO SOlar and Heliospheric Observatory

STA STEREO Ahead

STB STEREO Behind

STEREO Solar TErrestrial RElations Observatory

SWEPAM Solar Wind Electron, Proton, and Alpha Monitor

SXR soft X–ray

TIROS Television Infrared Observation Satellite

ULEIS Ultralow–Energy Isotope Spectrometer

ULEZEQ UltraLow Energy Z-E-Q Analyzer

Acknowledgements

In the first instance, I would like to thank everyone that supported me in any way to finally see the day for the submission of my thesis.

Most notably, I would like to thank my supervisor Dr. Silvia Dalla, who patiently guided me through every step of the study. Without her insightful advice I certainly would not be here writing the acknowledgements of this thesis.

In addition, I would like to thank my second supervisor Dr. Daniel Brown and research degree tutor Dr. Tim Cawthorne, for the help and support they provided.

Next, I would like to thank to the members of the solar group: Dr. Timo Laitinen, Dr. Mike Marsh, Dr. Markus Battarbee, Dr. Danielle Bewsher, Dr. Stephane Regnier, Andrew Walker, Danny Lee and Bill Swalwell, for numerous scientific discussions we held over the years and their constructive feedback to my work before it was presented to the world.

In particular, I would like to thank to Don Doran, who has been a good friend to me and made my time while researching solar physics more enjoyable. Additionally, I would like to Don for immense amount of time and efforts spent while proofreading this thesis.

I would also like to thank to all members of the Jeremiah Horrocks Institute and the staff at the University of Central Lancashire for creative environment, in which it was pleasure to work, and assistance they provided. Namely, I would like to thank professor Derek Ward–Thompson, Mrs. Nuala Jones, Dr. Giovanni Natale, Dr. Shane O'Hehir, Dr. Maider Sancho Miranda, Mr. David Capstick, Mr. Rick Collins and Mrs. Clare Altham.

A part of this thesis was published in *The Astrophysical Journal* and I would like to thank the co–authors of the paper, Dr. Christina Cohen and Dr. Richard Mewaldt at Caltech, for interesting discussions and their input while writing the manuscript.

I would like to thank the examiners professor Gordon Bromage and Dr. Eduard Kontar for their constructive and instructive suggestions to the thesis at the viva voce examination.

Last but not least, I would like to express my sincerest thanks to my wife, my mother and father, and my sister, who wholeheartedly supported me throughout my career.

I would like to acknowledge the support from the Jeremiah Horrocks Institute at the University of Central Lancashire through a PhD studentship.

In this study I used scientific data that are publicly available. Therefore, I would like to thank to the ACE SIS, STEREO LET, HET and SOHO ERNE instrument teams and the ACE and STEREO Science Centers for maintaining and releasing the data. The CDAW CME catalog is generated and maintained at the CDAW Data Center by NASA and The Catholic University of America in cooperation with the Naval Research Laboratory. SOHO is a project of international cooperation between ESA and NASA.

Chapter 1

Introduction

This thesis presents research undertaken during my PhD study at the Jeremiah Horrocks Institute at University of Central Lancashire in Preston, UK. It contains a summary of topics regarding solar energetic particles (SEPs) and presents the results of analysis of SEP data from particle instruments onboard multiple spacecraft. The thesis also encompasses a brief description of solar phenomena that are causally related to SEPs, as well as acceleration and transport of SEPs in the interplanetary medium (IPM).

The main concepts within SEP science and the state of the art are presented in the Introduction (Chapter 1), and the current knowledge about SEP observations and modelling in Chapter 2. Chapter 3 consists of the description of SEP observations and the heavy ion event list. In Chapter 4 the SEP observations are presented focussing on heavy ion SEP events observed simultaneously by multiple spacecraft. Chapter 5 contains analysis of the time dependence of heavy ions and the ordering by particles' mass–to–charge ratio, m/q. Conclusions and suggestions for future work are presented in Chapter 6. Appendix A contains analysis of 4 additional SEP events observed by multiple spacecraft, similar to those presented in Chapter 3. Appendix B contains a copy of the article by Zelina et al. (2017) published in *The Astrophysical Journal*. Appendix C contains a copy of the article by Dalla et al. (2017b) published in *Astronomy & Astrophysics*.

In the present chapter the main properties of SEPs are introduced (Section 1.1), as well as those of the solar phenomena responsible for their acceleration, solar flares and coronal mass ejections (Section 1.2). The role of acceleration and transport mechanisms is introduced in Section 1.3, and heavy ion SEP events in Section 1.4. The motivation for this work and its objectives are presented in Section 1.5.

1.1 Solar energetic particles

Solar energetic particles are energetic ions and electrons detected in the space environment that are observed as increases in particle flux. SEPs are not observed all the time and are usually associated with solar activity. Solar flares and shock waves driven by coronal mass ejections (CMEs) are known to accelerate particles to high kinetic energies up to relativistic energies of e.g. several GeV/nuc for ions and tens of MeV for electrons. A typical SEP energy range for protons starts above a hundred keV. SEPs are different in terms of energies from the solar wind, a highly variable flow of charged particles, with typical energies of several keV, and the suprathermal tail of solar wind at tens keV. Energetic particles released into the IPM propagate through it and when detected, they give rise to SEP events (Kallenrode 2004; Reames 1999).

SEP events are an important component of space weather and can negatively impact human activities, including causing space satellite failure and high–frequency radio blackouts over polar regions. Astronauts at low Earth orbit can receive a harmful dosage of radiation, while high–altitude flight crew and passengers may be exposed to an increased radiation risk. A more comprehensive overview of the space weather phenomena and effects can be found in textbooks, e.g. by Moldwin (2008).

SEP time profiles measured at 1 astronomical unit (AU) depend on their sources, i.e. the acceleration processes involved, and on conditions of the IPM, through which the particles propagate. Properties of the intensity versus time profiles, such as onset time, time–to–maximum intensity, rise and decay phase profiles, carry information

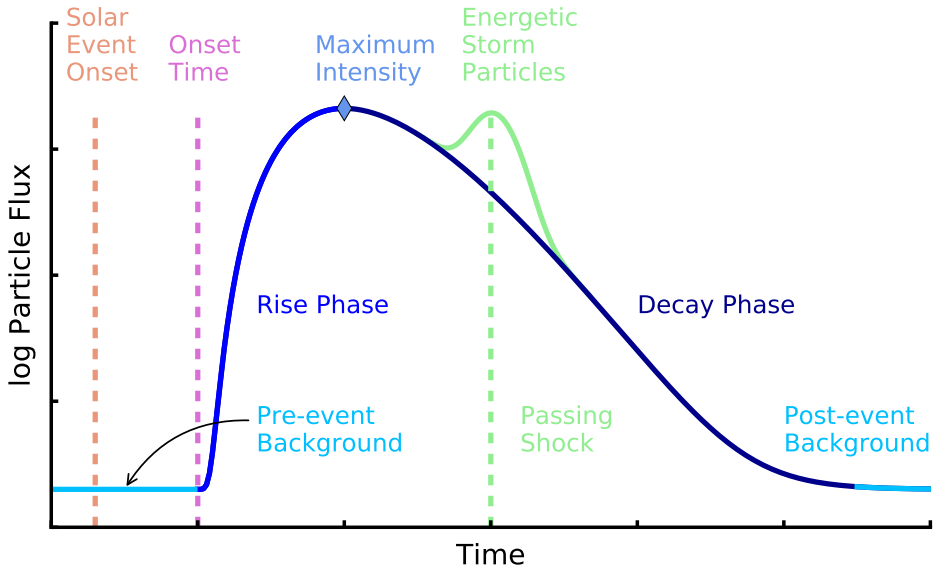

Figure 1.1: A cartoon of time profile of an SEP event (not to scale). The main timeline of an SEP event includes: start of a flare at the Sun (orange), start of a particle increase (pink) above pre–event background (light blue), rise phase (blue) to maximum flux, which can last several hours, and decay phase (dark blue), which can take several days. Particle increase associated with a passing shock (green) can sometimes be observed that peaks near the time of shock passing the observer. After Turner (2000).

about the origin and transport of SEPs. Therefore, SEPs tell us about processes on the Sun and local conditions in the IPM.

Figure 1.1 shows a sketch of time profile of an SEP event. Particles are detected after an associated solar eruption occurs at the Sun. The time between the start of a flare and the start of observed particle increase (the onset time) is called propagation delay. The SEP intensity increases until it reaches maximum, a time period called rise phase. The time between onset and peak intensity is called time to maximum. After the maximum, the intensity decreases and returns back to background levels. The decay phase of an SEP event can take several days depending on the energy of particles. When an interplanetary shock passes the observer, SEP intensity may increase near its passage at the observer, a phenomenon called energetic storm particle (ESP) event.

The shape of SEP intensity–time profiles largely depends on the energy of the particles. For example, SEPs at energies above 100 MeV often do not display a shock–

related particle increase, in contrast to SEPs at lower energies. For some events the onset time can be quite long (24 hours or more), especially when the eruption occurs behind the solar limb as seen by the observer. The onset time and the time to maximum intensity can also be quite short, e.g. minutes to several hours, particularly in events when the eruption occurs in the western hemisphere. Such short onset times and the generally unpredictable nature of the solar eruptions pose a serious challenge to space weather forecasting.

History of SEP research

Particles associated with solar activity were first observed in 1940s by Lange & Forbush (1942). The detected particles were linked to solar flares, observed as short–duration brightenings on the solar disk, several years later by Forbush (1946). These particles as detected by neutron monitors are now known as ground–level enhancements (GLEs) and are understood to be secondary particles of GeV energy protons that collide with particles in the atmosphere (Meyer et al. 1956; Cliver 2008). Signatures preserved as isotopic enhancements in deep layers of ice and in tree rings, show a record of past GLE events, (e.g. Usoskin et al. 2006), and tell us that extreme SEP and GLE events occur on timescales of hundreds to thousands of years.

In the 1950s and early 1960s high–altitude balloons and rockets were used to measure cosmic rays. SEPs, then known as *solar cosmic rays*, together with galactic and anomalous cosmic rays, were recognised as a component of the cosmic ray spectrum. With the advancement into the space age, instruments to measure particles were incorporated within spacecraft placed in Earth orbit in order to sample SEPs in situ. Such instruments were launched onboard many satellite missions, including the Television Infrared Observation Satellite (TIROS) (TIROS–1 launched in 1960), a series of Geostationary Operational Environmental Satellites (GOES) (GOES–1 in 1975, GOES–16 in 2016), and others. Notable current missions include the SOlar and Heliospheric Observatory (SOHO) (1995), the Advanced Composition Explorer

(ACE) (1997), and the Solar TErrestrial RElations Observatory (STEREO) spacecraft (2006), all of which, except for STEREO Behind, are still operational.

Based on observations of slow–drifting type II radio bursts, Wild et al. (1963) proposed interplanetary magnetohydrodynamic (MHD) shocks as a particle acceleration mechanism. Fast–drifting type III radio bursts associated with solar flares were recognised as a signature of electrons escaping on open magnetic field lines to the IPM (Lin 1970).

Later in the 1970s, a white light telescope with an occulting disk, a setup known as the coronagraph, was placed onboard the Skylab space station. Transient features were observed in coronagraph images and a connection was made between interplanetary shocks and the newly discovered CMEs (Tousey 1973; Gosling et al. 1974). CMEs were understood to be the drivers of the interplanetary MHD shocks. A long–lasting debate started during this period about the role of flares and CMEs in generating SEPs, known as *The Solar Flare Myth* (Gosling 1993).

Two class paradigm of SEPs

A two–class paradigm for the classification of SEP events was developed in the 1980s and 1990s. A diagram illustrating the paradigm is shown in Figure 1.2, which describes the two particle acceleration mechanisms thought to be at play: magnetic reconnection in compact solar flares for impulsive events and CME–driven interplanetary shocks for gradual events. Panel (a) in Figure 1.2 shows SEPs accelerated by a CME–driven shock and injected onto magnetic field lines over a wide range of longitudes. Panel (b) in the same figure shows SEPs injected over a narrow region populating magnetic field lines with good magnetic connection to the flare. Hence, the paradigm recognises 2 classes of SEP events, *gradual* and *impulsive* events that have different properties and proposed acceleration mechanisms. Under the paradigm, SEPs that propagate away from the Sun quickly become focussed and propagate along magnetic field without significant perpendicular transport. The paradigm is described and summarised by Reames (1999).

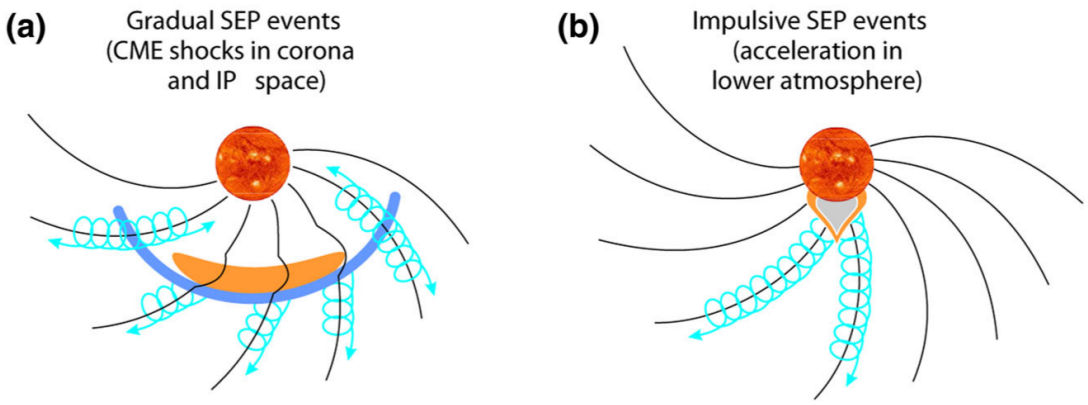

Figure 1.2: A diagram of the two class paradigm of SEP events. Panel (a) shows a schematic diagram of a gradual event, and panel (b) of an impulsive event. Taken from Desai & Giacalone (2016).

Impulsive SEP events are thought to be associated with solar flares. These are short–lived SEP events with fast rise and decay phases, which typically last less than a day. Impulsive events are rich in ^{3}He, Fe, and electrons. The isotopic ratio ^{3}He/^{4}He can be 1000 times larger and Fe/O 10 times larger, than typical coronal composition, 5×10^{-4} for ^{3}He/^{4}He and ~ 0.1 for Fe/O (Reames 1999). The average Fe charge state can reach values as high as $Q_{\mathrm{Fe}} \approx 20$ (Klecker et al. 2006b; Luhn & Hovestadt 1987), a signature of hot, 10^7 K plasma inside the flaring region. Acceleration is most likely a result of reconnection processes in the eruptive phase of solar flares happening low in the corona. Type III radio bursts, associated with flares, are a signature of electrons released into space. Initially, the longitudinal width of impulsive SEP events was thought to be narrow because they were observed only for source regions on the western hemisphere of the solar disk, typically located at 45–60 ° west of the central meridian (Reames 1999).

Gradual SEP events are characterised by large proton intensity increases, which can last as long as 15 days. Compared to impulsive events, average charge states of Fe ions are lower in gradual events, for example $Q_{\mathrm{Fe}} \approx 14$, a fact ascribed to the lower temperature of the source plasma from the corona. Mean ionic abundances in gradual events are similar to the solar wind ones (Reames 1998), but can vary more significantly event to event than typical solar wind ratios. Gradual SEP events

can be observed over a wide span of longitudes and can originate from eastern and western longitudes on the solar disk, and in some cases from behind the solar limb. Gradual events are often accompanied by a CME–driven shock. The expanding shock is thought to be responsible for SEP acceleration. The acceleration of SEPs occurs at the extended shock front expanding in longitude. A shock, within which SEPs are injected over a broad range of magnetic field lines, is thought to explain the wide longitudinal extent of gradual events in the heliosphere. Slow–drifting type II radio bursts are a signature of a shock propagating in the IPM accelerating particles.

In large SEP events, solar flares are often accompanied by CMEs and both type II and III radio bursts are observed. In recent years, studies using multiple spacecraft showed that some signatures of impulsive events, e.g. high Fe and ^{3}He abundances, can be observed over regions widely separated in longitude in events that would otherwise be classified as gradual (Wiedenbeck et al. 2013; Cohen et al. 2014). Therefore, the distinction between gradual and impulsive events has become less clean–cut in recent years (Kallenrode 2003; Cane & Lario 2006).

1.2 Solar flares and coronal mass ejections

Solar flares and CMEs, both having magnetic nature, can occur independently. In solar eruptions that produce large SEP events typically both a flare and a CME are present (Hudson 2011).

Both flares and CMEs are known to accelerate SEPs, therefore, SEPs can be used to study them. At the same time, the parameters of flares and CMEs determine the SEP intensity time profiles detected by an observer. The occurrence rate and strength of solar flares and CMEs varies with the solar cycle and is correlated with the solar sunspot number.

Magnetic energy released during the reconnection of magnetic field is dissipated and can supply the energy of flares, the kinetic energy of CMEs, and the thermal and non–thermal processes (Aschwanden et al. 2014, 2016, 2017). The total energy

budget of a solar eruption, including the flare and CME component, can be as large as 10^{25} J (Vourlidas et al. 2000).

Solar flares

A flare is a manifestation of magnetic reconnection in the solar corona (Parker 1957; Sweet 1958), understood within the framework of the standard theory of solar flares, the CSHKP model (Carmichael 1964; Sturrock 1966; Hirayama 1974; Kopp & Pneuman 1976). This model is based on a 2D geometry, but more recently magnetic reconnection processes in 3D topologies have been explored (Shibata et al. 1995; Priest & Forbes 2002; Dalla & Browning 2005).

Charged particles in solar flares are accelerated via magnetic reconnection, where energy stored in the magnetic field is transformed into kinetic energy of particles. During magnetic reconnection, a plasma bound in a closed magnetic loop is destabilised by the motion of photospheric footpoints and rises up into the corona. When plasmas with different frozen–in magnetic field are pressed together, magnetic fields reconnect, and plasma that slowly inflows into the reconnection region is accelerated and released as hot plasma jets. Energised electrons that propagate towards the chromosphere along loop magnetic fields decelerate in the denser plasma. Electrons colliding with ambient ions emit hard X–ray (HXR) via bremsstrahlung and lose kinetic energy via electron–electron Coulomb collisions (Kontar et al. 2014). In some cases, the HXR radiation can originate at the looptop, which is considered a direct signature of magnetic reconnection taking place (Masuda et al. 1994; Kontar et al. 2011). Simões & Kontar (2013) found that the production rate of energetic electrons above 30 keV is several times higher in the looptop than at the chromospheric footpoints. Heated plasma from the footpoints fills the coronal loop via chromospheric evaporation and emits thermal soft X–ray (SXR) (Fletcher et al. 2011).

Several features can be identified in the time profiles of solar flares (Hudson 2011). In the early phase of a solar flare, preheating of the plasma occurs showing soft and hard X–ray signatures. The impulsive phase is characterised by hard X–ray and

microwave radiation. The hard X–ray time profile roughly coincides with the time derivative of the soft X–ray time profile, a phenomenon known as the Neupert effect (Neupert 1968). The gradual phase follows with the decay of soft X–ray flux that can take several hours. Emission in the extreme ultraviolet (EUV) and optical part of the spectrum (e.g. H_α flares) due to thermal heating of plasma can be observed in coronal loops. Therefore, brightening from solar flares can be observed across the entire electromagnetic spectrum (Fletcher et al. 2011).

Electromagnetic waves in the microwave part of the spectrum are emitted by the gyrosynchrotron motion of electrons, gyrating around magnetic field lines in the coronal loop. The peak of the microwave spectrum can be used to infer the local value of magnetic field strength, which unlike photospheric magnetic field cannot be measured directly.

Energetic electrons propagating in the IPM can excite Langmuir waves, high–frequency plasma oscillations, emitting radio waves near the local electron plasma frequency (Melrose 1985) that are observed as type III radio bursts. Radio burst drifting towards high (low) frequencies are a signature of electrons accelerated towards (away from) the Sun. The frequency of Langmuir waves depends on the local electron density, therefore the radio waves can be used to infer the local electron density along the propagating electron beam.

Classification of solar flares is currently based on the GOES soft X–ray peak flux in the $1 - 8$ Å wavelength band. The flare class is denoted in ascending order by letters A, B, C, M and X, where each class has flux 10 times higher than the preceding class and X class corresponds to a soft X–ray flux of $10^{-4}\,\mathrm{W\,m^{-2}}$. The numeral after the letter is a multiplier between 1.0 and 9.9. The strongest flare ever recorded occurred on 4 November 2003 and it is estimated to have been of X28 class (CDAW CME Catalog), but the SXR detector was saturated at X20. The flare associated with the 1859 Carrington event is estimated to be an X45 class flare (Mann 2015). Current spacecraft missions that are primarily used to study solar flares are the Reuven Ramaty High Energy Solar Spectroscopic Imager (RHESSI)

(Lin et al. 2002) and Hinode (Kosugi et al. 2007).

Coronal mass ejections

Before technology advances permitted direct observations of coronal mass ejections, the Sun–Earth connection was understood in the context of solar flares that were followed by geomagnetic disturbances and aurorae, such as the one associated with the 1859 Carrington event (Carrington 1859; Hodgson 1859). Features on the solar disk and in the corona observed during solar eclipses, e.g. sunspots, prominences and streamers, were loosely considered to be the precursors of solar eruptions.

So called *Forbush decreases* of cosmic ray intensity observed by Forbush (1937) were later explained by the expulsion of the cosmic rays by transient magnetic structures in the vicinity of the Earth (Alexander et al. 2006). But after CMEs were directly observed using the Skylab coronagraph and further spacecraft missions, they were understood to be fast transients of coronal plasma that could be the driver of the interplanetary MHD shocks (Parker 1961; Wild et al. 1963). Their properties were quantitatively analysed for the first time by Gosling et al. (1974).

The origin of CMEs is usually associated with active regions, but CMEs can be triggered by instabilities of the underlying magnetic field leading to an eruption of a prominence as well. They are best observed by spaceborne coronagraphs, which detect photons scattered off the electrons within the CME. The CME structure usually has 3 parts: an outer bright front, an underlying dimmer cavity, and an embedded bright core. Halo CMEs, forming a circumsolar ring on coronagraph images, are considered CMEs heading towards or away from the observer, although in some cases multiple spacecraft widely separated in longitude can observe the same CME as halo (Kwon et al. 2015).

The fastest CMEs can in some cases exceed speeds of 3000 km/s (CDAW CME Catalog), but typical speeds of fast CMEs near the Sun are lower, between 800 and 2000 km/s, corresponding to a travel time to the Earth of 1–3 days. CMEs can drive a magnetohydrodynamic shock and are often associated with type II radio

bursts, which is a signature of the shock, but there is not one to one correlation for its presence. In situ measurements of passing interplanetary coronal mass ejections (ICMEs) often show a rapid change in the magnetic field vector, especially when a shock is present. A more comprehensive summary of CME properties can be found e.g. in Hudson et al. (2006); Schwenn et al. (2006); Wimmer–Schweingruber et al. (2006); Zurbuchen & Richardson (2006).

The nature of the link and causality between solar flares and CMEs is under intensive scientific debate, but according to Hudson (2011) there is 100 % correlation between CMEs and flares above X2 class.

Currently the only operational space–based coronagraphs are placed on the SOHO and STEREO Ahead spacecraft but future missions to the L5 point in addition to L1 would be advantageous and are under consideration.

1.3 SEP acceleration and transport

Solar energetic particles are not observed at all times, but they are transient phenomena associated with solar flares and CMEs. SEPs are accelerated via magnetic reconnection in solar flares and by CME–driven shocks, and propagate through the IPM. SEPs can be detected by an observer at 1 AU as soon as tens of minutes after the flare. The timing of the fastest particles in SEP and GLE events suggests they are accelerated during a short time period during the flare eruption and while the associated CME–driven shock is still near the Sun (Kahler 1994; Roussev et al. 2004; Klecker et al. 2006a). SEP acceleration is a subject of great research interest and the basic concepts are covered in textbooks about solar and heliospheric physics, e.g. Kallenrode (2004), or scientific review papers, e.g. Desai & Giacalone (2016).

1.3.1 SEP acceleration

SEPs associated with solar flares are thought to be primarily accelerated via magnetic reconnection, which has also been subject to modelling efforts (e.g. Dalla &

Browning 2005; Threlfall et al. 2015). The electric field created in the reconnection process that is parallel to the magnetic field can accelerate charged particles to high energies (Litvinenko 1996). Mechanisms that have been proposed to be important in flare SEP acceleration, include acceleration at magnetic islands as the current sheets between the islands contract and merge (Drake et al. 2006), collapsing magnetic traps created in the newly reconnected coronal magnetic field lines (Grady & Neukirch 2009), and second–order Fermi acceleration via particle scattering on magnetic fluctuations (Desai & Giacalone 2016). Other mechanisms for SEP acceleration include stochastic acceleration in the flare–generated turbulence (Ryan & Lee 1991), and acceleration by a shock created by reconnection plasma jets (Mann 2015; Guo & Giacalone 2012; Desai & Giacalone 2016). The enhancement of ion species such as ^{3}He and Fe, a feature of impulsive events, is explained as the resonant stochastic acceleration by plasma waves that selectively resonate with and accelerate more efficiently ^{3}He than ^{4}He, and Fe than O (Fisk 1978; Miller & Vinas 1993; Mason et al. 2004).

There are many studies that provide evidence that charged particles can be accelerated at shocks near the Sun and at the interplanetary shocks (Reames 1999; Desai & Giacalone 2016). Diffusive shock acceleration (DSA) is the main mechanism thought to be responsible for acceleration of particles by shocks. The DSA mechanism can accelerate SEPs provided that they can cross the shock boundary multiple times (Jokipii 1982). At each crossing of the shock a particle gains energy and leaves the shock site to the downstream. In the downstream region, it is scattered towards the shock by the increased turbulence, and is returned to the shock site to be re–accelerated. The process is repeated multiple times until the particle gains sufficient energy to leave the shock site and propagate into the interplanetary medium. Shocks can also accelerate particles via shock drift acceleration (SDA). The angle between the shock normal and the magnetic field, which can vary depending on the shock geometry, is an important factor in consideration of the acceleration efficiency. Quasi–parallel shocks are often found at the nose of a shock, while quasi–

perpendicular shocks can often be found at its flanks. DSA can efficiently accelerate particles under any shock geometry. SDA is most efficient in perpendicular shocks. Particles can be accelerated in shocks continuously during its propagation through the IPM, but the efficiency of particle acceleration decreases with the distance travelled from the Sun. When a shock passes at the observer's location, an increase of particle flux can occasionally be observed, peaking at the time of the shock passage (see ESP increase in Figure 1.1), but such increases are less pronounced at high SEP energies (Desai & Giacalone 2016). Therefore, it has been suggested that shocks in the interplanetary medium can continuously accelerate SEPs only to several tens of MeV energies, and SEPs at highest kinetic energies are most efficiently accelerated while the shock is near the Sun.

1.3.2 SEP transport

In the heliosphere, the trajectories of charged particles are mainly influenced by the interplanetary magnetic field. The average magnetic field can be modelled as the Parker spiral (Parker 1958). At the Earth, the magnetic field is inclined, on average, 45–60 ° with respect to the Sun–Earth line, and the angle depends on the solar wind speed. As a result, the magnetic field line connecting the Earth has its footpoint on the solar surface in the region in the western hemisphere, $\approx 45 - 60\,^{\circ}$ west of the central meridian. Observations of SEP events show that onset times and times to maximum intensity are reached earlier in those SEP events that originate near the region with the best magnetic connection to the Earth (Klecker et al. 2006a).

The equation that has often been used to describe the transport of SEPs in the IPM is the focussed transport equation, which models SEP propagation in cases where the particle distributions are anisotropic (Roelof 1969; Ruffolo 1995; Kóta 2000; Dröge et al. 2010). The focussed transport equation describes convection, adiabatic deceleration, magnetic focussing and pitch–angle scattering, but in its applications it often neglects the particle drift, which is generally thought to be negligible for SEPs (Mikić & Lee 2006). The equation is used to describe particle propagation

in cases where the pitch–angle scattering is weak, and where the magnetic field diverges strongly near the Sun, such as for the interplanetary magnetic field in the expanding solar wind (Desai & Giacalone 2016). The focussed transport approach has often been used to model SEPs in gradual events. In this description, particles propagating away from the Sun quickly become focussed, anisotropic and propagate mostly along the magnetic field. The scattering of the pitch angle occurs due magnetic irregularities and leads to spatial diffusion. In parallel propagation, SEPs are scattered off fluctuations in the magnetic field and this process is characterised by means of a scale length called the *mean free path*. Theoretical estimates of the mean free path value from quasilinear theory are usually smaller than those suggested by observations (Desai & Giacalone 2016).

The focussed transport equation was also applied to SEPs to describe the transport and acceleration of particles in shocks (Lee & Fisk 1982; Lee & Ryan 1986) as well as the ESP enhancements (Lee 1983).

Perpendicular SEP transport

A major question in SEP studies relates to the degree by which particles are able to propagate perpendicular to the average magnetic field of interplanetary space. Possible mechanisms for perpendicular transport include perpendicular diffusion associated with scattering off magnetic turbulence, field line meandering, and particle drift.

Large SEP events detected simultaneously by multiple spacecraft show that SEPs can be observed over a wide range of longitudes (Cliver et al. 1995; Gómez–Herrero et al. 2015) and latitudes (Lario et al. 2003; Tylka et al. 2013). The observations require either sources that can accelerate and inject particles onto magnetic field lines over a range of longitudes and latitudes, or an efficient perpendicular transport.

Observations from Ulysses showed indications that the role of perpendicular transport is not negligible and that particles that are injected at a small region near the Sun can propagate across the mean magnetic field efficiently (Dalla et al. 2003).

Cross–field diffusion for SEPs is poorly understood within quasilinear theory, compared to the parallel diffusion (Desai & Giacalone 2016). Quasilinear theory assumes that the magnetic field fluctuations occur on scales larger than the gyroradius of SEPs. Because the mean free path for scattering is much larger than a single gyroradius and scattering events are infrequent, SEP transport occurs primarily in the direction that follows the magnetic field lines, leading to inefficient cross–field diffusion that is often neglected. One mechanism that can contribute to the overall perpendicular transport of SEPs is a field line random walk (Jokipii & Parker 1968; Giacalone & Jokipii 2012; Kelly et al. 2012; Laitinen et al. 2013). On average, the magnetic field lines form the Parker spiral, but individual field lines can meander from the trajectories prescribed by the Parker spiral, e.g. as a result of solar supergranulation (Jokipii & Parker 1968) together with the solar wind advection (Desai & Giacalone 2016). Particles that are injected and propagate on these field lines will be found at a location that is different than that given by the mean magnetic field.

Recent analysis has shown that guiding centre drifts associated with the curvature and gradient of the interplanetary magnetic field also produce transport across the field and this will be discussed further in Section 2.3.2.

1.4 Heavy ion SEP events

Elemental abundances in the heliosphere were measured on many occasions during SEP events and in quiet times (Anders & Grevesse 1989; Reames 1995, 1998, 2014), and reflect those found in the Sun. The most abundant elements in SEP events, except for H, include He, C, N, O, Ne, Mg, Si, and Fe. The elements heavier than H are often called heavy ions.

While solar abundances in the photosphere and solar corona can be measured by remote sensing, elemental abundances in the solar wind and SEP events are measured in situ using particle instruments.

The differences in SEP abundances measured during gradual and impulsive

events are the basis of the two–class paradigm (Reames 1999). Mean abundances in gradual events are similar to those found in the solar wind, but vary more significantly event to event. Abundances in impulsive events often show enhancements in the electron–to–proton ratio, ^{3}He/^{4}He, Fe/O, and ultra–heavy elements (Mason et al. 2004). The ^{3}He/^{4}He abundance in impulsive events can be enhanced by as much as 1000 times and the Fe/O ratio by a factor 10 over the average values in gradual events (Reames et al. 1994; Reames 2013), therefore these events are often called ^{3}He–rich or Fe–rich events. Heavy ion elemental abundances are often normalised to oxygen (Reames 1998). For example, the average Fe/O abundance, the ratio of Fe and O abundances integrated over many gradual events, was calculated to be 0.134 (Reames 1998).

The source of the ^{3}He and Fe enrichment in impulsive events is still a matter for scientific debate. The overabundance of ^{3}He and Fe in impulsive events is understood to be a result of a wave–particle interaction and stochastic acceleration that preferentially accelerate ^{3}He over ^{4}He, and Fe over O in solar flares (Reames 1995, 1999).

However, Fe–rich SEP events could be related to the source plasma accelerated by interplanetary shocks. For example, Mewaldt et al. (2006) studied abundances in the suprathermal tail of the solar wind, which are thought to be the seed particles for SEP events, and found that the suprathermals were Fe–rich, particularly during periods with high solar activity. It has not yet been established to what extent the Fe content in SEP abundances is modulated by the source or the selective acceleration.

In the past, SEP events have often been analysed using abundances averaged over the entire SEP event, probably due to low relative abundances of heavy ions or limited sensitivity of particle instruments. Using particle instruments with improved collecting power, we can use time–resolved heavy ion data to study temporal evolution of heavy ion abundances. Heavy ion SEP ratios, such as Fe/O, often display a decrease over the duration of an SEP event. Time dependence of heavy ion ratios has

been interpreted as a signature of SEP propagation (Scholer et al. 1978; Mason et al. 2006, 2012; Tylka et al. 2013; Dalla et al. 2017b) or acceleration (Tylka et al. 1999). The temporal dependence of heavy ions will be further discussed in Section 2.2.2.

1.5 Objectives of the thesis

SEP observations reflect the particles' history in the heliosphere and carry information about the acceleration and transport processes acting on the SEPs. Many authors, e.g. Reames (1999), Kallenrode (2004), Lario et al. (2013), agree that simultaneous observations of SEPs by multiple spacecraft are needed in order to disentangle the contributions of acceleration and propagation to the measured particle data at 1 AU.

It is evident that a growing number of SEP events, particularly those observed simultaneously by multiple spacecraft (Dresing et al. 2014; Gómez–Herrero et al. 2015; Zelina et al. 2015), and SEP events with signatures of both impulsive and gradual type (Wiedenbeck et al. 2013; Cohen et al. 2014), cannot be fully understood under the two–class paradigm. The mechanism that can distribute SEPs efficiently in longitude and latitude remains unknown.

The m/q value of a charged particle is known to be an important parameter in many acceleration and propagation processes. Heavy ion SEPs, which are not fully ionised in interplanetary space, can take a range of m/q values and be useful probes of m/q–dependent processes. The observed temporal variation of SEP ratios (e.g. Tylka et al. 1999; Mason et al. 2012; Zelina et al. 2015) may be related to an m/q–dependent mechanism that is acting on SEPs. Whether the same mechanism, which causes temporal evolution of heavy ion abundances, can also distribute SEPs in longitude and latitude, is not presently known. However, heavy ions may be the key to understanding the SEP observations at regions with poor magnetic connection as well as the temporal evolution of SEP ratios.

The study summarised in this thesis aims to analyse SEP data obtained by state–of–the–art particle instruments onboard multiple spacecraft. The main goals of the analysis are:

a) To write computer code to process, analyse and plot SEP data from multiple spaceborne particle instruments.

b) To study the properties of heavy ions for a large number of SEP events, including the information on the associated solar eruptive events.

c) To analyse the longitudinal dependence of Fe/O using simultaneous observations from multiple instruments.

d) To carry out quantitative analysis of time profiles of elemental ratios and study the dependence of temporal evolution on m/q.

e) To discuss the findings in the context of SEP acceleration and propagation mechanisms, including the drift motion of energetic particles.

The analysis will use heavy ion SEP data from particle instruments onboard the ACE, SOHO and two STEREO spacecraft.

Chapter 2

SEP observations and modelling

As discussed in Chapter 1, SEPs are associated with solar flares and CMEs. They carry information about their acceleration and the conditions of the interplanetary medium, through which they propagate. At the same time, SEPs affect human activities and are an important component of the space weather. SEPs can be observed at locations widely separated in longitude and at high heliographic latitudes. The fastest SEPs can travel to 1 AU in about ten minutes.

However, the mechanism or mechanisms that allow them to reach regions of poor magnetic connection are not well understood. Observations and modelling can be used to further our understanding of SEP transport in the heliosphere. The modelling efforts have mostly been focussed on simulations within the framework of focussed transport theory, however, this cannot satisfactorily explain all the observations. In addition, both acceleration and transport mechanisms acting on SEPs can play a role in the observed particle fluxes, and their relative contributions can vary significantly event to event.

In this chapter, SEP instrumentation and observational techniques are presented in Section 2.1, SEP observations in Section 2.2, and SEP simulations and modelling in Section 2.3.

2.1 Instrumentation

Only the SEPs at the highest kinetic energies can be detected at ground level. There, it is mostly the secondary particles, which are produced by collisions with the particles in the atmosphere, that can be observed by neutron monitors during GLEs.

SEPs are commonly observed in situ by particle instruments onboard spacecraft. Particle instruments have been placed on high–altitude balloon and rocket flights, in lower Earth orbit, in geostationary orbit, at the L1 Sun–Earth Lagrangian point, or they may be travelling through space in specific orbits. Such instruments may be designed to measure the particle counts, particle energy, nuclear and ionic charge or mass.

2.1.1 Particle energy measurement

Energy loss versus total energy method

A solid state detector is a device that can measure energy of a particle deposited into a material (Ilgner 2012, p. 523). The incoming energetic particle interacts with electrons in the material as it penetrates through the material creating electron–hole pairs. If the there is an electric field applied to the material made of a semiconductor, the setup acts as a reverse biased diode. The energy deposited into the detector is proportional to the collected charge between the electrodes. If the thickness of the semiconductor layer and the incident angle of the particle are known, energy loss per unit length, $\mathrm{d}E/\mathrm{d}x$, can be expressed using the Bethe–Bloch theorem.

Solid state detectors arranged into a series form a particle instrument so–called $E \cdot \mathrm{d}E/\mathrm{d}x$ telescope. Total kinetic energy of the energetic particle, E, measured by the particle instrument can be estimated as the sum of energies lost in each layer. When the two quantities, energy loss per unit path $\mathrm{d}E/\mathrm{d}x$ and total kinetic energy of a particle E, are multiplied together, their product $E \cdot \mathrm{d}E/\mathrm{d}x \propto Z^2 M$, where Z is atomic number of the incident particle and M its atomic mass, uniquely identifies

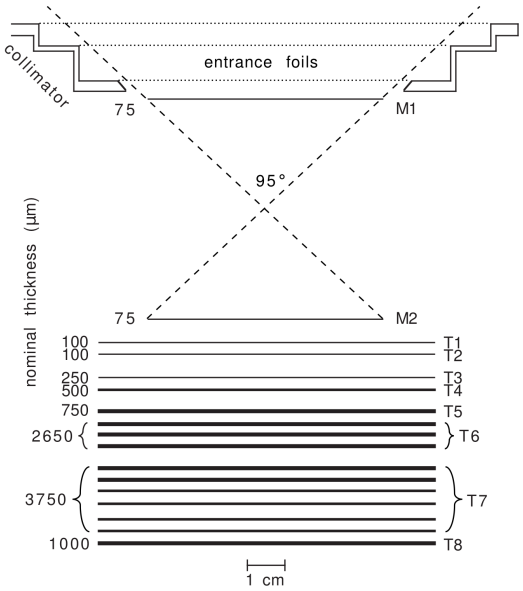

Figure 2.1: Schematic drawing of the ACE/SIS instrument, to scale. Taken from Stone et al. (1998).

elements, or even isotopes, provided that the resolution of the particle instrument is good (Mitchell & Hams 2012, p. 575).

The $E \cdot \mathrm{d}E/\mathrm{d}x$ telescope setup can be found in particle instruments such as Solar Isotope Spectrometer (SIS) onboard ACE, Energetic and Relativistic Nuclei and Electron (ERNE) onboard SOHO, Low Energy Telescopes (LET) and High Energy Telescopes (HET) onboard STEREO. A schematic drawing of the SIS instrument is shown in Figure 2.1. On the top of the instrument there are a collimator, which constrains acceptance angle of the telescope, and a hodoscope, a kind of position–sensitive detector that measures the incident trajectory of a particle. Below is the solid state telescope, a stack of silicon wafers of known thickness. The acceptance angle set by the collimator for this particle instrument is 95 °. The geometric factor of a particle instrument is the area of the detector multiplied by the solid angle. The geometric factor value of the SIS instrument is $\sim 40\,\mathrm{cm}^2\,\mathrm{sr}$.

The efficiency of depositing energy into a material is higher at lower kinetic energies. The method described above involves some approximations and does not account for imperfections in the silicon layers, dead layers, the spaces between the layers, and energy dependence across the energy spectrum of incident particles.

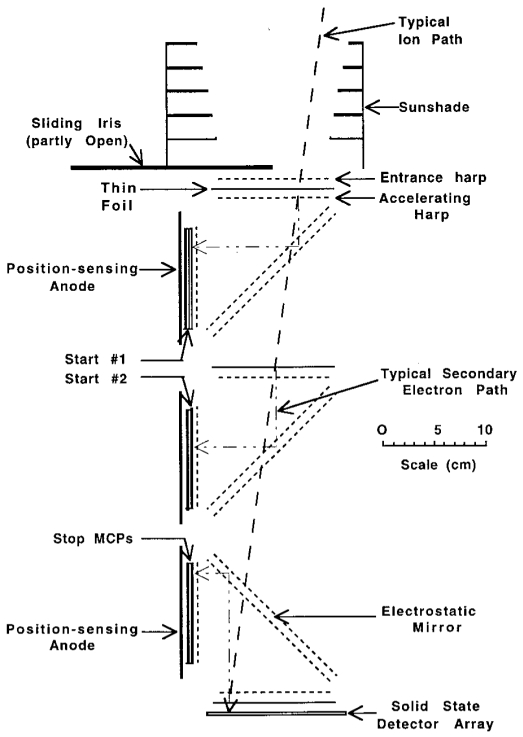

Figure 2.2: Schematic drawing of the ACE/ULEIS telescope. Taken from Mason et al. (1998).

Before their deployment, particle detectors undergo calibration using a spectrum of elements over a range of kinetic energies. The data are output as elements organised into differential energy bins by their E/m.

Time–of–flight method

Kinetic energy up to a few MeV/nucleon can be measured by the time–of–flight technique. A representative instrument is the Ultralow–Energy Isotope Spectrometer (ULEIS) instrument (Mason et al. 1998) onboard ACE. A schematic drawing of ULEIS is shown in Figure 2.2. The main parts of the telescope include a collimator, which also works as a sunshade, a time–of–flight spectrometer, and an $E \cdot \mathrm{d}E/\mathrm{d}x$ particle detector.

The kinetic energy of particles E, measured by a solid state detector placed at the bottom of the telescope, and the time of flight t are measured simultaneously for all particles that enter the telescope. The mass of an ion m can be calculated as $m = 2E(t/L)^2$, where L is the path length in the telescope. ULEIS cannot distinguish

between isomers, different elements with equal mass, e.g. ^{14}O and ^{14}N, but there are only a few isomers lighter than nickel, so that they are not an important source of ambiguity (Mason et al. 1998).

Particle mass, energy and element are provided in the final data product. The ULEIS telescope can measure isotopic composition of SEPs over a broad range of energies, but ionic charge measurement is not possible using the time–of–flight technique.

Deflection methods

The electrostatic deflection method is not used directly to measure particle kinetic energy but it is used to separate ions in defined ranges of energy per charge, E/q, at energies between those typical of the suprathermal solar wind particles and the lower end of the SEP energy range. Such a setup was previously used in the UltraLow Energy Z-E-Q Analyzer (ULEZEQ) instrument onboard the International Sun/Earth Explorer 3 (ISEE–3) spacecraft (Hovestadt et al. 1978), and more recently in the Solar Energetic Particle Ionic Charge Analyzer (SEPICA) instrument (Möbius et al. 1998) onboard ACE. The SEPICA instrument ceased to work due to a failure of control valves in 2005.

A schematic drawing of SEPICA is shown in Figure 2.3. The main parts of the telescope include a multi–slit collimator, an electrostatic analyser with deflection plates, a proportional counter, a solid state detector and an anti–coincidence scintillator covering the rear side of the detector. Particles that enter SEPICA through the collimator are deflected by the electric field applied to the deflection plates and detected in a series of detectors located on the far side from the collimator.

The collimator passively selects particles with pre–defined trajectories and creates a well–defined focal plane in the detector plane, where the particles with equal velocity component perpendicular to the detector are deflected by the same amount. Figure 2.3 shows a pair of undeflected and a pair of deflected ion trajectories. The lateral deflection, which is inversely proportional to E/q, is measured by the pro-

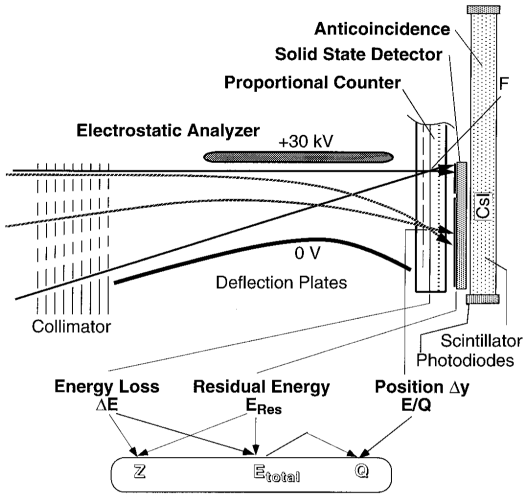

Figure 2.3: Schematic drawing of the ACE/SEPICA instrument. Taken from Möbius et al. (1998).

portional counter together with the specific energy loss $\mathrm{d}E/\mathrm{d}x$ and the particle's incident angle onto the detector. The total kinetic energy E is approximated by the residual energy E_{res} measured by the silicon solid state detector.

In this setup, $\mathrm{d}E/\mathrm{d}x$, E_{res} and E/q are measured independently, which allows for the calculation of particle's charge q. The setup with multiple slits in the collimator effectively expands the dynamic energy range of the detector.

2.1.2 SEP charge measurement

Measurement of the charge state of SEPs is not routinely carried out for all SEP events. The two main techniques for ion charge state measurement include the electrostatic deflection and the geomagnetic cutoff rigidity method (Klecker et al. 2006b).

Electrostatic deflection method

The direct method to measure ionic charge using the electrostatic deflection technique was deployed in the ULEZEQ instrument onboard ISEE–3 (Hovestadt et al. 1978) and more recently in the SEPICA instrument onboard ACE (Möbius et al. 1998). The lateral deflection by an electrostatic field of a particle with the charge

q and kinetic energy E is inversely proportional to E/q. The kinetic energy of a particle needs to be measured independently of the deflection, e.g. by a solid state detector or an $E \cdot \mathrm{d}E/\mathrm{d}x$ telescope, to allow for calculation of q.

The telescopes using electrostatic deflection can scan over a range of voltages between the deflecting plates in order to provide measurements over a wider range of values.

Cutoff rigidity method

The indirect method takes advantage of the Earth's magnetic field. When a charged particle cannot access regions with stronger magnetic field it is reflected back. The reflection occurs when the particle's rigidity $R = p/q$ is equal to the cutoff rigidity R_c at that point. Therefore, charged particles with rigidity values below the cutoff rigidity are excluded from and cannot penetrate deeper into the magnetosphere.

Instruments onboard a spacecraft placed on the highly–inclined, low orbit within the Earth's magnetosphere are measuring SEPs, their kinetic energy and the local magnetic field vector. The position at which the proton count at a given energy drops significantly marks the cutoff rigidity value at that point. The cutoff rigidity for protons can be calculated at that point because that the charge state of a proton is +1. Equating the rigidity of protons and other elements when a dropout occurs in a heavy ion intensity, and determining the energy at which the cutoff occurs in each elemental species, the charge of these elements can be calculated. This method was used by the Solar, Anomalous, and Magnetospheric Particle Explorer (SAMPEX) satellite (Baker et al. 1993). Three particle instruments LICA, HILT and MAST onboard SAMPEX observed dropouts in heavy ion particle intensity over a broad range of energies $0.3 - 70$ MeV/nucleon, from which the SEP ionic charge values were inferred in several SEP events, e.g. by Oetliker et al. (1997) and Mazur et al. (1999).

2.1.3 Spacecraft missions

The ACE (launched in 1997) and SOHO (launched in 1995) spacecraft were deployed to be able to measure SEPs during solar cycle 23 and both have been operational during solar cycle 24 as well. Both spacecraft have been placed on elliptical Lissajous orbits around L1. SOHO is a three–axis stabilised spacecraft while ACE is a spinning spacecraft with a period $\sim 12\,\mathrm{s}$ and its spin axis pointed along the Sun–Earth line.

In 2006, two almost identical STEREO Ahead (STA) and STEREO Behind (STB) spacecraft were launched into their heliocentric orbits, Ahead leading and Behind trailing the Earth. The spacecraft were placed in the ecliptic plane at a radial distance ≈ 1 AU, STEREO A inside Earth's orbit and STEREO B outside. As a result, their orbital periods are slightly different and the spacecraft separate from the Earth by $\approx 22\,^{\circ}$/year. On 6 February 2011 the two spacecraft were separated by $180\,^{\circ}$, observing the entire solar surface for the first time in history. The contact with STEREO B was lost after a scheduled reboot before the passage behind the Sun in October 2014. During 2015 both STEREO spacecraft passed behind the Sun and the contact with STEREO A was re–established in July 2015. The STEREO spacecraft are, similarly to SOHO, three–axis stabilised spacecraft.

Particle instruments

In this thesis work, for the study of heavy ion particles, I used SEP data measured in situ by the following particle instruments: Solar Isotope Spectrometer (SIS; Stone et al. 1998) onboard ACE, Energetic and Relativistic Nuclei and Electron (ERNE; Torsti et al. 1995) onboard SOHO, and Low Energy Telescopes (LET; Mewaldt et al. 2008) and High Energy Telescopes (HET; von Rosenvinge et al. 2008) onboard the STEREO Ahead and Behind spacecraft. These particle instruments measure protons and heavy ions using the $E \cdot \mathrm{d}E/\mathrm{d}x$ technique over an energy range that is similar among the particle instruments. The SEP data are organised into differential energy channels and they cover the energy range $\approx 1 - 100$ MeV/nucleon. The available energy bins for each particle instrument are shown in Figure 2.4.

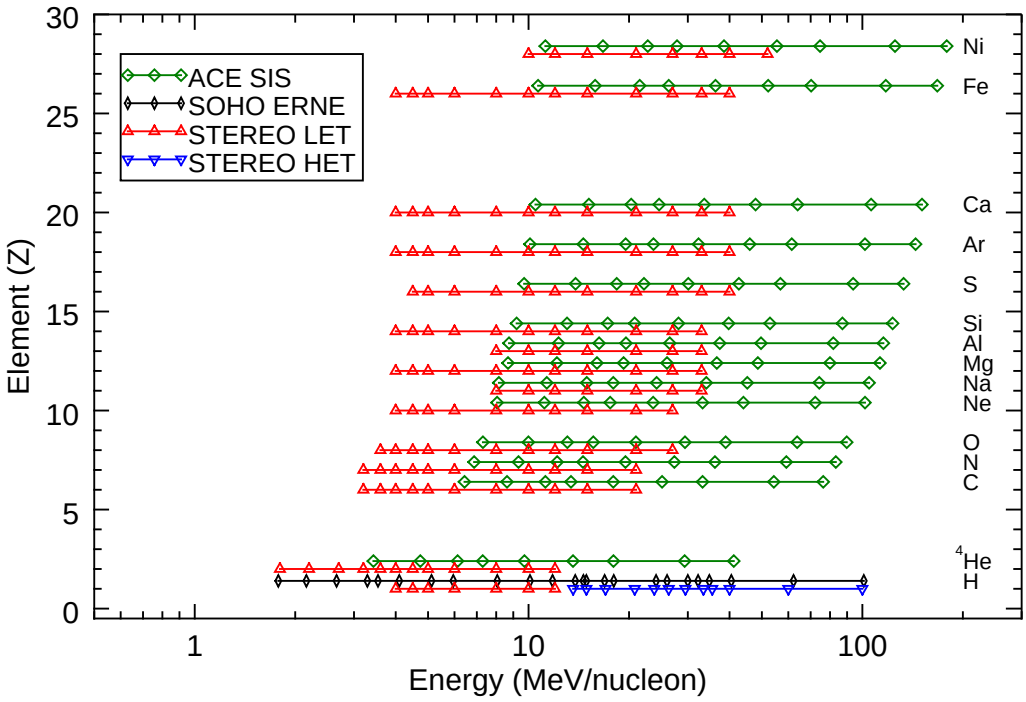

Figure 2.4: Elements and energy bins available in the SEP data from SOHO/ERNE, ACE/SIS, STEREO/LET and STEREO/HET.

ERNE can detect energetic protons and α particles. The ERNE instrument has 2 telescopes: Low Energy Detector (LED) operating in the energy range 1–13 MeV/nucleon and a geometric factor $\approx 0.2-0.8\,\mathrm{cm^2\,sr}$, depending on the energy range and species; High Energy Detector (HED) operating in the 14–131 MeV/nucleon energy range with a geometric factor $\approx 20-30\,\mathrm{cm^2\,sr}$, again depending on the energy range and species. Each ERNE telescope provides the data in 10 energy bins with 1–minute time resolution.

SIS was designed to measure 14 heavy ion elements including He at 256–second time resolution. The SIS instrument has two identical telescopes with area $\sim 65\,\mathrm{cm^2}$ each with a geometric factor $\sim 40\,\mathrm{cm^2\,sr}$. The heavy ions are measured in 8 energy bins. Due to the SIS instrument characteristics and precise calibration, the energy bin values were calculated for each element separately, and are different for each element, as seen in Figure 2.4 (see also Figure 19 in Stone et al. 1998 for reference). For example, the lowest energy bin for He is $3.4-4.7$ MeV/nucleon while the lowest

Fe energy bin is $10.7 - 15.8$ MeV/nucleon.

The LET instrument provides data for 16 elemental species, including protons, with 1–minute time resolution. The data are organised into $\sim$ 12 energy bins in the $\sim 3 - 30$ MeV/nucleon energy range as shown in Figure 2.4 (see also Figure 1 in Mewaldt et al. 2008). LET has ≈ 4 cm^2 sr geometric factor, depending on the analysed element, and it can also provide sectored data from 16 directions.The heavy ion sensitivity threshold of SIS is lower compared to LET due to about 10 times larger geometric factor.

HET, which has 0.61 cm^2 sr geometric factor, can measure proton and electron SEPs with 1–minute resolution. Electrons are measured in 3 energy channels in the $0.7-4.0$ MeV energy range and protons in 11 energy channels between $13-100$ MeV.

A particle instrument intercalibration for protons between STEREO/HET and SOHO/ERNE was done using data from December 2006 event, when the STEREO spacecraft were in the vicinity of the Earth. The measured data show overall good correlation between the particle instruments (Richardson et al. 2014).

Space–based instruments onboard the ACE, SOHO and STEREO spacecraft offer increased collecting power over previously flown instrumentation. In addition, the STEREO mission, combined with near–Earth spacecraft at the L1 point, offer a unique opportunity to study the perpendicular transport at similar radial and latitudinal locations but progressively separating in longitude.

To carry out multi–instrument analysis, in this work heavy ion data from ACE/SIS and proton data from SOHO/ERNE were matched to complement the STEREO data measured by LET and HET.

2.2 Key SEP observations

The Sun is the source of a dipole magnetic field, which is modified by a plasma outflow known as the solar wind. The solar rotation, combined with the fact that the magnetic field is frozen into the solar wind plasma, results in a heliospheric

magnetic field of spiral shape, the Parker spiral (Parker 1958).

A heliospheric current sheet separates the magnetic field of opposite polarities. In quiet times during the solar minimum the mean magnetic field is well described as a Parker spiral with flat current sheet, but during the solar maximum the heliospheric magnetic field becomes more complicated and the current sheet resembles the shape of a ballerina skirt.

At Earth, at 1 AU near the ecliptic plane, a heliospheric magnetic field line is inclined at approximately 45–60 ° from the Sun–Earth line, depending on the solar wind speed. SEP propagation is influenced by the mean magnetic field: an observer at Earth or L1 is most likely to observe an SEP event when the parent active region is near $\approx 45 - 60\,^{\circ}$ W on the solar disk, although gradual events can be observed over a much wider range of longitudes (Reames 1999).

2.2.1 SEP observations by multiple spacecraft

Studies using data from the Helios spacecraft showed that SEPs from a single parent active region can be detected simultaneously by spacecraft with significant separation in longitude (McGuire et al. 1983; Kallenrode 1993). In addition, SEPs were observed simultaneously by the Ulysses spacecraft at high heliographic latitudes and by near–Earth spacecraft (Dalla et al. 2003). Since the launch of the STEREO spacecraft, there have been many reports of proton and electron SEP events at widely separated locations. In some cases, SEPs can fill the entire heliosphere (Gómez–Herrero et al. 2015).

In one particular statistical study, Richardson et al. (2014) analysed 209 proton events at energy >25 MeV that occurred in 2006–2013 using the twin STEREO spacecraft and SOHO, a near–Earth spacecraft. They found that 34% of all events were observed by two spacecraft and 17% by all three spacecraft. About a quarter of observed events originated behind the western limb with respect to the observer, and a small fraction ($\sim$ 10%) behind the eastern limb. SEP properties are known to display large event–to–event variation. An east–west asymmetry in delays to onset

and peak times has been reported (Lario et al. 2013).

Dresing et al. (2012) studied the 17 January 2010 SEP event, where electrons were observed over a broad range of longitudes, by analysing the particle time intensity profiles and anisotropy. They interpreted the observations by means of a model with significant perpendicular diffusion. This provided a better fit to the data than a model with long–duration particle acceleration and lateral transport taking place in the corona. In a follow–up study, Dresing et al. (2014) studied particle anisotropies in 21 SEP events and found a group of SEP events consistent with a narrow acceleration region and significant perpendicular transport, another group that was consistent with spatially extended acceleration, e.g. by a CME–driven shock, and a third group with complex anisotropy features, for which a clear interpretation could not be given.

Lario et al. (2013) studied 35 STEREO events and found that a Gaussian fit to the longitudinal distribution of proton peak intensities showed a standard deviation in the range $\sigma = 15 - 38\,^{\circ}$, offset towards the central meridian as seen from the Earth. This effect was interpreted as a shift in magnetic connectivity towards the nose of a CME–driven shock. Lario et al. (2006) obtained similar results for data from the Helios and Interplanetary Monitoring Platform–8 (IMP–8) spacecraft.

Wiedenbeck et al. (2013) analysed ^{3}He rich events detected by STEREO and ACE and reported of an impulsive event that was observed by three spacecraft, two of which were separated by $136\,^{\circ}$. As part of a statistical study of 17 impulsive events they showed that simultaneous SEP detections at two spacecraft at longitudinal separation $> 60\,^{\circ}$ were not uncommon.

In separate studies, Gómez–Herrero et al. (2015) and Lario et al. (2016) used data from 3 spacecraft and found that Fe and O SEPs from a single parent active region can reach locations widely separated in longitude and be detected over almost $360\,^{\circ}$.

High values of event–averaged Fe/O are another signature of impulsive events, but Cohen et al. (2014) reported of an SEP event, where enhanced Fe/O values were observed at two spacecraft separated $135\,^{\circ}$ in longitude, none of which was well

connected to the source active region. Tylka et al. (2013) studied 2 large SEP events, in which a large enhancement in Fe was observed early in the events by Wind near the ecliptic and by Ulysses at high heliographic latitudes.

Since impulsive events are thought to originate in compact flare regions, the mechanism that would allow particles from these events to reach locations widely separated in longitude from the parent active region has not yet been identified.

It has been suggested that the arrival of SEPs in these events could be the result of contributions from multiple mechanisms (Gómez–Herrero et al. 2015).

2.2.2 Fe/O decreases and time dependence of ionic ratios

In the past, SEP abundance ratios have often been analysed after averaging over the duration of an SEP event and not much attention was given to the time dependence of heavy ion ratios. This was likely due to low fluxes of heavy ions compared to protons and limited sensitivity of previous–generation instruments. Nowadays, we have the opportunity to use particle instruments with sensitivity and temporal resolution superior to those of previous–generation instruments, and to better observe and resolve the temporal dependence of heavy ions.

SEP ratios, such as Fe/O, often display a decrease over the duration of an SEP event. Using 3–hour averaged data, Scholer et al. (1978) observed Fe/O ratios decreasing in time while the C/O ratios were time independent. Tylka et al. (1999) reported observations of the temporal evolution of several heavy ion ratios during the 1998 April 20 SEP event that were ordered by their M/Q values, where M is atomic mass number of an SEP ion and Q its charge number. Mason et al. (2012) studied the temporal evolution of Fe/O, O/He, and He/H ratios in 17 SEP events, where in the majority of events the ratios exhibited temporal variation. Tylka et al. (2013) used Ulysses and near–Earth spacecraft data to show that the characteristic Fe/O decrease over time was present at both spacecraft, both of which had poor magnetic connection to the parent flare.

Several researchers have proposed interpretations of the observed time depen-

dence of elemental ratios, either as an effect of acceleration or of transport. It was suggested that the high Fe/O ratio early in the SEP event is a result of an initial flare component (rich in Fe) while the decrease that follows is associated with a shock–accelerated component (with lower Fe/O) later in the event (Cane et al. 2003). Tylka et al. (1999) explained it as due to the ions with high m/q (i.e. Fe) escaping the accelerating shock region more easily. Others proposed that the observed time dependence is a propagation effect due to the rigidity dependence of the mean free path (Scholer et al. 1978; Mason et al. 2012), or more generally transport effects (Tylka et al. 2013).

2.3 Modelling of SEP propagation

Using particle propagation models and testing the simulation results against the observations is an important part of SEP science. This way many important parameters, e.g. the injection profiles, the mean free path and the diffusion coefficient of the SEP propagation, can be determined that cannot be measured directly. Many data–driven studies, e.g. Tylka et al. (1999); Dresing et al. (2012); Mason et al. (2012); Tylka et al. (2013), include a modelling part to support the observations. Most current SEP models are not self–consistent, i.e. cannot solve for all acceleration and transport phenomena within a single model. Progress in this area can be achieved by coupling of models: for example, the MHD modelling approach can be used for simulations of the solar wind particles and CMEs, and its output in the form of magnetic fields can be used as an input for focussed transport particle simulations (Manchester et al. 2005; Kóta et al. 2005).

2.3.1 Focussed transport

In propagation models based on kinetic theory, the distribution function of anisotropic population of energetic particles f propagating away from the Sun in the inner heliosphere is often modelled using the focussed transport equation (Roelof 1969):

$$\frac{\partial f}{\partial t} + \mu v \frac{\partial f}{\partial s} + \frac{1-\mu^2}{2\zeta} v \frac{\partial f}{\partial \mu} - \frac{\partial}{\partial \mu}\left(\kappa(\mu)\frac{\partial f}{\partial \mu}\right) = Q(r, v, t) \tag{2.1}$$

where r, v, and t are position, speed and time, the coordinates of the phase space, s is the length along the magnetic field line, $\mu = \cos(\alpha)$ the pitch angle cosine, κ the diffusion coefficient, $\zeta = -B(s)/(\partial B/\partial s)$, and Q is the source term. This equation typically has to be solved numerically, usually via finite–difference method or Monte Carlo simulations.

The pitch angle of a particle α, the angle between the particle velocity and the magnetic field vector, decreases with increasing distance travelled from the Sun as a result of the diverging magnetic field. Particles become focussed quickly after they are released into the IPM, especially near the Sun where the gradient of magnetic field is high. Pitch angle scattering occurs due to small–scale turbulence in the magnetic field (Ruffolo 1995). In kinetic theory the mean free path λ represents a travelled distance, during which the cumulative effect of small–angle scattering events changes the pitch angle by 90 °. The mean free path value in the heliosphere is not easily determined and depends on the conditions of the IPM. A typical range of values λ used in simulations for protons lies between $\lambda = 0.1 - \sim 2\,\mathrm{AU}$ depending on the model used (Dröge et al. 2014; Kelly et al. 2012).

Generally, the parameters that control the final time profiles include the mean free path, and the source spectral index γ (the injected spectrum $\propto E^{-\gamma}$). In many cases, the particle injection is assumed to be shorter than the propagation time scales and is modelled as a δ–function, an instantaneous injection in time. A continuous injection can be represented as a sum of δ–injections. In propagation models the distribution function of particles are followed after their acceleration.

Agueda et al. (2008) used a Monte Carlo method to model the time profiles of near–relativistic electrons in the Parker spiral. They used the Green's function of particle propagation to model the contributions of particle acceleration and transport, and to determine the particle injection profile. Using their model they found that the injection profile had 2 distinct components, a prompt component associ-

ated with type III radio burst, and a delayed component that could be associated with a CME–driven shock, and that the mean free path for electrons in the event considered was $\lambda = 0.9$ AU. Additionally, they found that no single scenario, but a range of injection phases in cases with strong scattering and scatter–free cases, can explain different events.

Ng et al. (1999) used a rigidity–dependent mean free path $\lambda \propto (m/q)^n$, where $n = 1/3$, to account for the early arrival of ions with larger rigidity, i.e. larger m/q value. Similarly, Mason et al. (2012) used a rigidity–dependent mean free path $\lambda \propto (m/q)^n$, where the fitting parameter n was related to the turbulence spectrum of the IPM. Within this type of SEP transport model, the ion with larger rigidity has larger gyromagnetic radius and it is less sensitive to the magnetic field fluctuations, therefore it is scattered less frequently.

The perpendicular diffusion coefficient $\kappa_\perp$ was assumed to be negligible in early focussed transport models (Ruffolo 1995), and the transport equation was solved in 1D. However, multipoint observations of SEP events showed that SEP propagation must occur in 3D (see Section 2.2.1). The importance of perpendicular transport has been discussed by a number of authors (e.g. Dröge et al. 2010). Mechanisms that contribute to propagation across the mean magnetic field include large scale field line meandering (Giacalone & Jokipii 2012; Kelly et al. 2012; Laitinen et al. 2013), as well as magnetic fluctuations that scatter particle's guiding centre to another field line, and drifts.

The value of the ratio of perpendicular versus parallel diffusion coefficients, $\kappa_\perp/\kappa_\parallel$, is still a subject of scientific debate. On the one hand, some studies derived very small values $\sim 10^{-4}$ (Roelof et al. 1983) or $\sim 10^{-5}$ (Dröge et al. 2010) to explain dropouts, step–like decreases in particle intensity. On the other hand, some multispacecraft studies, e.g. Dresing et al. (2012), require large values, e.g. $\kappa_\perp/\kappa_\parallel \sim 0.3$, to explain the observations. Simulations by Kelly et al. (2012) using a model that includes meandering magnetic field lines yield an intermediate value $\kappa_\perp/\kappa_\parallel = 0.04 - 0.08$.

Mason et al. (1991) showed that 1 AU time profiles of SEP events can be well fitted by a model including scattering as well as by a model with prolonged particle injection and scatter–free propagation. Therefore, the relative contribution of acceleration and transport in determining intensity time profiles remains uncertain.

2.3.2 Test particle approach

The full–orbit test particle approach is a method where the equations of motion are solved for individual particles propagating through prescribed electromagnetic fields. Trajectories of the particles are tracked during the full gyration orbit and integrated to obtain the final positions. In this approach energetic particles do not interact with each other or with the electromagnetic fields.

In one particular study, Marsh et al. (2013) simulated the SEP propagation in the Parker spiral magnetic field solving the Lorentz force equation:

$$\frac{\mathrm{d}\mathbf{p}}{\mathrm{d}t} = q\left(\mathbf{E} + \frac{1}{c}\frac{\mathbf{p}}{m_0\gamma} \times \mathbf{B}\right) \tag{2.2}$$

where $\mathbf{p}$ is particle's momentum, q its charge, m_0 rest mass, $\mathbf{E}$ and $\mathbf{B}$ are electric and magnetic fields, c is the speed of light, and γ the Lorentz factor. SEPs were treated as test particles able to propagate in 3D. The simulation results showed that the positions of 100 MeV protons after 4 days exhibited significant longitudinal and latitudinal displacement from the magnetic field lines onto which they were initially injected and that the displacement was more significant than for 10 MeV and 1 MeV protons, respectively. When protons were substituted with Fe^{15+} and Fe^{20+} ions as the injected particles, the overall observed displacement was greater for Fe^{15+} than for Fe^{20+} due to a larger m/q value, and in turn larger for Fe that for the protons. Significant latitudinal displacement was also observed, particularly at high heliographic latitudes.

The results of the test particle simulations are in agreement with the analytical formulae for drifts in the Parker spiral studied by Dalla et al. (2013). The formulae

for drift velocities show a dependence on m/q and kinetic energy. The findings of Dalla et al. (2013) and Marsh et al. (2013) suggest that drifts may be an important component in SEP propagation. Dalla et al. (2015) further showed that the drifts contribute to the overall particle deceleration. In recent studies, Dalla et al. (2017a) and Dalla et al. (2017b) presented the results showing that several characteristics of SEPs, such as the Fe/O decreases and the energy dependence of ionic charge states, can be qualitatively reproduced by a transport model that includes drift. Observations of the time dependence of ionic ratios related to the simulation results by Dalla et al. (2017b) for Fe/O, will be presented in Chapter 5.

Energetic particles, which are partially ionised in the IPM (Luhn et al. 1985), experience a drift when they propagate in electromagnetic fields. The drift occurs when the guiding centre of the particle, the position averaged over a single gyration, is displaced in the direction perpendicular to the magnetic field. Given the dependence of drift velocities on the m/q value, drifts are more significant for heavy ion SEPs due to their low charge state, and increase with increasing particle kinetic energy. Analytical expressions for various types of drifts calculated by means of single–particle motion theory can be found in many standard plasma physics textbooks (e.g. Goldston & Rutherford 1995). Drifts include electric field, gradient and curvature drifts. The main contributors to the drifts in the Parker spiral interplanetary magnetic field (Parker 1958) are the *grad B* drift and the curvature drift due to the spiral shape of the field.

In the context of SEP propagation, drifts are a type of perpendicular transport. Drifts are commonly included in transport models of galactic cosmic rays, which have similar properties to SEPs and higher energies, but they have been neglected for SEPs so far. The current consensus on propagation of SEPs in focussed transport models is that the contributions from meandering field lines, magnetic turbulence, and drifts, if included in the model, are collectively treated within the perpendicular diffusion coefficient $\kappa_\perp$.

Chapter 3

Observations of SEP events

Studies of SEP events have mostly analysed proton and electron data, including simultaneous observations of the same event by multiple spacecraft. The proton and electron studies have been largely preferred probably due to high abundance of these particles. Studies that analysed heavy ions using observations by the STEREO spacecraft were only published recently, e.g. studies by Cohen et al. (2014); Lario et al. (2014); Gómez–Herrero et al. (2015), all of which only analysed a single SEP event.

In this chapter, I analyse heavy ion SEP data from multiple spacecraft (Section 3.1) and compile an SEP event list (Section 3.2). Events observed simultaneously at two or three spacecraft are further analysed and discussed in Chapter 4.

3.1 Observations and SEP event list

The Fe/O ratio is historically the most studied heavy ion ratio. The Fe/O abundance is commonly used to obtain information about the acceleration and transport mechanisms in SEP events. The ratio also shows a significant event–to–event variation that serves as a basis for the SEP classification. Measurements of SEP abundances averaged over a large number of gradual SEP events, e.g. by Reames (1995), show that, on average, the O abundance is larger than the Fe abundance, and that the

Fe/O ratio is 0.134 at 5–12 MeV/nucleon. Often this value is used to define whether an SEP event is "Fe–rich" or "Fe–poor". The Fe/O abundance ratio can be enhanced over 10 times above 0.134 during impulsive events (Reames 1999). Therefore, good count statistics for Fe and O in an SEP event are a necessary condition for studying the Fe/O ratio.

In this thesis work I used SEP data measured in situ by the following particle instruments: ACE/SIS[1], SOHO/ERNE[2], and the LET and HET instruments onboard the STEREO[3] spacecraft. The particle data used are level 2 data, maintained and released by the instrument teams, and publicly available from the spacecraft science center websites. I used hourly–averaged data, which provide a good compromise between the temporal resolution and the count statistics. In addition, the hourly–averaged data provide the lowest common temporal resolution for all the particle instruments used.

The Fe/O ratio value $A_{\mathrm{Fe/O}}$ was calculated as a ratio of intensities of iron I_{Fe} and oxygen I_{O}

$$A_{\mathrm{Fe/O}} = \frac{I_{\mathrm{Fe}}}{I_{\mathrm{O}}} \tag{3.1}$$

at each point in time. Ratio data points are those that have more than 2 particle counts in a 1–hour time bin for both ion species. The event–averaged Fe/O ratio of an SEP event was calculated as arithmetic mean of the Fe/O values. The uncertainty on the ratio $\sigma_{\mathrm{Fe/O}}$ was calculated using the error propagation formula

$$\left(\frac{\sigma_{\mathrm{Fe/O}}}{A_{\mathrm{Fe/O}}}\right)^2 = \left(\frac{\sigma_{\mathrm{Fe}}}{I_{\mathrm{Fe}}}\right)^2 + \left(\frac{\sigma_{\mathrm{O}}}{I_{\mathrm{O}}}\right)^2 \tag{3.2}$$

where σ_{O} is the oxygen uncertainty and σ_{Fe} is the iron uncertainty. For all the count rates, the uncertainties were calculated as $\sigma = \sqrt{N}$, where N is the particle count within the accumulation time. The intensity uncertainties are provided in the data

[1] http://www.srl.caltech.edu/ACE/ASC/level2/lvl2DATA_SIS.html
[2] https://srl.utu.fi/erne_data/
[3] http://www.srl.caltech.edu/STEREO/DATA/

files for STEREO/LET and HET.

I used the `SolarMonitor.org` database[4] (Gallagher et al. 2002) and the Lockheed Martin Solar and Astrophysics Laboratory (LMSAL) database[5] to obtain details and parameters of solar flares. Information about active regions (ARs) is maintained by the National Oceanic and Atmospheric Administration (NOAA). Spatially–resolved soft X–ray flux is continually measured by the series of GOES spacecraft in order to determine parameters of solar flares. The peak SXR flux measured in $1 - 8$ Å wavelength band is used to establish the flare class. Information about CMEs was obtained from the CDAW CME catalogue (Gopalswamy et al. 2009) maintained by The Catholic University of America in cooperation with the Naval Research Laboratory of the USA. The data used in the CDAW catalogue are measured by C2 and C3 coronagraphs[6] that are part of the Large Angle and Spectrometric Coronagraph Experiment (LASCO) instrument (Brueckner et al. 1995) onboard the SOHO spacecraft.

In order to express the longitudinal separation between a spacecraft and an active region, where the eruption occurred, I used the Parker spiral model (Parker 1958) of the interplanetary magnetic field. I recorded the local solar wind speed value at the beginning of an SEP event at each spacecraft and calculated the nominal Parker spiral footpoint on the solar surface ϕ_{ft} relative to the spacecraft using the formula

$$\phi_{ft} = \phi_{sc} + \frac{\Omega}{v_{\mathrm{sw}}}(1\ \mathrm{AU} - 1\ R_{\mathrm{S}}) \tag{3.3}$$

where ϕ_{sc} is the spacecraft longitude, v_{sw} is the solar wind speed, $\Omega = 14.7\,^{\circ}$/day is the average angular rotation at the solar equator, AU is the astronomical unit and R_{S} is the solar radius. The angular separation in longitude between the flare and the spacecraft was calculated as

[4] https://www.solarmonitor.org/

[5] http://www.lmsal.com/solarsoft/latest_events/

[6] Coronagraph C1 did not recover from a mission interruption in 1998. https://umbra.nascom.nasa.gov/soho/SOHO_final_report.html

$$\Delta\phi = \phi_{flare} - \phi_{ft} \tag{3.4}$$

where ϕ_{flare} is the flare longitude. A positive $\Delta\phi$ means that the flare is western with respect to the observer's footpoint. In a similar manner, the latitudinal separation between the flare and the observer was calculated as

$$\Delta\theta = \theta_{flare} - \theta_{ft} \tag{3.5}$$

A positive $\Delta\theta$ means the flare is north of the observer. The position of the STEREO spacecraft in the solar system was determined using the "Where is STEREO?" application provided by the STEREO Science Center[7].

The solar wind speed measurements by the Plasma and Suprathermal Ion Composition (PLASTIC)[8] instrument (Galvin et al. 2008) onboard the STEREO spacecraft and the Solar Wind Electron, Proton, and Alpha Monitor (SWEPAM)[9] instrument (McComas et al. 1998) onboard ACE were used to determine the in situ solar wind speed at the spacecraft.

The Harvard–Smithsonian Center for Astrophysics database of shocks observed at ACE[10] and as well as the Level 3 data from the STEREO spacecraft[11] were checked for the presence of any shocks that might reach the spacecraft.

I used the CDAW database[12] and the Goddard Space Flight Center database hosting STEREO/Waves data[13] that contain the radiowave data from the WAVES instrument (Bougeret et al. 1995) onboard the Wind spacecraft, and the Waves instrument (Cecconi et al. 2008) instrument onboard the STEREO spacecraft for presence of type II or III radio bursts.

[7] https://stereo-ssc.nascom.nasa.gov/cgi-bin/make_where_gif

[8] http://www-ssc.igpp.ucla.edu/forms/stereo/level2_plasma_and_magnetic_field.html

[9] http://www.srl.caltech.edu/ACE/ASC/level2/lvl2DATA_SWEPAM.html

[10] https://www.cfa.harvard.edu/shocks/ac_master_data/ac_master_2012.html

[11] ftp://stereodata.nascom.nasa.gov/pub/ins_data/impact/level3/STEREO_Level3_Shock.pdf

[12] https://cdaw.gsfc.nasa.gov/CME_list/radio/waves_type2.html

[13] https://swaves.gsfc.nasa.gov

I examined the SEP data between December 2006 and December 2016[14] and identified SEP events as times when Fe intensity was above 10^{-4}(cm^2 s sr MeV/nucleon)$^{-1}$ at 10–12 MeV/nucleon for STEREO and above 10^{-5} (cm^2 s sr MeV/nucleon)$^{-1}$ in the 10.7–15.8 MeV/nucleon channel for ACE. The lower threshold in the ACE data is due to a wider energy bin and approximately ten times larger geometric factor of the ACE/SIS instrument compared to the STEREO/LET instruments. The selected intensity thresholds correspond to a particle count of $\sim$5 particles per 1–hour accumulation time for ACE/SIS and $\sim$3 for the STEREO/LET instruments.

In addition, the criterion that the particle intensity increase was observed for $\geq$12 1–hour time intervals was introduced. I identified 50 SEP events, which are listed in Table 3.1 with their key parameters. In the table, the year, the start and end day of year (DOY) define the interval, which identifies the event. Δt as the number of 1–hour intervals, during which Fe SEPs were measured above the threshold values. Also recorded are $I_{\mathrm{Fe},max}$, the maximum Fe particle intensity in (cm^2 s sr MeV/nucleon)$^{-1}$ units during an SEP event, and event–averaged Fe/O ratio. The ratio was calculated in the 10–12 MeV/nucleon channel for STEREO and at ACE it was obtained as the ratio of Fe intensity at 10.7–15.8 MeV/nucleon and O intensity measured at 10.0–13.1 MeV/nucleon. Note that the Fe/O ratio values were only calculated for data points with the particle count >2 in the 1–hour time bin.

In order to obtain as many multispacecraft events as possible, when an event was detected by one spacecraft, I recorded Δt and $I_{\mathrm{Fe},max}$ for other two spacecraft, even if $\Delta t < 12$. In addition, I noted $I_{\mathrm{Fe},max}$ = Y for cases where the particle intensity increase was observed but the values were below the threshold values. If the Fe/O data were not available, I noted this case as "N". Finally, I noted the cases, where there were data gaps (dg) during an SEP event, or missing data (md), if the data were absent for the entire SEP event.

[14]During this period, the data from STEREO A particle instruments were of lower quality, with gaps in data or no data, from 19 August 2014 to 16 November 2015, while using the side–lobe antenna and during the major solar conjunction. No data were received from STEREO B after October 2014, when the spacecraft failed to reboot prior to its passage behind the Sun. Note that after the communication with STEREO A was established in July 2015, the STA/LET instrument is pointed perpendicular to the nominal Parker spiral field line.

Table 3.1: Details of Fe SEP events between 2006 and 2016 considered in this thesis. Year and day of year (DOY) are the intervals, during which Fe SEPs were measured above the threshold values for $\geq$12 1–hour intervals. Δt is the number of 1–hour intervals, during which Fe SEPs were measured above the threshold values. $I_{\mathrm{Fe},max}$ is the maximum Fe intensity in $(\mathrm{cm^2\,s\,sr\,MeV/nucleon})^{-1}$ units reached during an SEP event. $A_{\mathrm{Fe/O}}$ is the average Fe/O value calculated for the duration of an SEP event.

Event				STB			ACE			STA		
#	Year	DOY		Δt	$I_{\mathrm{Fe},max}$	$A_{\mathrm{Fe/O}}$	Δt	$I_{\mathrm{Fe},max}$	$A_{\mathrm{Fe/O}}$	Δt	$I_{\mathrm{Fe},max}$	$A_{\mathrm{Fe/O}}$
1	2006	339	347	72	1.2×10^{-2}	0.165	135	4.1×10^{-3}	0.055	73	1.4×10^{-2}	0.142
2	...	347	349	26	1.3×10^{-2}	1.100	45	9.9×10^{-3}	0.540	0^{md}	0	N
3	...	349	355	1	1.1×10^{-4}	N	19	2.3×10^{-5}	0.609	0^{md}	0	N
4	2011	80	87	0	Y	N	26	6.2×10^{-5}	0.376	0^{md}	0	N
5	...	155	158.3	0^{md}	0	N	34	3.4×10^{-5}	0.316	0^{md}	0	N
6	...	158.3	166	$>1^{\mathrm{dg}}$	1.1×10^{-4}	N	28	6.3×10^{-5}	0.249	$>2^{\mathrm{dg}}$	1.5×10^{-4}	N
7	...	216	220.5	0	Y	N	48	2.3×10^{-4}	0.165	0	0	N
8	...	221.3	224	0	0	N	13	9.3×10^{-5}	0.370	0	0	N
9	...	265	273	$>2^{\mathrm{dg}}$	1.1×10^{-4}	N	11	2.0×10^{-5}	0.101	1	1.6×10^{-4}	N
10	...	307	312	0	Y	N	0	Y	0.541	20	6.6×10^{-4}	0.418
11	...	330	333	0	0	N	29	4.9×10^{-5}	0.054	0	0	N
12	2012	23	27	0	Y	0.075^{*}	65	1.1×10^{-3}	0.014	4	1.1×10^{-4}	0.096^{*}
13	...	27	35	0	Y	N	72	1.2×10^{-3}	0.035	36	6.8×10^{-3}	0.113
14	...	64	67	17	2.2×10^{-4}	0.143	0	0	N	0	Y	N
15	...	67	73.6	61	8.0×10^{-3}	0.124	133	5.6×10^{-3}	0.081	23	2.2×10^{-4}	0.192
16	...	73.6	77	0	Y	N	31	7.2×10^{-4}	0.108	0	0	N
17	...	138	142	0	0	N	35	1.8×10^{-4}	0.195	0	0	N
18	...	147	150	0	0	N	0	Y	N	14	6.2×10^{-4}	0.135
19	...	189	190.5	0	0	N	24	5.8×10^{-5}	0.302	0	0	N
20	...	190.5	194	0	0	N	23	3.4×10^{-5}	0.606	1	2.2×10^{-4}	N
21	...	199	201	0	0	N	18	8.1×10^{-5}	0.081	0	0	N
22	...	201	205	0	0	N	43	1.9×10^{-4}	0.245	1	1.2×10^{-4}	N
23	...	205	212	10	1.8×10^{-4}	0.116	8	1.6×10^{-5}	0.064	49	5.1×10^{-2}	0.080
24	...	244	248	15	3.4×10^{-4}	0.045	0	Y	N	0	0	N
25	...	263	269	16	4.7×10^{-4}	0.239	0	Y	N	56	2.4×10^{-3}	0.140
26	...	271.9	276	0	Y	N	11	3.6×10^{-5}	0.323	0	0	N
27	2013	64	67	2	1.2×10^{-4}	0.183^{*}	0	Y	N	36	4.7×10^{-3}	0.130
28	...	101	105	24	8.7×10^{-4}	0.837	36	1.2×10^{-4}	0.377	0	0	N
29	...	133.6	137	37	1.9×10^{-3}	0.150	0	Y	N	0	0	N
30	...	135.4	138	0	Y	N	10	2.7×10^{-5}	0.038	0	0	N
31	...	142	147	0	0	N	58	1.1×10^{-3}	0.082	0	0	N
32	...	231.8	235	3	1.5×10^{-4}	0.116^{*}	0	Y	N	25	2.9×10^{-4}	0.046^{*}
33	...	273	276	0	0	N	43	1.5×10^{-4}	0.188	0	Y	N
34	...	278	281	0	Y	N	0	Y	N	11	3.3×10^{-4}	0.529
35	...	284	288	1	1.1×10^{-4}	N	0	Y	N	13	4.4×10^{-4}	1.230
36	...	301	304	0	Y	N	21	3.6×10^{-5}	0.478	0	0	N
37	...	306	308	0	Y	N	0	Y	N	20	5.6×10^{-4}	0.746
38	...	311	314	27	1.0×10^{-3}	0.046	0	Y	N	10	4.2×10^{-4}	0.223
39	...	362	365	0	Y	N	14	6.7×10^{-5}	0.671	0	0	N
40	2014	6	7.8	0	0	N	35	1.8×10^{-4}	0.709	0	0	N
41	...	7.8	14	0	Y	0.425^{**}	86	2.1×10^{-3}	0.069	$>4^{\mathrm{dg}}$	1.5×10^{-4}	0.137^{**}
42	...	55	65	80	3.5×10^{-3}	0.322	142	1.8×10^{-4}	0.208	34	7.9×10^{-4}	0.389
43	...	92	96	10	6.4×10^{-4}	0.500	0	Y	N	0	0	N
44	...	108	112	0	0	N	42	1.4×10^{-4}	0.173	0	0	N
45	...	244	253	67	2.3×10^{-2}	0.130	4	1.3×10^{-5}	0.256	$>8^{\mathrm{dg}}$	1.5×10^{-3}	N
46	...	253	257	0	Y	N	40	7.1×10^{-5}	0.241	0	0	N
47	...	268	271	22	5.0×10^{-4}	0.260	0	Y	N	$>5^{\mathrm{dg}}$	3.4×10^{-4}	N
48	...	287	295	0^{md}	0	N	0	Y	N	$>7^{\mathrm{dg}}$	1.5×10^{-3}	N
49	...	348	357	0^{md}	0	N	0	Y	N	$>16^{\mathrm{dg}}$	1.2×10^{-2}	0.075
50	2015	169	185	0^{md}	0	N	13	3.3×10^{-5}	0.078	0^{md}	0	N

$^{\mathrm{md}}$ missing data for the whole event
$^{\mathrm{dg}}$ partial data gap during an event
* average Fe/O value not calculated at 8–10 MeV/nucleon (STEREO/LET data only).
** average Fe/O value not calculated at 6–8 MeV/nucleon (STEREO/LET data only).

0 – as maximum intensity, no particle intensity increase was observed at the spacecraft
Y – as maximum intensity, a particle intensity increase at the spacecraft observed below the threshold value
N – as average Fe/O value, the average Fe/O value not calculated

3.2 Multispacecraft data

Table 3.1 contains details of 50 Fe SEP events that were observed between December 2006 and December 2016 above the threshold values 10^{-4} $(\mathrm{cm}^2\,\mathrm{s}\,\mathrm{sr}\,\mathrm{MeV/nucleon})^{-1}$ in the 10–12 MeV/nucleon channel for STEREO and 10^{-5} $(\mathrm{cm}^2\,\mathrm{s}\,\mathrm{sr}\,\mathrm{MeV/nucleon})^{-1}$ in the 10.7–15.8 MeV/nucleon channel for ACE.

Events #1, #2 and #3 occurred in December 2006 while the STEREO spacecraft were still near the Earth. No Fe SEP events at all were observed above the selected threshold values between 2007–2010 during the period of low solar activity. There are in total 47 Fe SEP events that were recorded in years 2011–2015, 8 events that occurred in 2011, 15 in 2012, 13 in 2013, 10 in 2014, and a single event in 2015. There were no SEP events recorded in 2016 that would satisfy all the criteria.

In two cases (events #15, #42) intensities above the threshold values for $\Delta t \geq 12$ were detected simultaneously at all three spacecraft, and in four cases (events #13, #23, #28, #38) at two spacecraft. These events are selected for further analysis in Section 4.1.

In ten cases (events #4–6, #9, #41, #45, #47–50) the particles with intensity above the threshold values were measured at one spacecraft but data gaps or missing data at another spacecraft prevented the events to be classified as a two– or three–spacecraft event.

Overall, including the events where the intensity increases were noted as "Y", there were 17 SEP events observed by three spacecraft, 19 events observed by two spacecraft, and 11 events observed by a single spacecraft.

The Fe threshold values ensure that there is sufficient count statistics to evaluate the Fe/O ratio. However, in one case (event #48) the average Fe/O value was not evaluated at either spacecraft due to data gaps. There are 36 SEP events (events #1–3 each count as a single event), at which the Fe/O value was evaluated at a single spacecraft. Out of these events, 26 are Fe–rich SEP events, i.e. $A_{\mathrm{Fe/O}} > 0.134$, and 10 events are Fe–poor, i.e. $A_{\mathrm{Fe/O}} < 0.134$. The Fe/O ratio was evaluated at two

spacecraft in 8 events, and by all three spacecraft in 5 events. With all 50 SEP events considered, 41 observations of SEP events were Fe–rich and 26 were Fe–poor.

There is an apparent bias towards Fe–rich events, which might be linked to the method used for calculating the Fe/O values in this work. The event–averaged Fe/O value, as used in this work, was calculated as the arithmetic average of all Fe/O data points, which correspond to >2 counts per the accumulation time for both Fe and O. The average SEP abundance in gradual events $A_{\mathrm{Fe/O}} = 0.134$, as determined by Reames (1995), was calculated as the integrated count of Fe particles normalised to the O particle count over 49 gradual events at 5–12 MeV/nucleon. Oxygen ions, as compared to Fe ions, are more likely to be observed due to the higher O than Fe abundance in SEP events, and the duration of O SEP events is typically longer as well. As a result, the particle detector is able to collect more O than Fe SEPs. The method for calculation of the event–averaged Fe/O ratio used throughout this work does not consider any O ions, where >2–count Fe intensity data points are not observed at the same time. Therefore, the Fe/O value calculated using the integration method, e.g. by Reames (1995, 1998), is expected be lower as compared to event–averaged Fe/O value used in this work.

In order to compare the two methods, event–integrated values were calculated for event #28 at ACE and STEREO B. The event–integrated Fe/O value at STEREO B $A_{\mathrm{Fe/O},int} = 0.701$ is lower than that obtained as event–averaged $A_{\mathrm{Fe/O},avg} = 0.837$, but similar to the value obtained by Cohen et al. (2014), 0.69, a behaviour that is expected. At ACE, $A_{\mathrm{Fe/O},int} = 0.364$, a value which is similar to the event–averaged Fe/O value, $A_{\mathrm{Fe/O},avg} = 0.377$, is lower than that obtained by Cohen et al. (2014), 0.48. It should be noted that Cohen et al. (2014) used a wider energy bin, 12–33 MeV/nucleon, to count Fe and O SEPs, and in this particular event the Fe/O value at ACE increased with energy, as can be seen in Figure 7 in Cohen et al. (2014).

In addition to events observed at two or three spacecraft, where $\Delta t \geq 12$, the Fe/O ratio was evaluated simultaneously at three spacecraft in events #12, #15,

#23, #41, #42 and at two spacecraft in events #10, #13, #25, #27, #28, #32, #38, #45. All of these events are also included in Table 3.1. The longitudinal dependence of Fe/O and other SEP parameters will be further discussed in Section 4.2.

3.2.1 Events #1, #2 and #3 (2006 DOY 339–355)

Events #1 (2006 DOY 339–347), #2 (2006 DOY 347–349) and #3 (2006 DOY 349–355) occurred while the STEREO spacecraft were still performing manoeuvres near the Earth. During this period of very high solar activity, 4 X–class flares erupted at the Sun from AR 10930: on 5 December at 10:18 UT (the start time of the flare), an X9.0 flare erupted at location S07E79 (latitude 7 ° south of the solar equator, longitude 79 ° east of the central meridian as seen from the Earth), followed by an X6.5 flare at S06E63 on 6 December at 18:29 UT, an X3.4 flare at S06W23 on 13 December at 02:14 UT, and an X1.5 flare at S06W46 on 14 December at 21:07 UT. Two halo CMEs were observed on 13 December at 02:54 UT with speed 1774 km/s and on 14 December at 22:30 UT with speed 1042 km/s. Information about possible other CMEs associated with the the flares is not available due to a data gap in the SOHO/LASCO data.

These events were the last strong events of the solar cycle 23 and were studied in more detail by other researchers, e.g. event #1 by Mewaldt et al. (2010), event #2 by Liu et al. (2008), event #3 by von Rosenvinge et al. (2009), and the events collectively by Mewaldt et al. (2008); Malandraki et al. (2009).

Figure 3.1 shows the Fe intensity time profiles by STEREO A (red) and B (blue) measured by the LET instruments at 10–12 MeV/nucleon and ACE/SIS (green) at 10.7–15.8 MeV/nucleon. The vertical solid lines indicate the flare start times. The horizontal dash–dotted lines are the intensity threshold values used for the identification of SEP events, $I_{\mathrm{Fe}} = 10^{-4}\,(\mathrm{cm^2\,s\,sr\,MeV/nucleon})^{-1}$ (cyan) for STEREO/LET and $I_{\mathrm{Fe}} = 10^{-5}\,(\mathrm{cm^2\,s\,sr\,MeV/nucleon})^{-1}$ (yellow) for ACE/SIS.

Fe SEPs in event #1 start increasing after the X9.0 flare erupted on 5 December (DOY 339.43), but the majority of the particles were most likely associated with

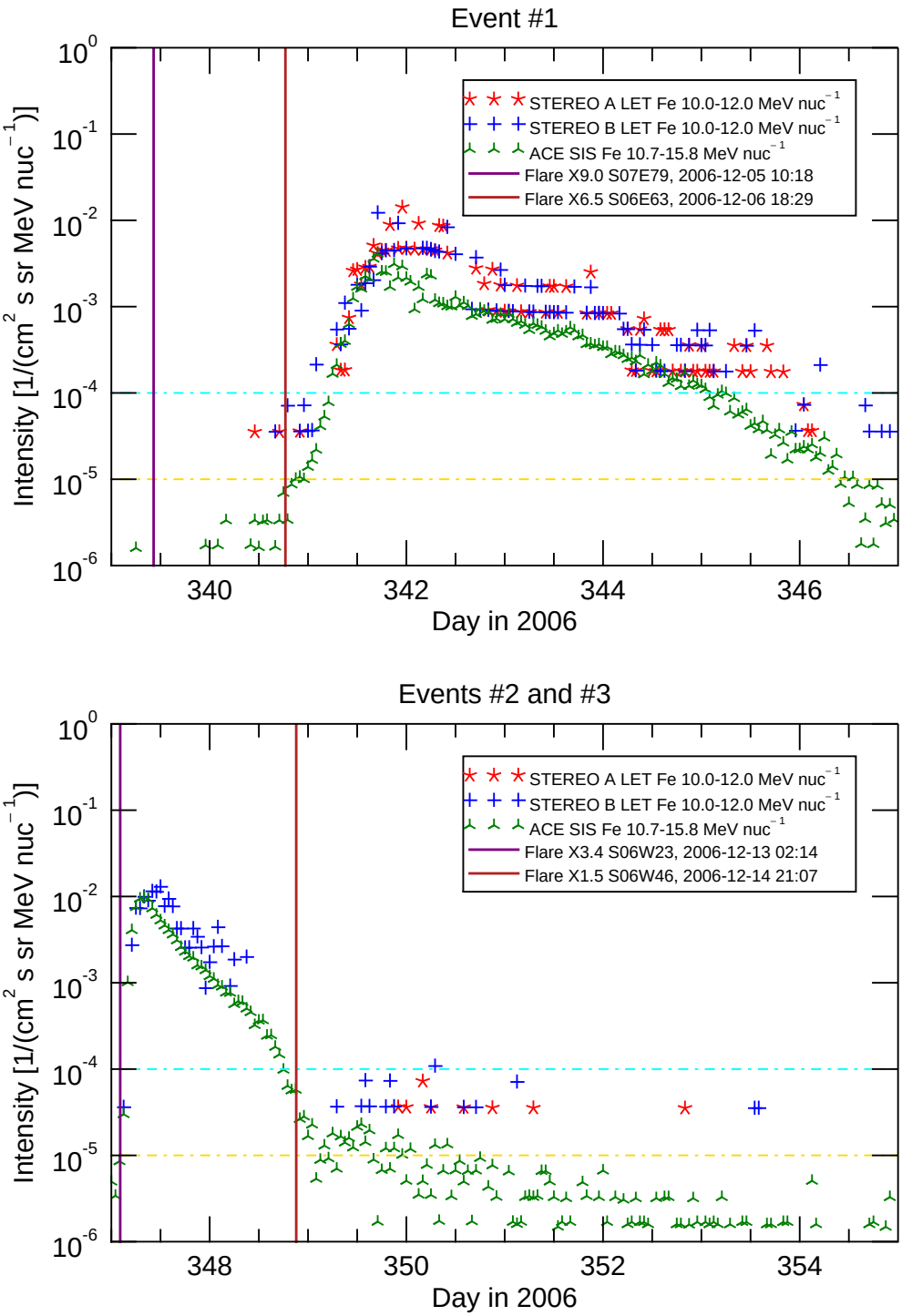

Figure 3.1: Fe intensity time profiles of events #1 (top), and #2 and #3 (bottom) for STEREO A/LET (red), STEREO B/LET (blue) and ACE/SIS (green). The vertical purple and brown lines denote the start time of the flares. The horizontal lines are the intensity threshold values for STEREO/LET (cyan) and ACE/SIS (yellow).

the X6.5 flare on 6 December (DOY 340.77), which was also the better magnetically connected event to the Earth ($\Delta\phi = -111\,^\circ$) than the X9.0 flare ($\Delta\phi = -162\,^\circ$), as noted by Mewaldt et al. (2008). Event #2 was caused by the X3.4 flare on 13 December (DOY 347.09) also from AR 10930, which by this time rotated to the longitude W23. A small increase of Fe particle intensity was observed after the X1.5 flare on 14 December (DOY 348.88). Unfortunately, the STEREO A/LET data for events #2 and #3 are missing.

The particle intensity time profiles measured by the three instruments during DOY 341.3–341.7, as seen in the top plot of Figure 3.1, show very similar values. However, later in the event, the ACE/SIS intensity keeps decreasing steadily, but the STEREO/LET intensities drop in steps. The particle count data show that these intensity data points correspond to low counts (e.g. 1, 2 or 3 counts per accumulation time). This indicates that the dynamic range, and as a result the sensitivity of the STEREO/LET instruments, changed during the SEP event.

Similarly, in the bottom plot of Figure 3.1 the ACE/SIS and STEREO B/LET intensities followed by the X1.5 flare are low and near the particle instrument sensitivity thresholds so that the quantisation of the particle intensity can be observed, and 1–, 2–, and 3–count intensity values can be resolved. Overall, the Fe intensities shown in Figure 3.1 show a good agreement among the three spacecraft.

A comparison of data measured by the STEREO/LET instruments with other particle instruments onboard ACE, GOES and SAMPEX using these particle events was done by Mewaldt et al. (2008) and Cohen et al. (2008). In each the two studies, the authors compared the proton and heavy ion, including oxygen and iron, spectra with those measured by other particle instruments. The measurements by the LET instruments also compare well within the measured spectral range of the data. In a different study, Richardson et al. (2014) showed that SEP measurements based on these events by the HET and ERNE instruments using $\sim$25 MeV protons compare well to each other, see Figure 3 in Richardson et al. (2014).

Therefore the data for events #1,2,3, at a time when the two STEREO spacecraft

and ACE were located at similar longitudes, show that intensities measured by the different particle instruments are in good agreement.

Chapter 4

Multispacecraft observations of heavy ion SEP events

Studies of SEP events that used multiple spacecraft, e.g. by Cohen et al. (2014), Lario et al. (2014) and Gómez–Herrero et al. (2015), showed that Fe SEPs can be observed simultaneously at spacecraft that are widely separated in longitude from each other. In addition, the SEP event analysed by Cohen et al. (2014) was found to be rich in Fe at two spacecraft well–separated from the parent active region and the Fe/O value was dependent on longitude.

Similarly to the aforementioned studies, Chapter 3 contains an Fe SEP event list where the events were observed by multiple spacecraft. Events in that list observed simultaneously at two or three spacecraft are analysed in Section 4.1. The longitudinal dependence of SEP parameters is presented in Section 4.2 and the summary of the observations is provided in Section 4.3. Section 4.4 includes the discussion to these results.

4.1 Analysis of selected multispacecraft events

For further analysis, I selected 6 SEP events, where $\Delta t \geq 12$ observed simultaneously at two (events #13, #23, #28, #38) or three spacecraft (events #15, #42). The details of the associated solar eruptive events are given in Table 4.1. In addition to these events, the table also contains the details for events, where the Fe/O values were evaluated at two spacecraft (events #10, #25, #27, #32, #45) and at three spacecraft (events #12, #41). Table 4.1, contains the properties of the flares and CMEs, and of the spacecraft. For each flare the day, the start time (including fractional DOY), the peak time (if known), the flare class and location are recorded. For CMEs, the time indicates when the CME was first observed in the LASCO instrument's field of view, and v_{CME} is the linear speed of a CME in the plane of sky in km/s. The central position angle (CPA), the measured position angle (MPA) and the CME angular width (dA) are important properties of a CME characterising its position in the plane of sky. CPA and MPA are measured anticlockwise from the solar northern direction in degrees. CPA is marked as "halo" when the apparent width of a CME is 360 °, i.e. the CME forms a halo around the solar disk, but the MPA value describes the angle of the fastest moving segment of a CME, even for halo CMEs. In ideal case the MPA and CPA values are equal (CDAW CME Catalog 2017). v_{sw} is the solar wind speed in km/s at the spacecraft at the start of the flare. The angle $\Delta\phi$ is longitudinal separation in degrees calculated using Equation 3.4 (positive is flare west of the spacecraft footpoint). The angle $\Delta\theta$ is the latitudinal separation in degrees (positive is flare north of the spacecraft).

Events #42 and #38 are further discussed in Section 4.1.1 and 4.1.2. Plots of SEP intensities and ionic ratios for additional events may be found in Appendix A.

4.1.1 Event #42 (2014 DOY 55–65)

On 25 February 2014 at 00:39 UT (DOY 56.03) an X4.9 flare erupted from AR 11990 at S12E77[1] and it was accompanied by a fast CME with a speed of 2147 km/s, ob-

[1]The position of the flare was identified at S13E82 in the CDAW CME Catalog.

Table 4.1: Details of solar eruptive events associated with SEP events observed simultaneously by multiple spacecraft. For each flare the day, start time (including fractional day of year (DOY)), peak time (if known), flare class and location are recorded. For associated CMEs, the time indicates when a CME was first observed by the LASCO instrument, v_{CME} is the linear speed in the plane of sky in km/s, CPA is the central position angle of the CME. Halo means that the angular CME width, dA measured in degrees, is 360 °. MPA is the measured position angle of the fastest moving element of the CME leading edge in degrees. v_{sw} is the solar wind speed at the spacecraft at the start of an SEP event in km/s, $\Delta\phi$ is longitudinal separation in degrees (positive is flare west of the spacecraft footpoint), $\Delta\theta$ is latitudinal separation in degrees (positive is flare north of the spacecraft).

Event		Flare						CME					STB			ACE			STA		
#	Year	Day	Start time (DOY)		Peak	Class	Location	Time	v_{CME}	CPA	dA	MPA	v_{sw}	$\Delta\phi$	$\Delta\theta$	v_{sw}	$\Delta\phi$	$\Delta\theta$	v_{sw}	$\Delta\phi$	$\Delta\theta$
10	2011	Nov 03	22:21	(307.93)	—	—	N08E155[a]	23:30	991	halo	360	90	448	–109	3	349	132	4	426	40	15
12	2012	Jan 23	03:38	(23.15)	03:59	M8.7	N28W21	04:00	2175	halo	360	326	349	61	35	450	–36	33	360	–157	31
13	2012	Jan 27	17:37	(27.73)	18:37	X1.7	N34W77[a]	18:27	2508	halo	360	296	449	134	27	519	28	40	420	–92	37
15	2012	Mar 07	00:02	(67.01)	00:24	X5.4	N18E31	00:24	2684	halo	360	57	351	14	14	370	–100	25	335	144	15
...	...	Mar 07	01:05	(67.05)	01:14	X1.3	N15E26	01:30	1825	halo	360	82	351	19	11	373	–94	22	330	147	12
23	2012	Jul 23	02:15	(205.09)	—	—	S15W134[a]	02:36	2003	halo	360	286	341	174	–8	435	75	–20	466	–42	–17
25[b]	2012	Sep 20	14:55	(264.62)	—	—	S15E156[a]	15:12	1202	halo	360	131	349	–112	–13	570	159	–22	402	16	–10
...	...	Sep 21	06:15	(265.26)	—	—	S10E147[a]	06:24	639	halo	360	46	379	–97	–8	432	154	–17	383	22	–4
27	2013	Mar 05	03:26	(64.14)	—	—	N11E146[a]	03:48	1316	halo	360	137	270	–101	5	375	146	18	345	9	6
28	2013	Apr 11	06:55	(101.29)	07:16	M6.5	N07E13	07:24	861	halo	360	85	342	54	5	390	–78	13	540	166	0
32	2013	Aug 19	22:50	(231.95)	—	—	N12W179[a]	23:12	877	halo	360	282	328	–121	19	438	121	5	408	–28	16
...	2013	Aug 20	07:55	(232.33)	—	—	S20W96[a]	08:12	784	halo	360	210	332	157	–13	409	34	–27	369	–118	–16
38	2013	Nov 07	10:15	(311.43)	—	—	N00E150[a]	10:36	1405	halo	360	89	582	–50	0	350	137	–4	530	13	6
41	2014	Jan 07	18:04	(7.75)	18:32	X1.2	S12W08	18:24	1830	halo	360	231	312	79	–19	392	–57	–5	361	146	–18
42	2014	Feb 25	00:39	(56.03)	00:49	X4.9	S12E77	01:25	2147	halo	360	73	571	38	–19	460	–132	–5	361	60	–18
45	2014	Sep 01	11:00	(244.46)	—	X2.1[c]	N14E129[a,d]	11:12	1901	halo	360	65	441	–26	21	448	174	7	417	3	21

[a] The position of the backside flare was calculated using STEREO FITS files.
[b] The source of Fe SEPs at STEREO B could not be reliably determined.
[c] The flare class for this event was estimated by Pesce–Rollins et al. (2015).
[d] The position of the flare was identified at N14E127 in the CDAW CME Catalog.

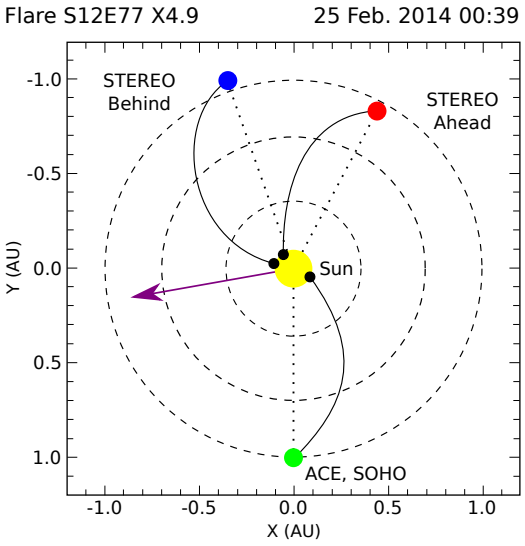

Figure 4.1: A diagram of the position of ACE and SOHO (green), STEREO A (red) and B (blue) in the helioequatorial at the time of the X4.9 solar flare on 25 February 2014 at 00:39 UT. The purple arrow indicates the radial direction of the solar flare.

served at 01:25 UT. An interplanetary shock associated with the ICME was observed at STEREO A on 25 February at 12:15 UT (DOY 56.51) and at ACE on 27 February at 15:50 UT (DOY 58.66). This event was studied in more detail by Lario et al. (2016).

The SEP event 2014 DOY 55–65 (event #42) was observed at all three spacecraft positions, see Figure 4.1. STEREO B was the best magnetically connected spacecraft with $\Delta\phi_{\mathrm{STB}} = 38\,^{\circ}$, followed by STEREO A $\Delta\phi_{\mathrm{STA}} = 60\,^{\circ}$ and ACE $\Delta\phi_{\mathrm{ACE}} = -132\,^{\circ}$. At the time of the flare, the STEREO spacecraft were separated by $47\,^{\circ}$ from each other, STEREO B from the Earth by –160 °, and STEREO A from the Earth by 153 °. Type III radio bursts were observed at all three spacecraft and were followed by type II radio bursts at Wind and STEREO B, but significantly weaker at STEREO A (Lario et al. 2016).

The top plot in Figure 4.2 shows that the 40–60 MeV proton intensities at both STEREO spacecraft rise rapidly after the start of the flare while the peak intensity at SOHO, for which this event is an eastern event, occurs $\sim 15 - 20$ hours after the flare start. The Fe particle intensities above the threshold value $I_{\mathrm{Fe}} = 10^{-4}\,(\mathrm{cm^2\,s\,sr\,MeV/nucleon})^{-1}$ at STEREO B lasted approximately 3 days, and at

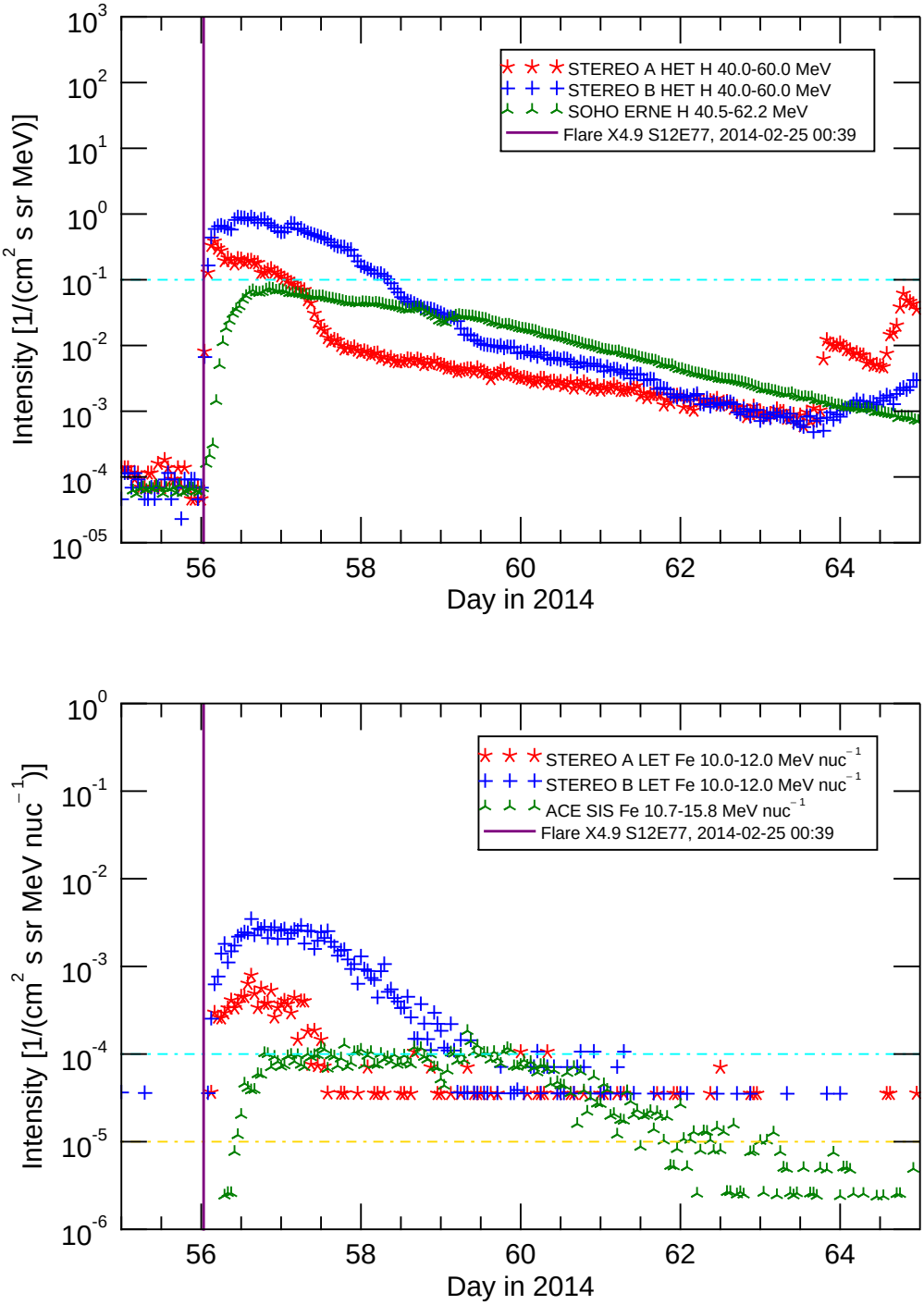

Figure 4.2: Particle intensity time profiles for event #42 (2014 DOY 55–65). Top plot: 40–60 MeV proton intensity for STA/LET (red), STB/LET (blue) and 40.5–62.2 MeV proton intensity for SOHO/ERNE (green). The cyan horizontal line is the proton intensity value $I_{\mathrm{H}} = 10^{-1}$ (cm^2 s sr MeV)$^{-1}$. Bottom plot: 10–12 MeV/nucleon Fe intensity for STA/LET (red), STB/LET (blue) and 10.7–15.8 MeV/nucleon Fe intensity for ACE/SIS (green). The vertical purple and brown lines denote the start time of the flares. The horizontal lines are the threshold values for STE/LET (cyan) and ACE/SIS (yellow).

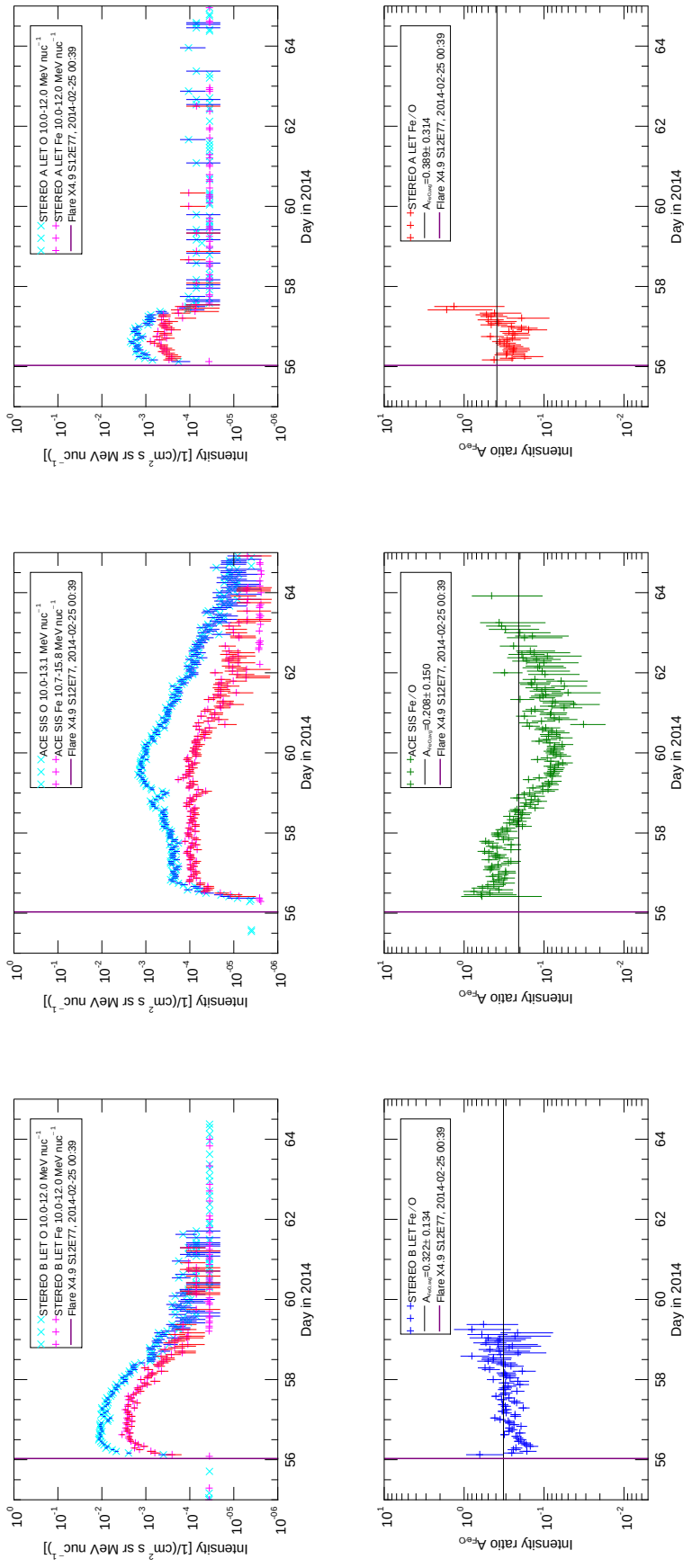

Figure 4.3: Top row: Intensities of O (blue) and Fe (red) measured at STEREO B (left), ACE (middle) and STEREO A (right) event #42 (2014 DOY 55–65). Bottom row: Fe/O ratio time profiles at the three spacecraft. The horizontal black line is the average Fe/O value at each spacecraft. The vertical purple line denotes the start time of the flare.

STEREO A only about 1.5 days, as seen in the bottom plot in Figure 4.2. The Fe SEP event at ACE, which lasted for almost 8 days, was probably affected by the ESP–related increase on DOY 58.66 as well as the corotation. The periods where $I_{\mathrm{H}} > 10^{-1}$ $(\mathrm{cm}^2\,\mathrm{s}\,\mathrm{sr}\,\mathrm{MeV})^{-1}$ are approximately similar to the periods where $I_{\mathrm{Fe}} > 10^{-4}$ $(\mathrm{cm}^2\,\mathrm{s}\,\mathrm{sr}\,\mathrm{MeV/nucleon})^{-1}$ at the STEREO spacecraft. While the proton intensity maximum at SOHO did not reach the $I_{\mathrm{H}} = 10^{-1}\,(\mathrm{cm}^2\,\mathrm{s}\,\mathrm{sr}\,\mathrm{MeV})^{-1}$ value, the Fe maximum intensity at ACE was $I_{\mathrm{Fe},max} = 1.8 \times 10^{-4}$ $(\mathrm{cm}^2\,\mathrm{s}\,\mathrm{sr}\,\mathrm{MeV/nucleon})^{-1}$, and lasted near the $I_{\mathrm{Fe}} = 10^{-4}$ $(\mathrm{cm}^2\,\mathrm{s}\,\mathrm{sr}\,\mathrm{MeV/nucleon})^{-1}$ value for approximately 3 days.

Fe and O intensity time profiles and the Fe/O values for the three spacecraft are shown in Figure 4.3. The average Fe/O value was calculated for each of the three spacecraft and is plotted as the black horizontal line in graphs in the bottom row of Figure 4.3. The best magnetically connected spacecraft STEREO B ($\Delta\phi_{\mathrm{STB}} = 38\,^\circ$) observed an Fe–rich event ($A_{\mathrm{Fe/O},avg} = 0.322$) as well as did ACE ($A_{\mathrm{Fe/O},avg}(\mathrm{ACE}) = 0.208$), even though the SEP event for ACE was an eastern event ($\Delta\phi_{\mathrm{ACE}} = -132\,^\circ$). However, STEREO A ($\Delta\phi_{\mathrm{STA}} = 60\,^\circ$), the spacecraft magnetically separated from the flare more than STEREO B, also observed an event rich in Fe $A_{\mathrm{Fe/O},avg}(\mathrm{STA}) = 0.389$ but with the Fe/O value higher than at STEREO B.

4.1.2 Event #38 (2013 DOY 311–314)

On 07 November 2013 at 10:15 UT (DOY 311.43) a back–side flare erupted from AR 11899 at N00E150[2] and it was accompanied by a CME with a speed of 1405 km/s, observed at 10:36 UT. A shock associated with an ICME was observed at STEREO B on 08 November at 18:28 UT (DOY 312.77).

The SEP event 2013 DOY 311–314 (event #38) was best observed at STEREO A and B, as seen in Figure 4.4. STEREO A was the best magnetically connected spacecraft ($\Delta\phi_{\mathrm{STA}} = 13\,^\circ$), followed by STEREO B ($\Delta\phi_{\mathrm{STB}} = -50\,^\circ$), and ACE and SOHO ($\Delta\phi_{\mathrm{ACE}} = 137\,^\circ$). At the time of the flare, the STEREO spacecraft were

[2]The position of the flare was identified at N02E151 in the CDAW CME Catalog.

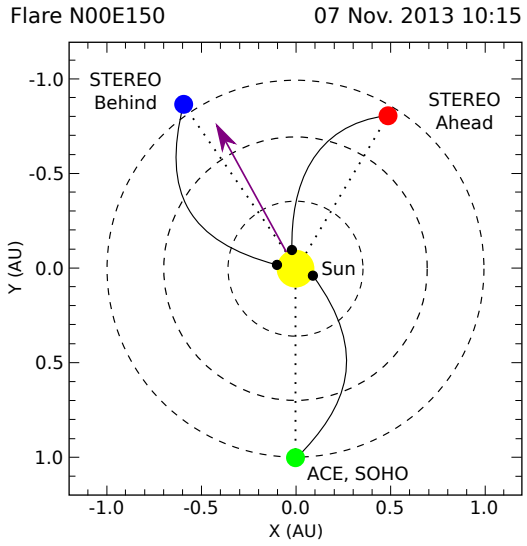

Figure 4.4: A diagram of the position of ACE and SOHO (green), STEREO A (red) and B (blue) in the helioequatorial at the time of the back–side solar flare on 07 November 2013 at 10:15 UT. The purple arrow indicates the radial direction of the solar flare.

separated by 68 °, STEREO B from the Earth by –143 °, and STEREO A from the Earth by 149 °. Type III radio bursts were observed at all three spacecraft, but the type II radio bursts were only observed at STEREO A and B.

The top plot of Figure 4.5 shows that the 40–60 MeV proton intensities at STEREO A rose rapidly after the start of the flare, followed by those at STEREO B. Unfortunately, the SOHO/ERNE data are missing during this period. The bottom plot of Figure 4.6 shows that the Fe particle intensity increase above the threshold value $I_{\mathrm{Fe}} = 10^{-4}\,(\mathrm{cm^2\,s\,sr\,MeV/nucleon})^{-1}$ at STEREO B lasted approximately 1.2 days, significantly longer than the Fe event at STEREO A, of approximately 10 hours. The periods of 40–60 MeV proton intensities $I_{\mathrm{H}} > 10^{-1}\,(\mathrm{cm^2\,s\,sr\,MeV})^{-1}$ as measured by the STEREO/HET instruments are again similar to the periods of 10–12 MeV/nucleon Fe intensities $I_{\mathrm{Fe}} > 10^{-4}\,(\mathrm{cm^2\,s\,sr\,MeV/nucleon})^{-1}$ measured by the STEREO/LET instruments. The Fe SEPs measured by the ACE/SIS instrument cannot be clearly associated with this event, and could be a part of the preceding event.

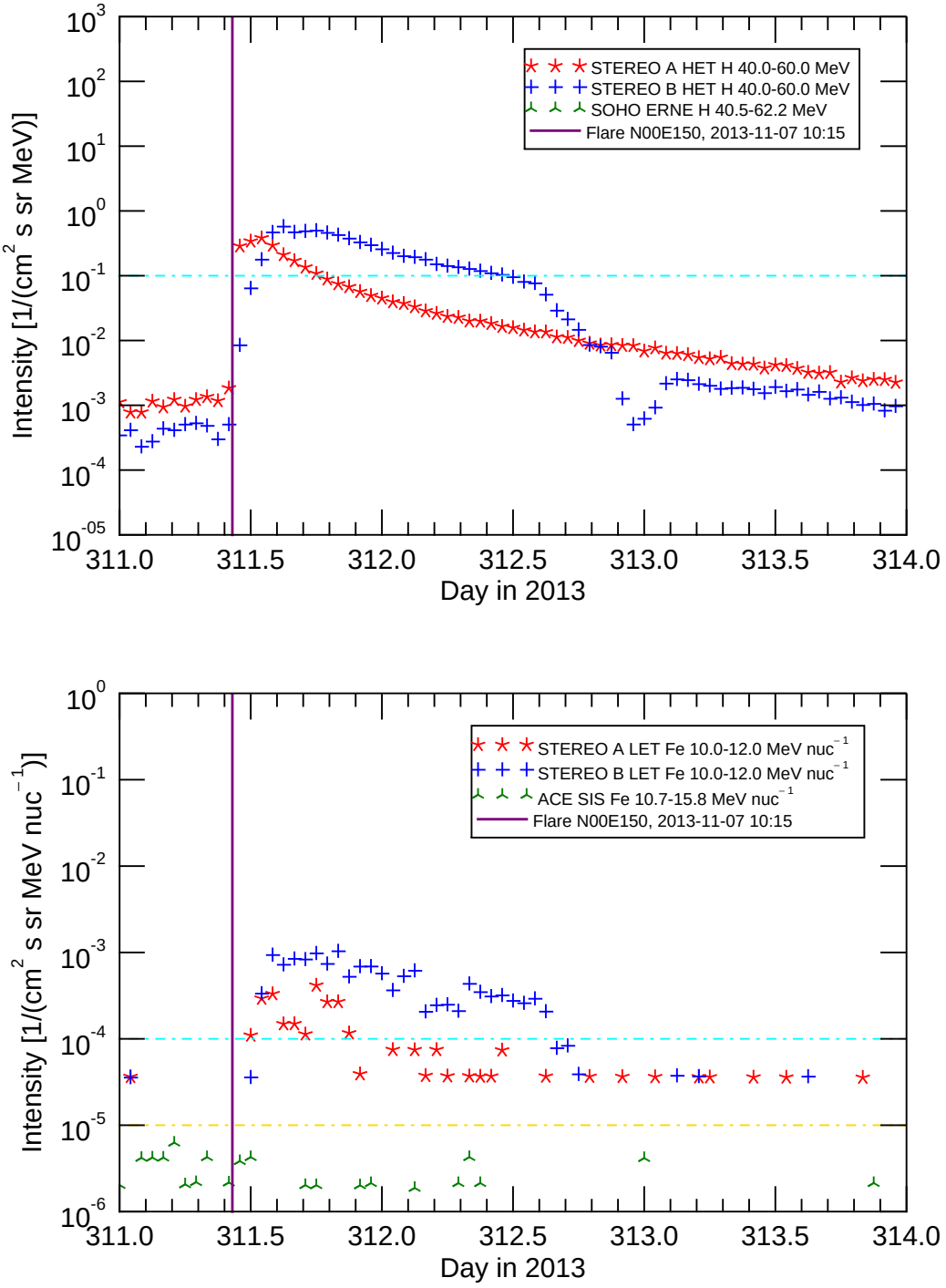

Figure 4.5: Particle intensity time profiles for event #38 (2013 DOY 311–314). Top plot: 40–60 MeV proton intensity for STA/LET (red), STB/LET (blue) and 40.5–62.2 MeV proton intensity for SOHO/ERNE (green). The cyan horizontal line is the proton intensity value $I_{\mathrm{H}} = 10^{-1}\,(\mathrm{cm^2\,s\,sr\,MeV})^{-1}$. Bottom plot: 10–12 MeV/nucleon Fe intensity for STA/LET (red), STB/LET (blue) and 10.7–15.8 MeV/nucleon Fe intensity for ACE/SIS (green). The vertical purple line denotes the start time of the flare. The horizontal lines are the threshold values for STE/LET (cyan) and ACE/SIS (yellow).

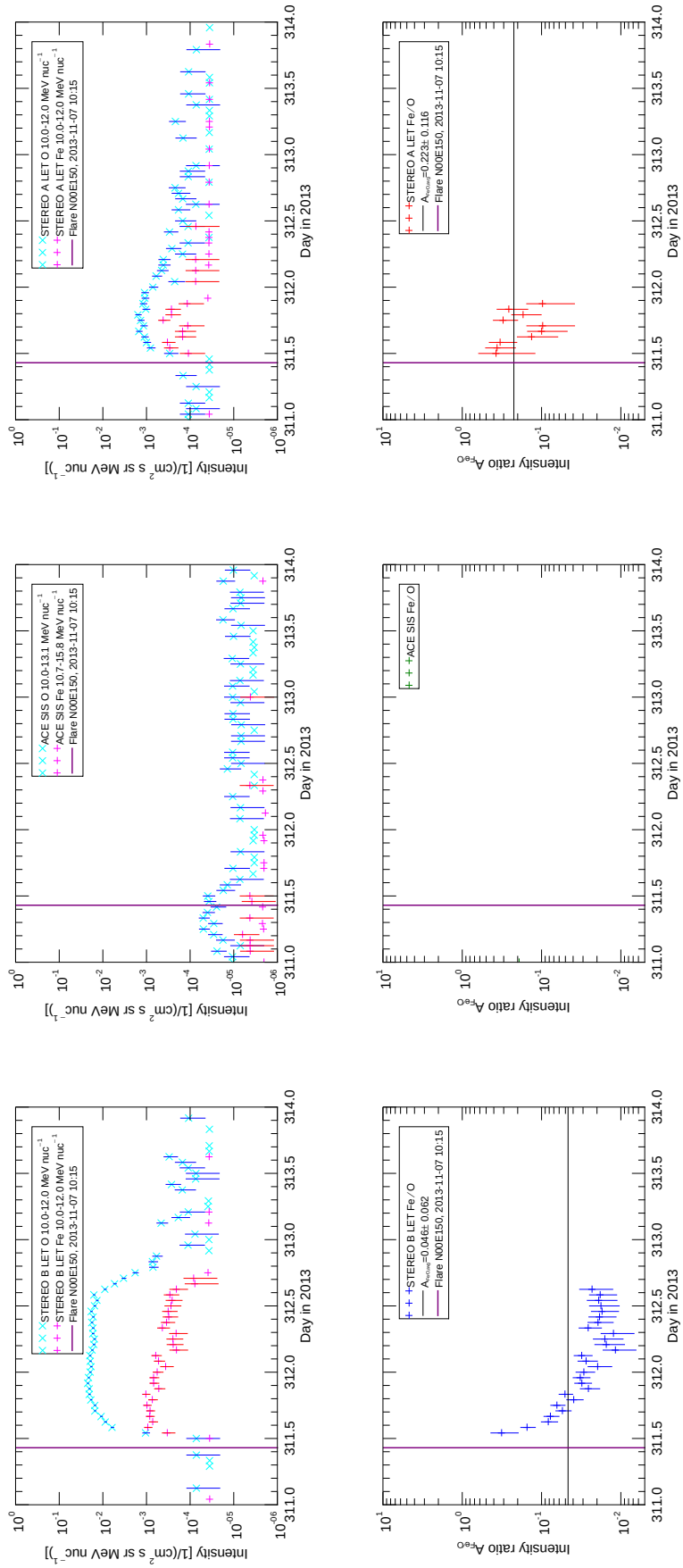

Figure 4.6: Top row: Intensities of O (blue) and Fe (red) measured at STEREO B (left), ACE (middle) and STEREO A (right) event #38 (2013 DOY 311–314). Bottom row: Fe/O ratio time profiles at the three spacecraft. The horizontal black line is the average Fe/O value at each spacecraft. The vertical purple line denotes the start time of the flare.

4.2 Longitudinal dependence of Fe SEP event parameters

A summary of the parameters of Fe SEP events observed simultaneously by two or three spacecraft is given in Table 4.2. These parameters were extracted from Table 3.1 and Table 4.1, with the addition of a parameter $\Delta\tau$, the number of 1–hour time intervals within intensity above $I_{\mathrm{Fe}} = 10^{-4}$ $(\mathrm{cm^2\,s\,sr\,MeV/nucleon})^{-1}$, i.e. the same threshold for STEREO/LET and ACE/SIS. For each SEP event, the spacecraft in Table 4.2 are organised by ascending $\Delta\phi$, the longitudinal separation between the flare and the magnetic footpoint of the spacecraft (s/c) on the solar surface. $I_{\mathrm{Fe},max}$ is the measured maximum Fe particle intensity value, and $A_{\mathrm{Fe/O}}$ is the event–averaged Fe/O value at each spacecraft. In addition, the table also contains the Fe/O values obtained from Cohen et al. (2014) for event #28.

Figure 4.7 shows graphs of the three parameters, $\Delta\tau$, $I_{\mathrm{Fe},max}$ and $A_{\mathrm{Fe/O}}$, plotted as a function of $\Delta\phi$. Data points corresponding to multi–point observations of the same event are connected by lines.

The time intervals are plotted as $\Delta\tau = 0$ for events where Fe SEPs were observed below the threshold values, $\Delta\tau(I_{\mathrm{Fe},max} = \mathrm{Y}) = 0$. For cases when maximum Fe intensities were below the threshold values, marked as $I_{\mathrm{Fe},max} = \mathrm{Y}$, the lower limit for maximum intensities is plotted as $I_{\mathrm{Fe}} = 10^{-5}$ $(\mathrm{cm^2\,s\,sr\,MeV/nucleon})^{-1}$ for STEREO/LET, and $I_{\mathrm{Fe}} = 10^{-6}$ $(\mathrm{cm^2\,s\,sr\,MeV/nucleon})^{-1}$ for ACE/SIS[3].

The top graph in Figure 4.7 shows the dependence of $\Delta\tau$ with $\Delta\phi$. When the solar event is eastern with respect to the spacecraft footpoint, $\Delta\phi < 0$ and when it is western $\Delta\phi > 0$. Overall, the time span $\Delta\tau$ of SEP events increases towards the location with the best magnetic connection, $\Delta\phi = 0$. In events #13, #15, #23, #38 and #41, the spacecraft for which the event was eastern observed SEPs for a longer time than the spacecraft for which the event was western. The middle data point

[3]The plotted intensity values estimated as the lower limits are values 1 order of magnitude below the threshold values used for the selection of Fe SEP events, $I_{\mathrm{Fe}} = 10^{-4}$ $(\mathrm{cm^2\,s\,sr\,MeV/nucleon})^{-1}$ for STEREO, and $I_{\mathrm{Fe}} = 10^{-5}$ $(\mathrm{cm^2\,s\,sr\,MeV/nucleon})^{-1}$ for ACE.

Table 4.2: A summary of the parameters of Fe SEP events from Table 3.1 and Table 4.1 observed simultaneously by two or three spacecraft. The spacecraft are arranged (from left to right) by increasing $\Delta\phi$, the longitudinal separation between the flare and the magnetic footpoint of the spacecraft (s/c) on the solar surface. $\Delta\tau$ is the number of 1–hour time intervals above $I_{\rm Fe} = 10^{-4}$ (cm^2 s sr MeV/nucleon)$^{-1}$, during which the Fe intensity was observed above the threshold values at STEREO/LET and ACE/SIS, $I_{{\rm Fe},max}$ is the measured maximum Fe particle intensity value, and $A_{\rm Fe/O}$ is the average Fe/O value at each spacecraft.

	Spacecraft 1					Spacecraft 2					Spacecraft 3				
Event #	$\Delta\phi$	s/c	$\Delta\tau$	$I_{{\rm Fe},max}$	$A_{\rm Fe/O}$	$\Delta\phi$	s/c	$\Delta\tau$	$I_{{\rm Fe},max}$	$A_{\rm Fe/O}$	$\Delta\phi$	s/c	$\Delta\tau$	$I_{{\rm Fe},max}$	$A_{\rm Fe/O}$
10	–109	STB	0	Y	N	40	STA	20	6.6×10^{-4}	0.418	132	ACE	0	Y	0.541
12	–157	STA	4	1.1×10^{-4}	0.096	–36	ACE	37	1.1×10^{-3}	0.014	61	STB	0	Y	0.075
13	–92	STA	36	6.8×10^{-3}	0.113	28	ACE	32	1.2×10^{-3}	0.035	134	STB	0	Y	N
15[a]	–100	ACE	105	5.6×10^{-3}	0.081	14	STB	61	8.0×10^{-3}	0.124	144	STA	23	2.2×10^{-4}	0.192
23	–42	STA	49	5.1×10^{-2}	0.080	75	ACE	0	1.6×10^{-5}	0.064	174	STB	10	1.8×10^{-4}	0.116
27	–101	STB	2	1.2×10^{-4}	0.183	9	STA	36	4.7×10^{-3}	0.130	146	ACE	0	Y	N
28	–78	ACE	4	1.2×10^{-4}	0.377	54	STB	24	8.7×10^{-4}	0.837	166	STA	0	0	N
28[b]	–77	ACE	...	...	0.48	58	STB	...	...	0.69	166	STA	...	...	N
32[c]	–121	STB	3	1.5×10^{-4}	0.116	–28	STA	25	2.9×10^{-4}	0.046	121	ACE	0	Y	N
38	–50	STB	27	1.0×10^{-3}	0.046	13	STA	10	4.2×10^{-4}	0.223	137	ACE	0	Y	N
41	–57	ACE	46	2.1×10^{-3}	0.069	79	STB	0	Y	0.425	146	STA	>4[e]	1.5×10^{-4}[e]	0.137
42	–132	ACE	25	1.8×10^{-4}	0.208	38	STB	80	3.5×10^{-3}	0.322	60	STA	34	7.9×10^{-4}	0.389
45	–26	STB	67	2.3×10^{-2}	0.130	3	STA	72[e]	1.5×10^{-3}[e]	N[dg]	174	ACE	0	1.3×10^{-5}	0.256

[a] The first flare on 07 March 2012 starting at 00:02 UT is used to determine the magnetic connection to the spacecraft.
[b] The event–integrated Fe/O ratio value for event #28 as evaluated by Cohen et al. (2014).
[c] The flare and CME on 19 August 2013 are the most likely sources of particles observed at STEREO A and B.
[dg] Partial data gap during an event.
[e] The $\Delta\tau$ and $I_{{\rm Fe},max}$ values are the lower limit estimates using the partial SEP time profiles.

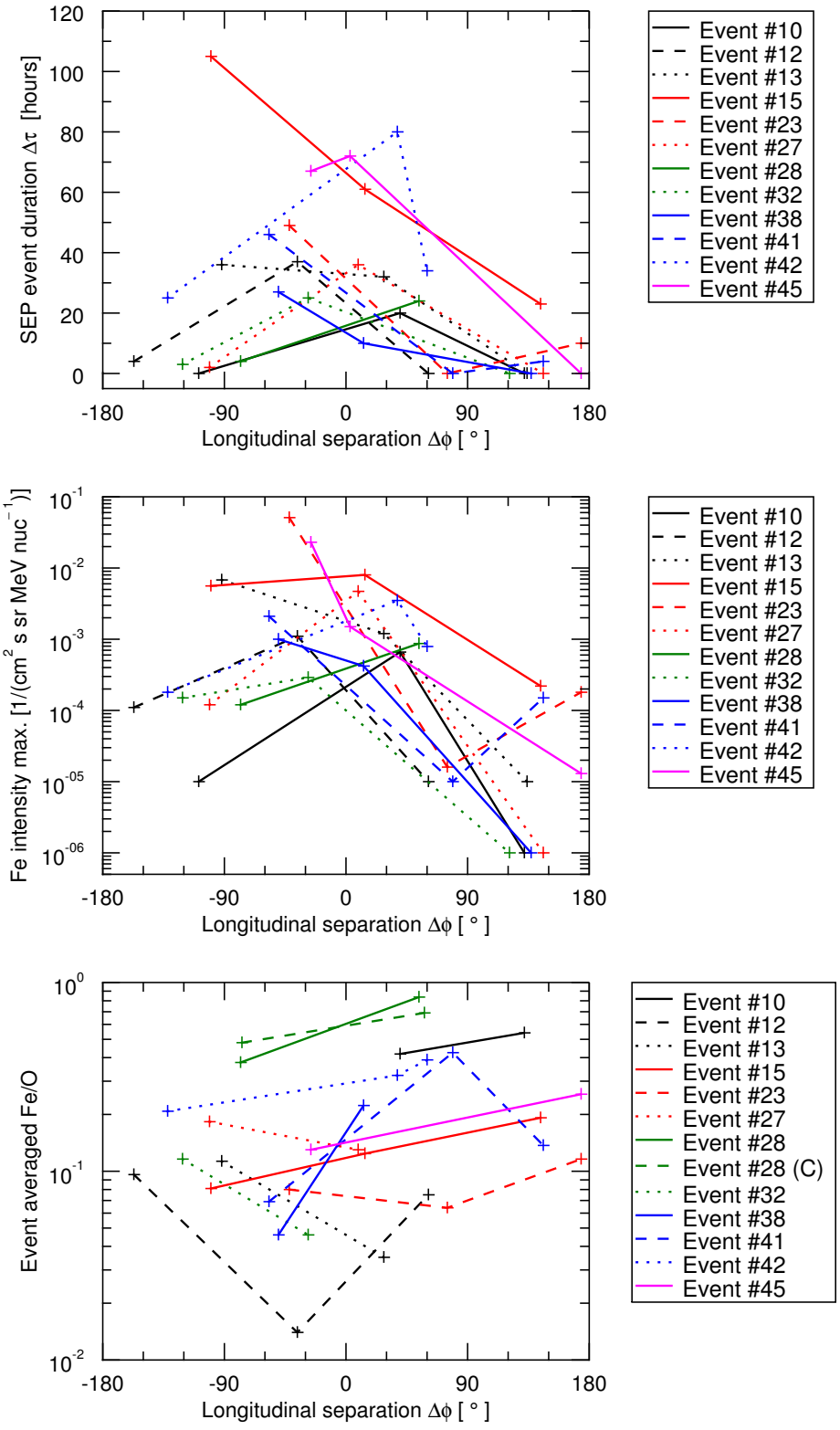

Figure 4.7: Parameters of Fe SEP events, $\Delta\tau$, $I_{\mathrm{Fe},max}$ and $A_{\mathrm{Fe/O},avg}$, observed simultaneously by two or three spacecraft plotted versus the longitudinal separation of the spacecraft $\Delta\phi$. $\Delta\tau(I_{\mathrm{Fe},max} = 0) = 0$ and $A_{\mathrm{Fe/O},avg} = \mathrm{N}$ are not plotted. $\Delta\tau(I_{\mathrm{Fe},max} = \mathrm{Y}) = 0$ (or the intensity is known) is plotted as $\Delta\tau = 0$. The Fe intensity $I_{\mathrm{Fe},max} = \mathrm{Y}$ is plotted as $I_{\mathrm{Fe},max} = 10^{-5}$ $(\mathrm{cm}^2\,\mathrm{s\,sr\,MeV/nucleon})^{-1}$ for STEREO/LET, and $I_{\mathrm{Fe},max} = 10^{-6}$ $(\mathrm{cm}^2\,\mathrm{s\,sr\,MeV/nucleon})^{-1}$ for ACE/SIS.

for event #45 is included in this graph and the $\Delta\tau$ value is estimated as the lower limit.

The middle graph in Figure 4.7 shows the dependence of $I_{\mathrm{Fe},max}$ with $\Delta\phi$. The spacecraft with the best magnetic connection to the parent active region typically observes the highest peak intensities, except for cases such as events #13 and #38, where the highest peak intensity was observed by a spacecraft that saw the event as eastern. Peak intensities often are reduced by orders of magnitudes at the less well connected spacecraft, a result that is well known for protons (e.g. Lario et al. 2013; Richardson et al. 2014). The middle data point for event #45 is included in this graph and the $I_{\mathrm{Fe},max}$ value is estimated as the lower limit.

The bottom graph in Figure 4.7 shows the dependence of $A_{\mathrm{Fe/O},avg}$ with $\Delta\phi$. The average Fe/O ratio values in any event vary less than approximately 1 order of magnitude, compared to the overall variation of the Fe/O values in the 12 events, which is $\approx$2 orders of magnitude. In addition, the Fe/O values obtained from Cohen et al. (2014) are also included in this graph, which are noted as event #28 (C), albeit measured as event–integrated Fe/O at $12-33$ MeV/nucleon. The middle data point for event #45 at $\Delta\phi = 3\,^\circ$ is excluded due to a partial data gap.

A variety of profiles of longitudinal dependence of Fe/O can be seen in Figure 4.7. In some events a high Fe/O value is observed near $\Delta\phi = 0$, e.g. event #38, while in others the Fe/O values are lower near $\Delta\phi = 0$, such as in events #10, #13, #27 and #32. It is not clear why the observers with magnetic connection closer to the flare, i.e. $\Delta\phi = 0\,^\circ$, would observe Fe/O values that are lower than those measured at other longitudes. SEP events, where high Fe/O values were observed over a wide range of longitudes, are events #10 and #28.

4.3 Summary of the results

In this chapter I studied the observations of Fe SEP events detected by three spacecraft, ACE, STEREO A and B. The results of this study provide observational evi-

dence that $\approx 10 - 15$ MeV/nucleon Fe SEPs can reach locations in the heliosphere that are not at all magnetically well–connected to the source region, see e.g. event #12 observed by STEREO A, event #23 observed by STEREO B and event #45 observed by ACE in Table 4.2. However, the onset of these particle increases at the remote locations is typically observed $\sim 1 - 3$ days after the flare eruption and the intensity peaks $\sim 2 - 4$ days after the flare. An example of such observations are the Fe and O SEP time profiles during event #23 shown in Figure A.9 in Appendix A.

Fe SEP events, as defined in this work and observed by the LET and SIS instruments, can last for as long as 142 hours, see e.g. event #42 measured by ACE/SIS in Figure 4.2. O SEP events typically have higher peak intensities and last longer than Fe SEP events.

The Fe/O ratio was evaluated simultaneously at three spacecraft in events #12, #15, #23, #41, #42 and at two spacecraft in events #10, #13, #25, #27, #28, #32, #38, #45. Out of 67 Fe/O ratio observations, 41 were Fe–rich and 26 were Fe–poor.

In events analysed in Section 4.1 it can be seen that the duration of 40–60 MeV proton intensities $I_{\mathrm{H}} > 10^{-1}$ $(\mathrm{cm}^2\,\mathrm{s}\,\mathrm{sr}\,\mathrm{MeV})^{-1}$, and the duration of 10–12 or 10.7–15.8 MeV/nucleon Fe intensities at $I_{\mathrm{Fe}} > 10^{-4}$ $(\mathrm{cm}^2\,\mathrm{s}\,\mathrm{sr}\,\mathrm{MeV/nucleon})^{-1}$ are often similar. The Fe peak intensities are lower by 2–4 orders of magnitudes compared to those of protons at 40–60 MeV, depending on the Fe abundance in an SEP event. A similar behaviour was observed when the Fe intensities were compared to 60–100 MeV proton intensities $I_{\mathrm{H}} > 10^{-2}$ $(\mathrm{cm}^2\,\mathrm{s}\,\mathrm{sr}\,\mathrm{MeV})^{-1}$.

Figure 4.7 shows the longitudinal dependence of SEP parameters $\Delta\tau$, $I_{\mathrm{Fe},max}$ and $A_{\mathrm{Fe/O},avg}$. The duration of Fe SEP events is typically longer for spacecraft, for which the eruption occurs near the central meridian from their point of view. As expected, the maximum Fe intensity peaks near the region that is magnetically well–connected to the parent active region, but in some events a higher peak intensity was measured by the spacecraft for which the event was eastern. Event–averaged Fe/O values in some events are higher at a remote spacecraft than at a well connected spacecraft,

e.g. in events #10, #13, #27 and #32. High Fe/O values were observed over a wide range of longitudes in events #10 and #28.

The time profiles of the Fe/O ratio display a variation in time, i.e. a decrease (STEREO B in events #38 and #42), but this behaviour sometimes occurs in the presence of a shock (STEREO A in events #13 and #23, ACE in event #42). In other cases the Fe/O time profiles do not change significantly over the duration of SEP events, e.g. at ACE in events #13, #15 and #28 and STEREO B in event #28. The time dependence of Fe/O and other heavy ion ratios will be studied as the primary objective in the following chapter.

4.4 Discussion

Out of a total of 50 Fe SEP events in Table 3.1, for the study of the longitudinal dependence of Fe/O in SEP events, I considered 12 SEP events, where the Fe/O ratio was calculated simultaneously at two or three spacecraft. In further 10 events, partial data gaps prevented the events being classified as two– or three–spacecraft events.

The event–averaged Fe/O values $A_{\mathrm{Fe/O}}$ are plotted as a function of the longitudinal separation angle $\Delta\phi$ in the bottom graph in Figure 4.7. The average Fe/O values in any individual event vary by less than approximately 1 order of magnitude, compared to the overall variation of the Fe/O values in 14 events, which is $\approx$2 orders of magnitude.

In a study of SEP abundances, Reames (1995) found that the Fe/O abundances showed a variation between 0.01 and 1.0, in different events observed by a single spacecraft. In order to eliminate the event–to–event variation, it is crucial to consider SEPs originating in a single eruptive event measured simultaneously by multiple spacecraft.

According to the two–class paradigm (Reames 1999), impulsive and gradual events are characterised by different source plasma and physical mechanisms that

accelerate SEPs. Therefore, within this picture, the two types of events exhibit different characteristics when observed at 1 AU. Impulsive events, associated with solar flares, are typically observed in a narrow longitudinal distribution centered near the observer's magnetic footpoint, and are rich in Fe and ^{3}He. SEPs in gradual events are accelerated from the corona by a CME–driven shock and injected onto magnetic field lines over a wide range of longitudes. The average Fe/O abundance ratio of gradual events $A_{\mathrm{Fe/O}} = 0.134$ (Reames 1995) is similar to that found in the corona via spectroscopic remote sensing.

Large SEP events are often associated with both solar flares and CMEs. Cane et al. (2003) suggested that two components, impulsive and gradual, can co–exist in SEP events, and the measured Fe/O value depends on the longitudinal separation between the observer and the flare. In a study of 29 SEP events, Cane et al. (2003) used observations by ACE/SIS, which were divided based on the characteristics of the intensity time profiles and Fe/O value into three groups. They suggested that SEPs observed in group 1 (having intensity time profiles that rose rapidly and decayed more slowly, with high Fe/O at the beginning of the event and event–averaged Fe/O enhanced over the coronal value) originated from solar flares, and those in group 2 (having rounded intensity time profiles and much lower Fe/O in the event) were accelerated by CME–driven shocks, i.e. by two separate mechanisms, and that SEPs from each mechanism only populated a range of longitudes, with the overlap represented by the SEP events in group 3. They concluded that it is the acceleration mechanism, a solar flare versus a CME–driven shock, that is responsible for producing Fe–rich and Fe–poor populations, and that observers placed ideally at a range of longitudes would detect either, or both, components depending on their longitudinal separation from the SEP source.

Tylka et al. (2005) suggested that the shock geometry can play a role in the observed longitudinal dependence of Fe/O, where SEPs accelerated by the quasi–perpendicular shock, typically found at the flanks of the CME–driven shock, create Fe–rich SEP abundances with $A_{\mathrm{Fe/O}} \approx 1$, while quasi–parallel at the nose of the

shocks are responsible for Fe–poor abundances with $A_{\mathrm{Fe/O}} \approx 0.1$. However, they conclude that further investigation and modelling is needed to determine the shock geometry near the Sun.

Cohen et al. (2013) studied the longitudinal dependence of Fe/O in 12 SEP events, and found that in 5 events the Fe/O value was higher at a remote, rather than a well connected, observer. Three of 12 events were used in a follow–up study by Cohen et al. (2014), where they studied the longitudinal dependence of Fe/O in total 4 Fe–rich SEP events observed simultaneously by two or three spacecraft, including those noted as events #4, #10 and #28 in this study. In spite of no magnetically well–connected observers within $|\Delta\phi| < 15\,^{\circ}$, they noted that in one of the events (event #4 in this study) the less well–connected spacecraft observed a higher Fe/O value that was Fe–rich. Cohen et al. (2013) and Cohen et al. (2014) concluded that the observed longitudinal dependence of Fe/O could not be clearly explained by either scenario proposed by Cane et al. (2003) and Tylka et al. (2005). However, Cohen et al. (2013, 2014) noted that the proposed mechanisms were not exhaustive, and that other factors, such as longitudinally–dependent particle seed population or the interplanetary transport, could contribute to the observed Fe/O values.

In the bottom panel in Figure 4.7, the plot of $A_{\mathrm{Fe/O},avg}$ versus $\Delta\phi$ shows event #38 with high Fe/O value observed near $\Delta\phi = 0$, as well as events where the Fe/O values are lower near $\Delta\phi = 0$, and higher at a remote spacecraft, such as events #10, #13, #27 and #32. In event #42, STEREO A, which was further separated from the flare than STEREO B, observed a higher Fe/O value (see Figure 4.3).

It should be noted that these measurements are not fully comprehensive because in many cases there was no observer at the site with the best magnetic connection, $\Delta\phi = 0$. It is also important to consider that Fe particle intensities measured at remote spacecraft are often near the particle instrument sensitivity thresholds.

On the one hand, the observed Fe/O values in events such as #38 (high Fe/O at a well connected observer) agree with the scenario put forth by Cane et al. (2003),

which is also consistent with that of Reames (1999). On the other hand, the Fe/O observations in events such as #13, #27 and #32 (high Fe/O at a remote observer), cannot be well understood within the framework of the two–class paradigm. Even though these SEP events were Fe–poor, it is not clear why the observers with magnetic connection closer to the flare, i.e. $\Delta\phi = 0\,^{\circ}$, would observe Fe/O values that are lower than those measured at other longitudes. SEP events where high Fe/O values were observed over a wide range of longitudes are events #10 and #28, but the observed longitudinal dependence of Fe/O does not agree with the two–class paradigm, under which Fe–rich events should only be detected at longitudes near the well connected region.

It should be noted that ^{3}He abundances were not used in this study to rigorously classify events as impulsive or gradual. Cohen et al. (2014) noted that in some cases SEP events rich in Fe were not necessarily rich in ^{3}He. Moreover, contrary to the expectations from the paradigm, in a study of ^{3}He rich events detected by multiple spacecraft, Wiedenbeck et al. (2013) reported an impulsive event that was observed by three spacecraft, two of which were separated by 136 °, but as part of a statistical study of 17 impulsive events they showed that simultaneous SEP detections at two spacecraft at longitudinal separation $>60\,^{\circ}$ were not uncommon.

If perpendicular diffusion is present and it depends on the Larmor radius of particles, then Fe would be expected to arrive to an observer at large $\Delta\phi$ earlier than O, but it is not clear how this will affect the Fe/O ratio integrated over the entire event. We do not know what kind of distribution of Fe/O as a function of $\Delta\phi$ would be produced by perpendicular diffusion associated with turbulence in the solar wind. Further modelling would be required to address these points.

The higher Fe/O values detected at a remote observer, such as in events #12, #13, #27 and #32, are potentially consistent with a perpendicular transport mechanism that can distribute Fe ions in longitude more effectively than O ions at the same energy/nucleon. Full–orbit simulations of heavy ions showed that drifts are an important mechanism of perpendicular transport that can distribute SEPs across

the interplanetary magnetic field (Marsh et al. 2013) that is m/q–dependent (Dalla et al. 2013). In a recent study, Dalla et al. (2017a) showed that the propagation of test particles within a Parker spiral magnetic field model occurs in 3D and the drift produces a significant transport across the mean magnetic field. Therefore, particles with larger m/q values exhibit more drift, e.g. Fe (at typical charge state values) would drift more than O, which is nearly fully ionised. The drift could result in a higher average Fe/O value at a remote observer, however, further study of this phenomenon using the test particle propagation model is desired.

Chapter 5

Time dependence of heavy ion ratios

In this chapter, I will quantitatively analyse the temporal variation of heavy ion SEP ratios, especially that of Fe/O seen in the data in Chapter 3.

Parts of this chapter were published as unrefereed contribution to *The 34th ICRC Conference Proceedings* (Zelina et al. 2015), in which we established that the decreases in Fe/O are a common feature of SEP events. In a refereed article published in *The Astrophysical Journal* (Zelina et al. 2017), a copy of which is included as Appendix B, we studied and quantitatively analysed the m/q dependence of heavy ion ratios in SEP events. In both articles, I carried out the data analysis and wrote the manuscript. Co–authors contributed to the writing of the manuscript.

Possible causes of the m/q dependence of temporal profiles of ratios in the context of transport mechanisms that include drifts, were reported in *Astronomy & Astrophysics* (Dalla et al. 2017b). A copy of this article is included as Appendix C. In this article, I am the third autor and I contributed to discussion and to the writing of the manuscript.

SEP ionic charge states are discussed in Section 5.1 and the parameters of the study in Section 5.2. The results of the study, including examples of SEP events, are

presented in Section 5.3. The summary of the results is given in Section 5.4 and the discussion in Section 5.5.

5.1 Ionic charge states in SEP events

Heavy ion SEPs in the interplanetary medium are partially ionised, but the measurement of the charge q is challenging, and is not routinely carried out for all events at SEP energies (Klecker et al. 2006b). Knowledge of the charge state of heavy ions is an important quantity to determine the ion m/q ratio. In the analysis below, for the purpose of calculating the m/q values, we use charge state measurements by Luhn et al. (1985), shown in Table 5.1. These values are a set of ionic charge states averaged over 12 large SEP events during 1978–79 in the energy range $\approx 0.5 - 3.3$ MeV/nucleon. This set has been used in many SEP studies over the years, including Tylka et al. (1999), and is derived at the lower end of the SEP energy range used in this study. The charge state measurements given in Luhn et al. (1985) are subject to systematic errors of 5%, but variable conditions in the space environment cause event to event variation in ionic charge states. The generally accepted value for the charge of Fe ions in gradual events is $Q_{\mathrm{Fe}} \approx 14$ (Reames 1999), but there are reports of Fe charge state values as high as $Q_{\mathrm{Fe}} \approx 21.5$ at energies ≈ 50 MeV/nucleon (Luhn & Hovestadt 1987; Labrador et al. 2001), that are typically ascribed to flare acceleration processes. Other ionic charge states vary too but to a lesser extent. Additionally, it should be noted that Q can vary event to event and in some SEP events it increases with energy (Klecker et al. 2006b; Mewaldt et al. 2006).

The Fe charge state value for event #2 (2006 DOY 347–349), $Q_{\mathrm{Fe}} = 16.2^{+1.7}_{-1.5}$ at $25 - 90$ MeV/nucleon was estimated from the SAMPEX data (Zelina et al. 2017), using the same method described by Oetliker et al. (1997). Therefore it can be said that for this event, the value of Q_{Fe} at the lower energies that we consider in this study, as given in Table 5.1, is not inconsistent with the measured value at

Table 5.1: Atomic mass number M, ionic charge state value Q, M/Q of abundant SEP ions, and temperature T. The ionic charge states are from Luhn et al. (1985) except for H and He, which are assumed to be fully ionised. The heavy ion charge state values are subject to 5% systematic uncertainty. The temperatures, as determined by Arnaud & Rothenflug (1985), correspond to the equilibrium between ionization and recombination, at which the ions obtain given average charge states.

Element	M	Q	M/Q	T [MK]
H	1	1.00	1.00	>0.03
He	4	2.00	2.00	>0.2
C	12	5.70	2.11	1.6
N	14	6.37	2.20	2.0
O	16	7.00	2.29	2.5
Ne	20	9.05	2.21	5.0
Mg	24	10.70	2.24	6.3
Si	28	11.00	2.55	1.6
Fe	56	14.90	3.76	2.0

Table 5.2: Table of S values, for all common pairs of abundant SEP elements.

		Element (2)							
		He	C	N	O	Ne	Mg	Si	Fe
Element (1)	H	2.00	2.11	2.20	2.29	2.21	2.24	2.55	3.76
	He	1	1.05	1.10	1.14	1.10	1.12	1.27	1.88
	C	...	1	1.04	1.09	1.05	1.07	1.21	1.79
	N	...	...	1	1.04	1.01	1.02	1.16	1.71
	O	...	0.92	0.96	1	0.97	0.98	1.11	1.64
	Ne	...	...	...	...	1	1.01	1.15	1.70
	Mg	...	...	...	...	...	1	1.13	1.68
	Si	...	...	...	...	...	...	1	1.48

Note: Ratio = $\frac{\text{Element(2)}}{\text{Element(1)}}$.

higher energies. To the best of our knowledge there were no operational instruments measuring ionic charges in the other SEP events.

For each pair of SEP elements X_1 and X_2, a parameter S was defined given by

$$S_{X_2/X_1} \equiv \left(\frac{M_2}{Q_2}\right) \Big/ \left(\frac{M_1}{Q_1}\right) \tag{5.1}$$

where M_i is atomic mass number and Q_i is the ionic charge state in elementary charge units, for species X_i.

We use the atomic mass number of the dominant isotope as a mass estimate for an SEP species. The difference between this value and the isotopic SEP compositions, e.g. given by Anders & Grevesse (1989), is estimated to be $\leq 2\%$, but it is substantially less than the uncertainty in SEP charge state. Using the mass and charge state values in Table 5.1, we consider all combinations of ionic ratios and calculate their S–value. The corresponding values are shown in Table 5.2.

5.2 Observations of SEP events

SEP events from Table 3.1 with Fe intensity $I_{\mathrm{Fe},max} > 10^{-4}$ $(\mathrm{cm^2\,s\,sr\,MeV/nucleon})^{-1}$ at 10−12 MeV/nucleon for STEREO/LET and 10.7−15.8 MeV/nucleon for ACE/SIS were considered and examined for the purposes of this study. The list of selected events is given in Table 5.4. A higher intensity threshold was chosen to ensure sufficient count statistics necessary to quantify the time dependence of ionic ratios.

For each selected event, time intensity profiles for all abundant elements, which include H, He, C, N, O, Ne, Mg, Si and Fe, were analysed and ionic ratios constructed. For ratios observed by STEREO/LET, the lowest energy channel common for all elements that is $4.0 - 4.5$ MeV/nucleon was used. ACE/SIS energy channels do not cover exactly the same energy range as STEREO/LET for any of the heavy ions. Therefore, the closest available channels to the STEREO/LET energy channel were used. Note that the heavy ion energy bins in ACE/SIS data change depending on the analysed element due to the SIS instrument response function for the

Table 5.3: Table of energy channels for ionic pairs used for the near–Earth spacecraft.

Ratio	Element(2)	Energy bin(2)	Element(1)	Energy bin(1)
C/O	C	6.4–8.6 MeV/nuc.	O	7.3–10.0 MeV/nuc.
Mg/O	Mg	8.7–12.2 MeV/nuc.	O	10.0–13.1 MeV/nuc.
Si/O	Si	9.2–13.0 MeV/nuc.	O	10.0–13.1 MeV/nuc.
Fe/Si	Fe	10.7–15.8 MeV/nuc.	Si	9.2–13.0 MeV/nuc.
Fe/Mg	Fe	10.7–15.8 MeV/nuc.	Mg	12.2–16.0 MeV/nuc.
Fe/C	Fe	10.7–15.8 MeV/nuc.	C	11.2–13.4 MeV/nuc.
He/H	He	3.4–4.7 MeV/nuc.	H	3.5–4.1 MeV
O/H	O	7.3–10.0 MeV/nuc.	H	8.1–10.1 MeV
Fe/H	Fe	10.7–15.8 MeV/nuc.	H	13.8–14.6 MeV

Note: Ratio $= \frac{\text{Element(2)}}{\text{Element(1)}}$.

analysed nuclei, see Figure 19 in Stone et al. (1998). Proton measurements from SOHO/ERNE were used to complement the heavy ion data by ACE/SIS.

The energy channels for a pair of two elements were chosen to be the closest to each other, e.g. in order to obtain the Fe/O ratio, Fe intensity at 10.7–15.8 MeV/nucleon was divided by O intensity measured at 10.0–13.1 MeV/nucleon. Energy channels for other ionic pairs used in this study at the near–Earth spacecraft are given in Table 5.3.

5.3 Time dependence of heavy ion ratios

5.3.1 Event #24 (2012 DOY 244–248)

A filament eruption occurred in the south–eastern region of the solar disk as viewed from Earth on 31 August 2012 (DOY 244) and launched a CME with linear speed 1442 km/s. An associated C8.4 X–ray flare at S16E42 started at 19:45 UT (DOY 244.82) and peaked at 20:43 UT (Gallagher et al. 2002). A shock passed the STEREO B spacecraft on 3 September at 07:11 UT (DOY 247.30). As viewed from Earth the flare and the CME were not particularly strong or fast but they caused a significant particle event at STEREO B with magnetic connection $\Delta\phi = -5\,^{\circ}$.

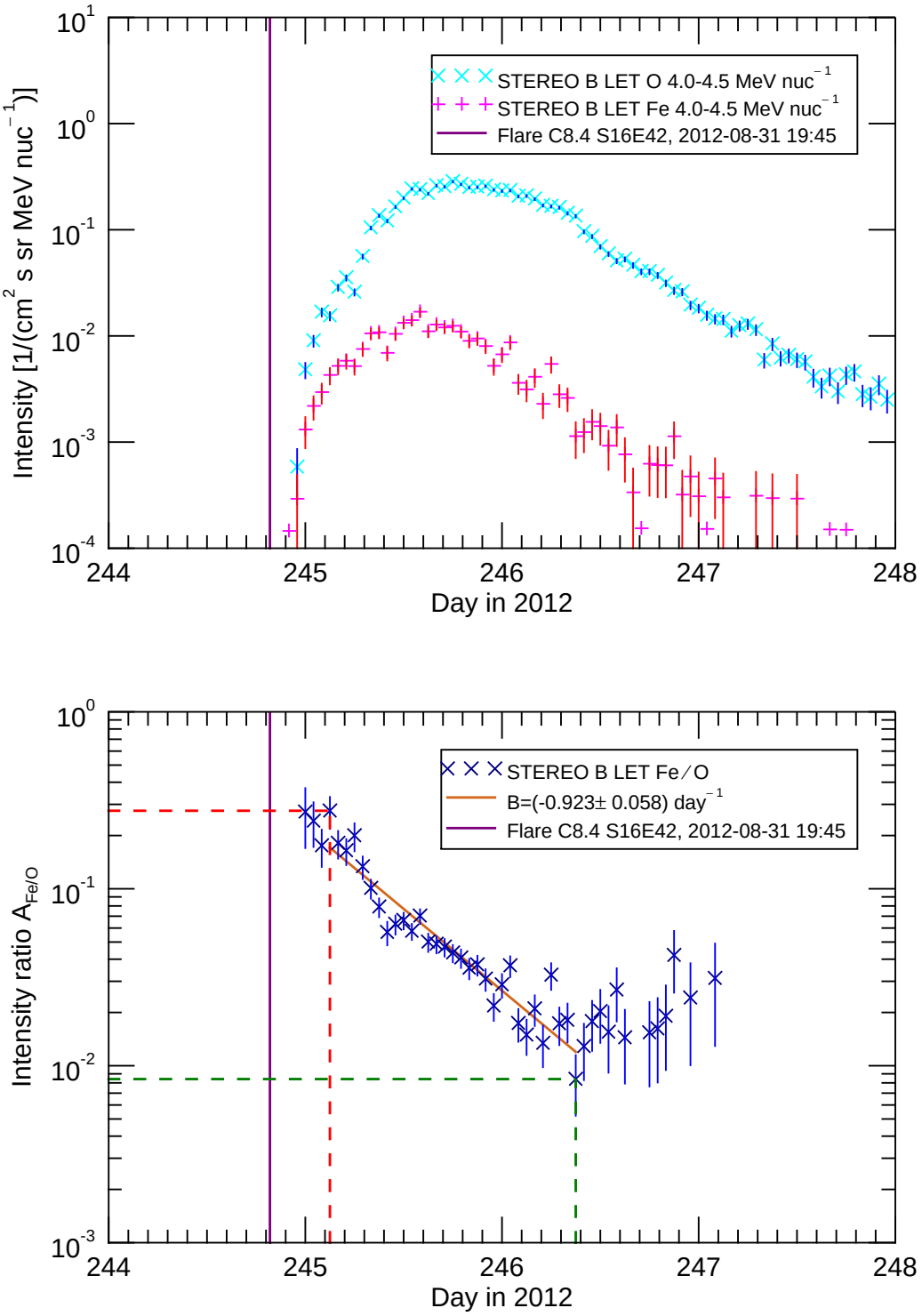

Figure 5.1: Top graph: Fe (magenta) and O (cyan) intensity for event #24 measured at 4.0–4.5 MeV/nucleon by STEREO B/LET. Bottom graph: Fe/O intensity ratio. The SEP ratio data (blue) are overplotted with the fitted exponential function (brown) given by Equation 5.2, where B is the time constant for changes in ion ratio. The line of best fit was fitted to the data in the period Δt, indicated by the dashed lines of the maximum (red) and minimum (green) data point. The vertical purple line denotes the start time of the flare.

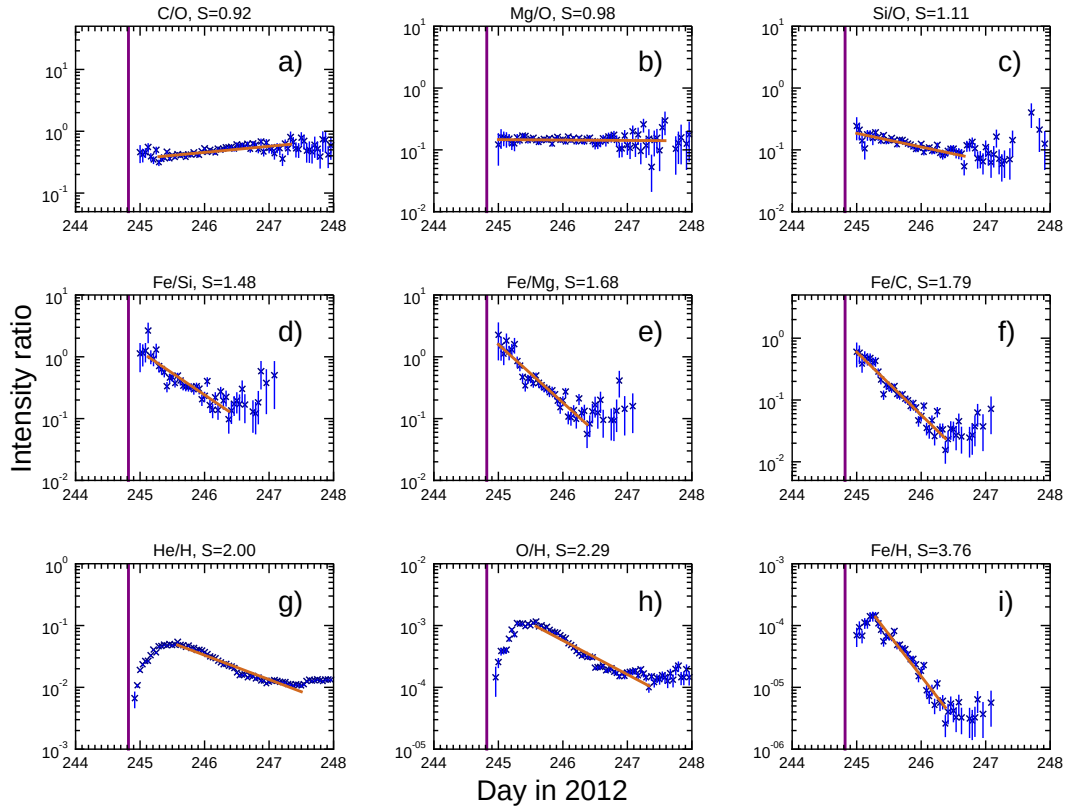

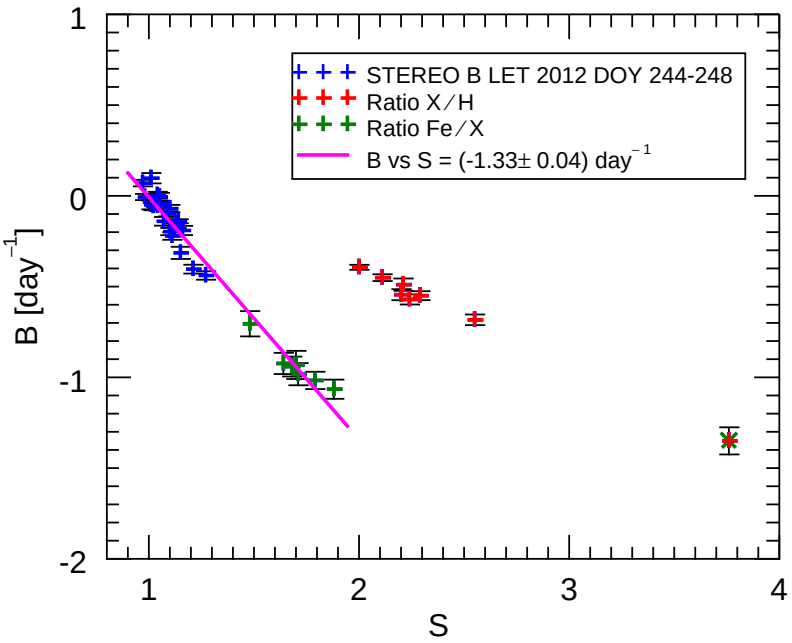

Figure 5.2: Top panels: A succession of SEP ratios with ascending S values (see Table 5.2) for event #24. The SEP ion intensities were measured by STEREO B/LET at 4.0–4.5 MeV/nucleon. The SEP ratio data (blue) in time interval between the maximum and the minimum are overplotted with the fitted function (brown). All intervals on the vertical axes are scaled equally to 3 orders of magnitude. Bottom panel: Time constant values B plotted as a function of S. The monotonic dependence shows that more decrease is observed in ratios with increasing S. A discontinuity is observed at $S = 2.0$.

The event #24 (2012 DOY 244–248) could in many respects be considered an exemplary proton SEP event. Oxygen and iron particle intensity–time profiles and Fe/O ratio are shown in Figure 5.1. The particle intensities show a rapid increase followed by a gradual decrease with smooth profile and no significant shock–associated particle intensity component observed over 10 days after the flare. The intensity of oxygen peaks later than that of iron and the oxygen SEP event lasts longer. The Fe/O ratio, shown in the bottom panel of Figure 5.1, is decreasing from values typical of impulsive events to values more than 1 order of magnitude below the average gradual event abundance of 0.134 (Reames 1995). This event would be classified as Fe–poor with event–averaged Fe/O value $A_{avg}(\mathrm{Fe/O}) = 0.064$. The Fe/O decrease occurred over $\Delta t_{\mathrm{Fe/O}} = 1.25$ days. After Fe/O reaches its minimum, it increases for the next $\sim$1 day. Considering the intensity profiles of Fe and O, it is apparent that the increase is a result of the low Fe counts at the limit of the instrument's sensitivity.

For the same event, the top panels in Figure 5.2 show 9 SEP ratio plots versus time for a number of ion pairs. Heavy ion ratios are calculated as the ratio of two particle intensity values I, e.g. $A_{\mathrm{Fe/O}} = I_{\mathrm{Fe}} \big/ I_{\mathrm{O}}$. Panels (a)–(i) are ordered by increasing S values, where S is the ratio defined in Equation 5.1, for the pair under consideration. The heavy ion ratios are plotted over a 4–day period, during which the temporal evolution of heavy ion ratios takes place. From a qualitative point of view, the time variation of the ratio displays a correlation with S: a ratio shows decrease (increase) in time when $S > 1$ ($S < 1$). The ratio profiles also show that the slope of temporal variation scales with S, where e.g. Mg/O shown in Figure 5.2(b), a ratio with $S \approx 1$, remains almost unchanged over the duration of the SEP event. The C/O ratio with $S = 0.92$, Figure 5.2(a), shows a slight but steady increase over time, and the Si/O ratio with $S = 1.11$ shows a decrease, Figure 5.2(c). The duration of Si/O evolution is also shorter than that of C/O or Mg/O due to the lower relative abundance of silicon in the SEP event. These three ratios show far less variation than the ratios with high values of S, i.e. Fe/Si, Fe/Mg and Fe/C, Figure 5.2 panels (d),

(e) and (f), all of which have larger values of S that $S_{\mathrm{Si/O}}$. Ratios of elements with respect to hydrogen, e.g. He/H, O/H and Fe/H are somewhat anomalous, showing an initial increase followed by a decrease, as can be seen in the last row of Figure 5.2 in panels (g), (h) and (i). The decay rate of Fe/H is higher than that of O/H, which is higher than He/H, therefore increasing with increasing S of an SEP ratio. The decay period is shorter for Fe/H than it is for O/H and He/H respectively, due to relative abundances of the elements in the SEP event. The initial increase is observed in all X/H ratios.

Quantitative analysis

A quantitative analysis of the temporal variation of heavy ion ratios in the SEP events was carried out as follows. The bottom graph in Figure 5.1 shows the Fe/O ratio in event #24 at $4.0 - 4.5$ MeV/nucleon over a 4–day period. Ratio data points used in further analysis are those that have more than 2 particle counts in a 1–hour time bin for both ion species. An input to the analysis is the time range after the start of the flare Δt between the maximum (red) and minimum (green) data points, over which data should be fitted. We marked the first occurring maximum or minimum data point within Δt as A_1, and the last occurring as A_2. When the Fe/O ratio decreases over time, the maximum precedes the minimum and $A_2/A_1 < 1$, but other heavy ion ratios may show an increase over time, i.e. $A_2/A_1 > 1$. All the data points between the maximum and the minimum were fitted using the function

$$A = 10^{\alpha + Bt} \tag{5.2}$$

where B is the time constant for changes in ion ratio in units of day^{-1}, and α is a unitless fitting constant. For the example of Figure 5.1 the time constant value, obtained using Equation 5.2, is $B_{\mathrm{Fe/O}} = (-0.92 \pm 0.06)$ day^{-1}. In a similar manner, the values of B were obtained for all abundant ratios considered in Table 5.2.

In the bottom graph in Figure 5.2 we plot the time constant values B as a function of S for all SEP ratios in event #24. The plot shows a quantitative description of

the qualitative behaviour seen in the top graph. Between $S = 0.9$ and $S = 2$ a monotonic decrease of B with S is observed corresponding to faster decay rates as S increases. Ratios of Fe to other heavy ions, Fe/X, are plotted as green data points. There is a discontinuity present at $S = 2.0$, the S value for He/H, followed by another monotonic decrease. As can be seen from Figure 5.2, the ratios with $S \geq 2$, plotted as red data points, are the ratios of a heavy ion and hydrogen, X/H.

The location of the data points along the horizontal axis is influenced by the values of the charge states Q that are used to calculate S. We analysed how S values change when different values of Q_{Fe}, the Q value that can vary by the largest amount, are considered. The S value for Fe/O in our plot is $S = 1.64$. This value changes to $S = 2.04$ when $Q_{\mathrm{Fe}} = 12$ and $S = 1.36$ when $Q_{\mathrm{Fe}} = 18$. If the Fe charge changed, ionic charges for all the other ions would change too, therefore it is not easy to quantify the effect on the B vs S plot unless charge states for the event for all ions were available.

For this event, the B versus S dependence in the interval $S \in [0.9, 2.0)$, considering 28 unique ionic ratios, has the slope value $-1.33 \pm 0.04\,\mathrm{day}^{-1}$.

5.3.2 Event #2 (2006 DOY 347–349)

Event #2 (2006 DOY 347–349), also previously discussed in Section 3.2.1, was associated by an X3.4 flare at S06W23, which started at 02:14 UT (DOY 347.09) and peaked at 02:40 UT, and was accompanied by a CME with speed 1774 km/s. An interplanetary shock passed ACE on 14 December at 14:14 UT (DOY 348.59). Heavy ion particle intensity profiles for event #2 are shown in Figure 5.3. Event #2 was followed by another SEP event on 14 December at 22:14 UT, therefore the analysed period was cut off on 15 December 2006 (DOY 349). At the time of the flare, the magnetic connection of ACE was $\Delta\phi = -17\,^{\circ}$.

Event #2 shows similar Fe/O profile as event #24, where a decrease can be observed over the duration of the SEP event, but the decay of Fe/O cannot be well described as a single power law. The oxygen intensity, more significantly that

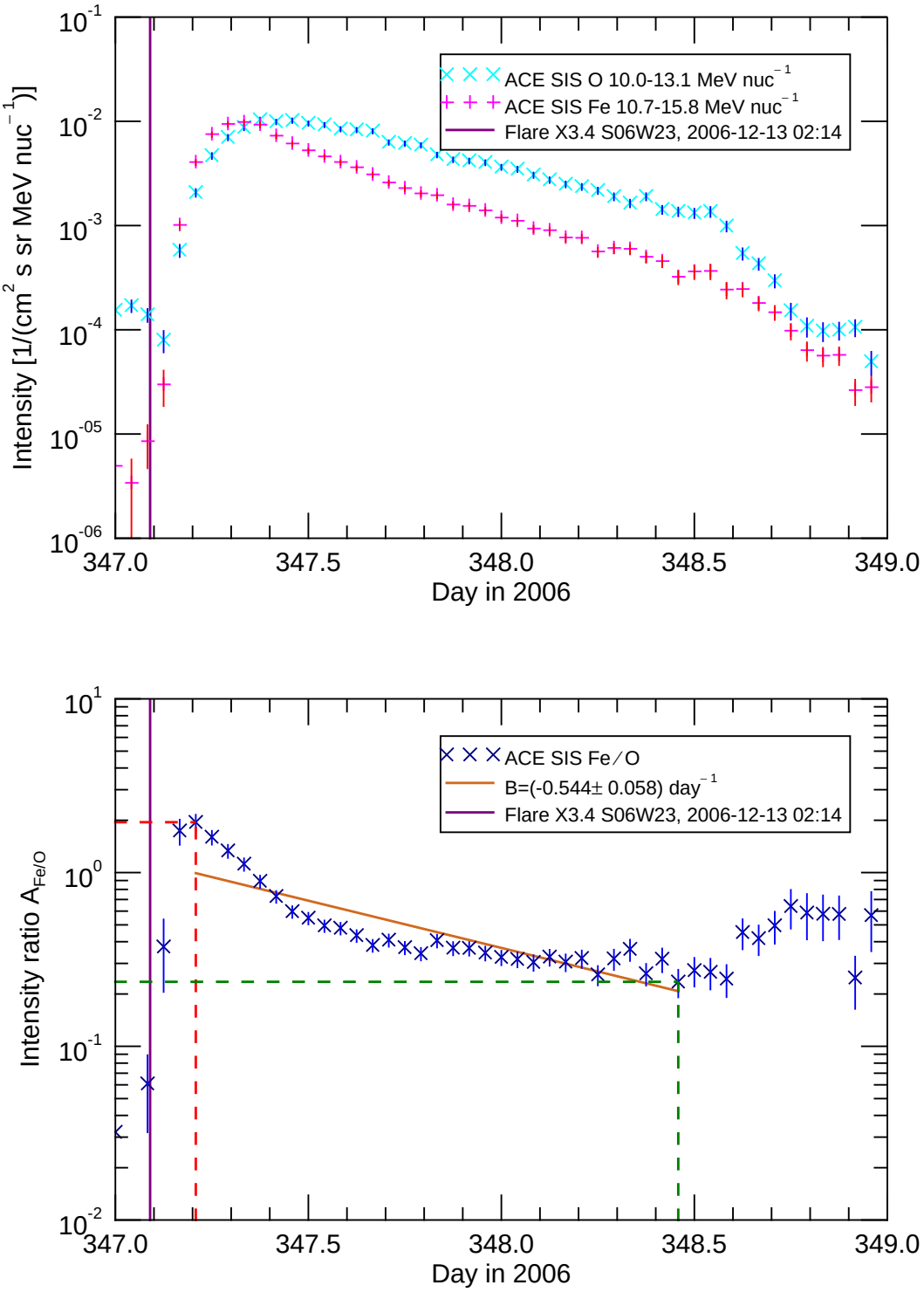

Figure 5.3: Top graph: Fe intensity (magenta) at 10.7–15.8 MeV/nucleon and O (cyan) intensity at 10.0–13.1 MeV/nucleon measured by ACE/SIS for event #2. Bottom graph: Fe/O intensity ratio. The SEP ratio data (blue) are overplotted with the fitted exponential function (brown) given by Equation 5.2, where B is the time constant for changes in ion ratio. The line of best fit was fitted to the data in the period Δt, indicated by the dashed lines of the maximum (red) and minimum (green) data point. The vertical purple line denotes the start time of the flare.

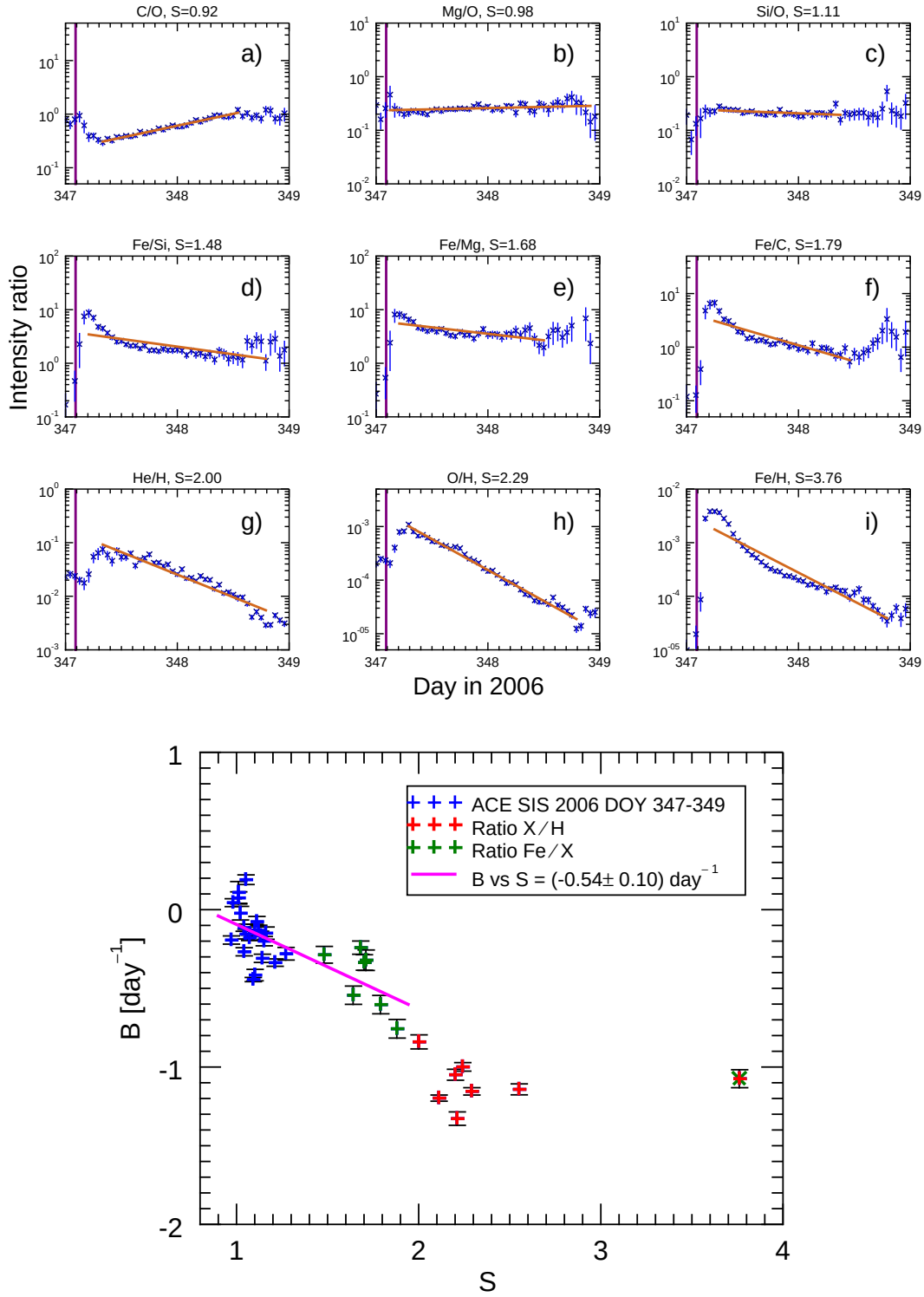

Figure 5.4: Top panels: A succession of SEP ratios with ascending S values (see Table 5.2) for event #2. Proton intensities were measured by SOHO/ERNE and heavy ion intensities by ACE/SIS. Energy channels for a pair of ions in each ratio are given in Table 5.3. The SEP ratio data (blue) in time interval between the maximum and the minimum are overplotted with the fitted function (brown). All intervals on the vertical axes are scaled equally to 3 orders of magnitude. Bottom panel: Time constant values B plotted as a function of S. The monotonic dependence as in event #24 is observed but without the discontinuity.

iron, is affected by the passing shock, which could contribute to the event having two episodes. The SEP event occurred while the particle intensity was elevated from a preceding event, see O intensity in Figure 5.3, which probably contributed to the observed increase of the Fe/O ratio after the start of the flare. The pre–event background for heavy ions is less significant than for protons because heavy ion events decay faster, and the O and Fe intensities increased by 2 orders of magnitude over the background. The Fe/O ratio, bottom graph in Figure 5.3, decreases for $\Delta t_{\mathrm{Fe/O}} = 1.25\,\mathrm{days}$. Fe/O decays to a value of about 2×10^{-1}, higher than the value reached in event #24. This event is Fe–rich with average Fe/O value $A_{avg}(\mathrm{Fe/O}) = 0.540$.

The top panels (a)–(i) in Figure 5.4 show a subset of heavy ion ratios as in in Figure 5.2. The plotted ratios show similar temporal evolution as was observed in event #24, except for the initial increases observed in most heavy ion ratio time profiles, which may be the result of the elevated background from the preceding event.

The quantitative analysis was applied to the SEP ratios as in event #24 and the values of B vs S plotted as shown in the bottom panel in Figure 5.4. For this event, the B versus S dependence in the interval $S \in [0.9, 2.0)$ has the slope value $-0.54 \pm 0.10\,\mathrm{day}^{-1}$. The dependence shows a monotonic behaviour but in this case the discontinuity at $S = 2.0$ is not present. Instead, the X/H ratios decay at faster rate than other heavy ion ratios. This behaviour is observed during elevated particle background because the proton intensities at $\sim 10 - 15$ MeV/nucleon only change $\approx$1 order of magnitude over the 2–day period.

5.3.3 Event #38 (2013 DOY 311–314)

The SEP observations of event #38 at the two STEREO spacecraft were discussed in Section 4.1.2. Here, the time dependence of Fe/O ratio and the B versus S dependence are shown for STEREO A in Figure 5.5 and for STEREO B in Figure 5.6.

As can be seen in the top graphs in Figure 5.5 and Figure 5.6, STEREO A,

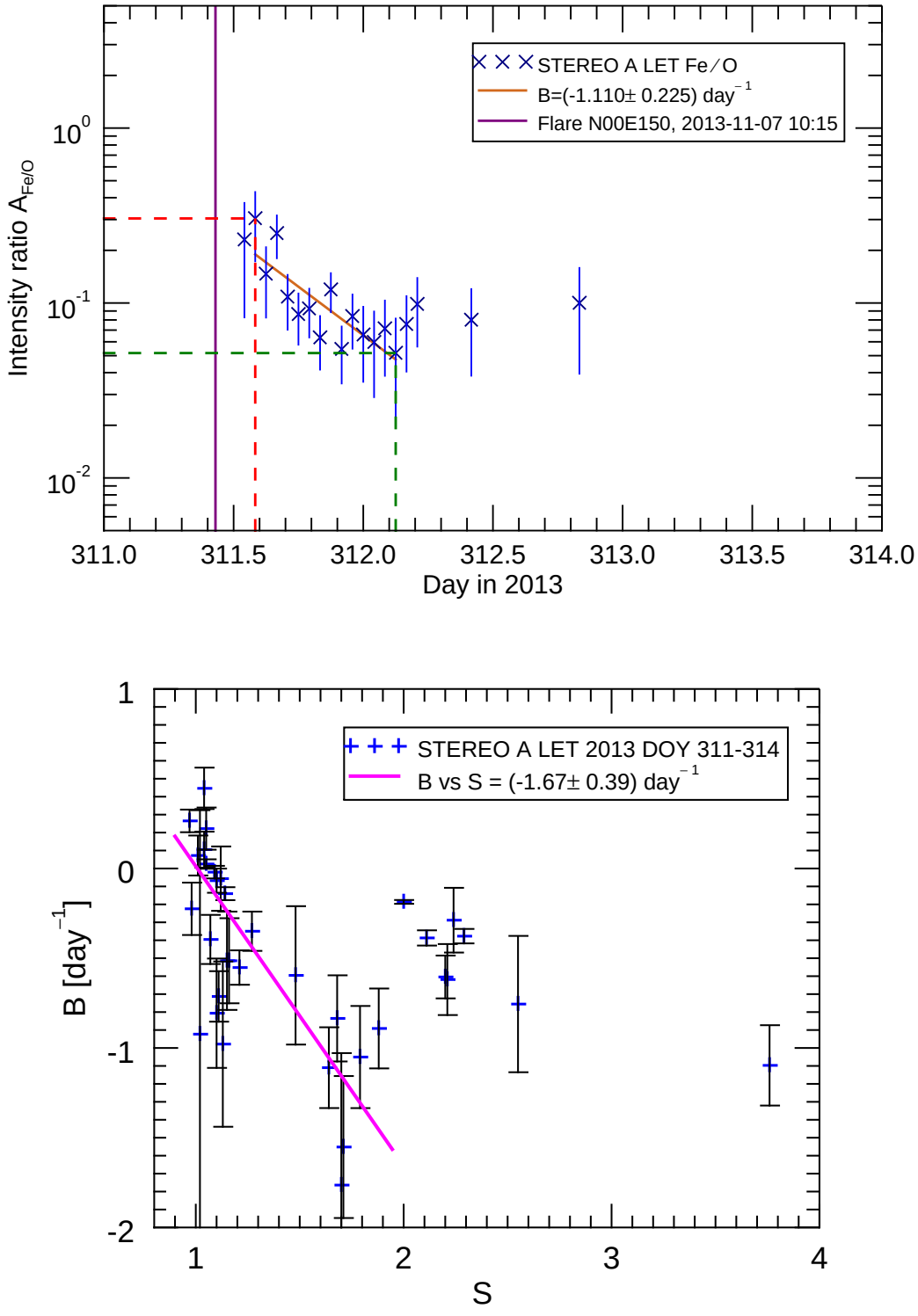

Figure 5.5: Event #38 measured by STEREO A/LET at 4.0–4.5 MeV/nucleon. Top graph: Fe/O intensity ratio (blue) are overplotted with the fitted exponential function (brown), where B is the time constant for changes in ion ratio. The line of best fit was fitted to the data in the period Δt, indicated by the dashed lines of the maximum (red) and minimum (green) data point. The vertical purple line denotes the start time of the flare. Bottom graph: B vs S dependence. The B values (blue) are overplotted with the best slope fit (magenta) in $S \in [0.9, 2.0)$.

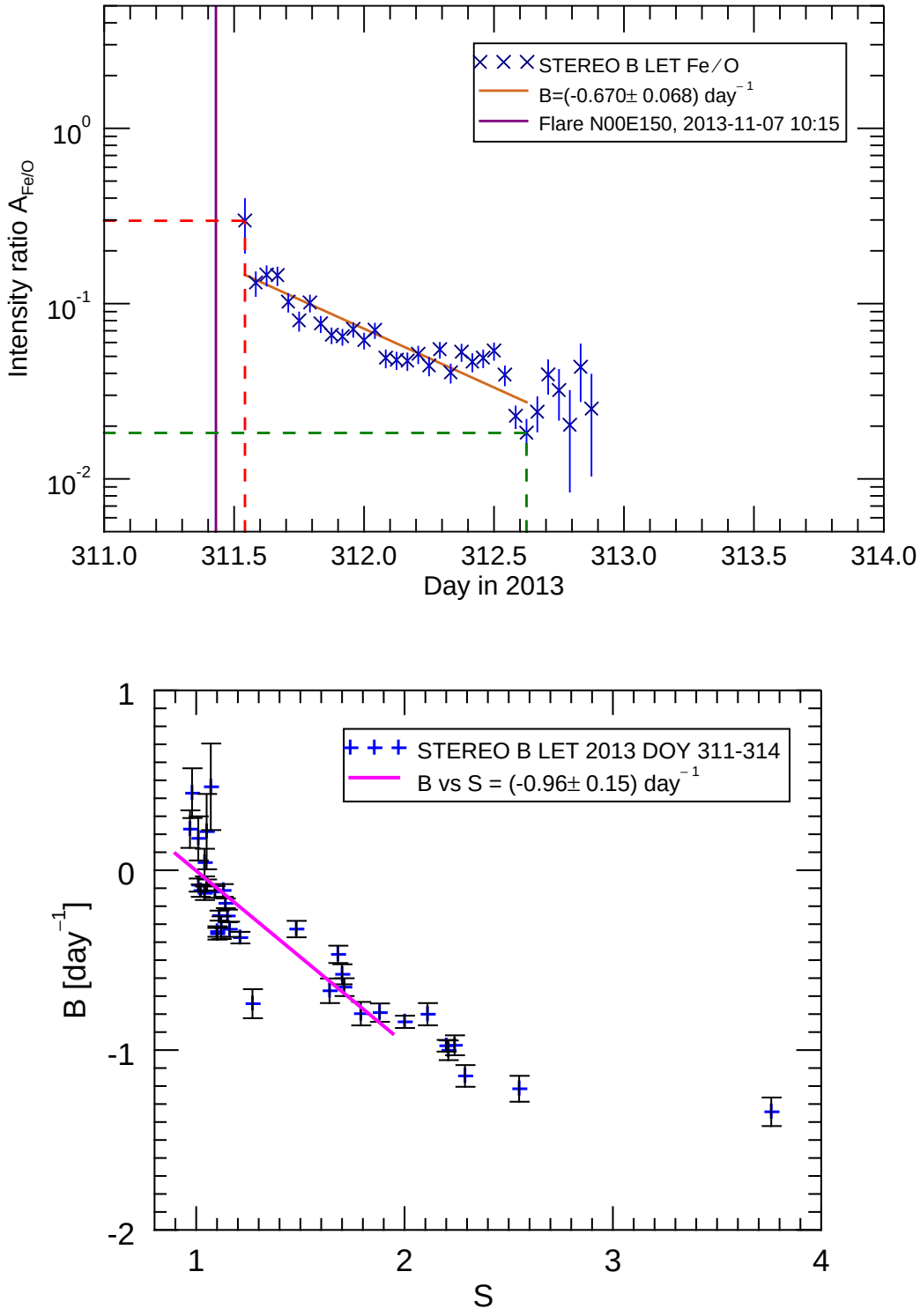

Figure 5.6: Event #38 measured by STEREO B/LET at 4.0–4.5 MeV/nucleon. Top graph: Fe/O intensity ratio (blue) are overplotted with the fitted exponential function (brown), where B is the time constant for changes in ion ratio. The line of best fit was fitted to the data in the period Δt, indicated by the dashed lines of the maximum (red) and minimum (green) data point. The vertical purple line denotes the start time of the flare. Bottom graph: B vs S dependence. The B values (blue) are overplotted with the best slope fit (magenta) in $S \in [0.9, 2.0)$.

which is the better magnetically connected spacecraft ($\Delta\phi_{\mathrm{STA}} = 13\,^{\circ}$), observed a steeper Fe/O decrease that lasted for a shorter time, compared to STEREO B ($\Delta\phi_{\mathrm{STB}} = -50\,^{\circ}$).

The B versus S dependence at STEREO A, shown in the bottom panel in Figure 5.5 shows a steeper dependence that that of STEREO B shown in Figure 5.6. Not only is the slope value steeper for STEREO A (-1.67 ± 0.39 day^{-1}) versus STEREO B (-0.96 ± 0.15 day^{-1}), but the discontinuity is observed in the STEREO A data that is not observed at STEREO B. Larger error bars in the STEREO A dependence correspond to fewer data points being fitted.

It appears that whether the discontinuity is observed or not may depend on the magnetic connection of the observer.

5.3.4 Event #42 (2014 DOY 55–65)

The SEP observations of event #42 by all three spacecraft were discussed in Section 4.1.1. The SEP event at STEREO B lasted only 4 days, therefore the analysed period here will be 2014 DOY 56–60. The Fe and O intensities, and the Fe/O ratio time profile are shown in Figure 5.7. The Fe/O time profile shows over the first 3 days, $B = -0.012 \pm 0.018$ day^{-1}, followed by an increase that is associated with limited count statistics. However, a steep decrease can be observed in the first $\sim$12 hours, $B = -2.50 \pm 0.41$ day^{-1}.

The heavy ion ratios over the 4–day period and the corresponding B versus S plot are shown in Figure 5.8.

The quantitative analysis was applied to the heavy ion ratios in event #42 in two ways: first the fitting procedure was applied to the entire event (i.e. over a time range $\Delta t = 4$ days), second it was applied only to the first 12 hours after the start of the flare. The first 12 hours are when a fast decrease (increase) occurs in some ratios. The graphs of B vs S dependence for the two Δt values are shown in Figure 5.9. The B vs S graph for $\Delta t = 4$ days, the top graph in Figure 5.9, shows that the time constant values B are smaller because the initial decrease in Fe/X ratios is

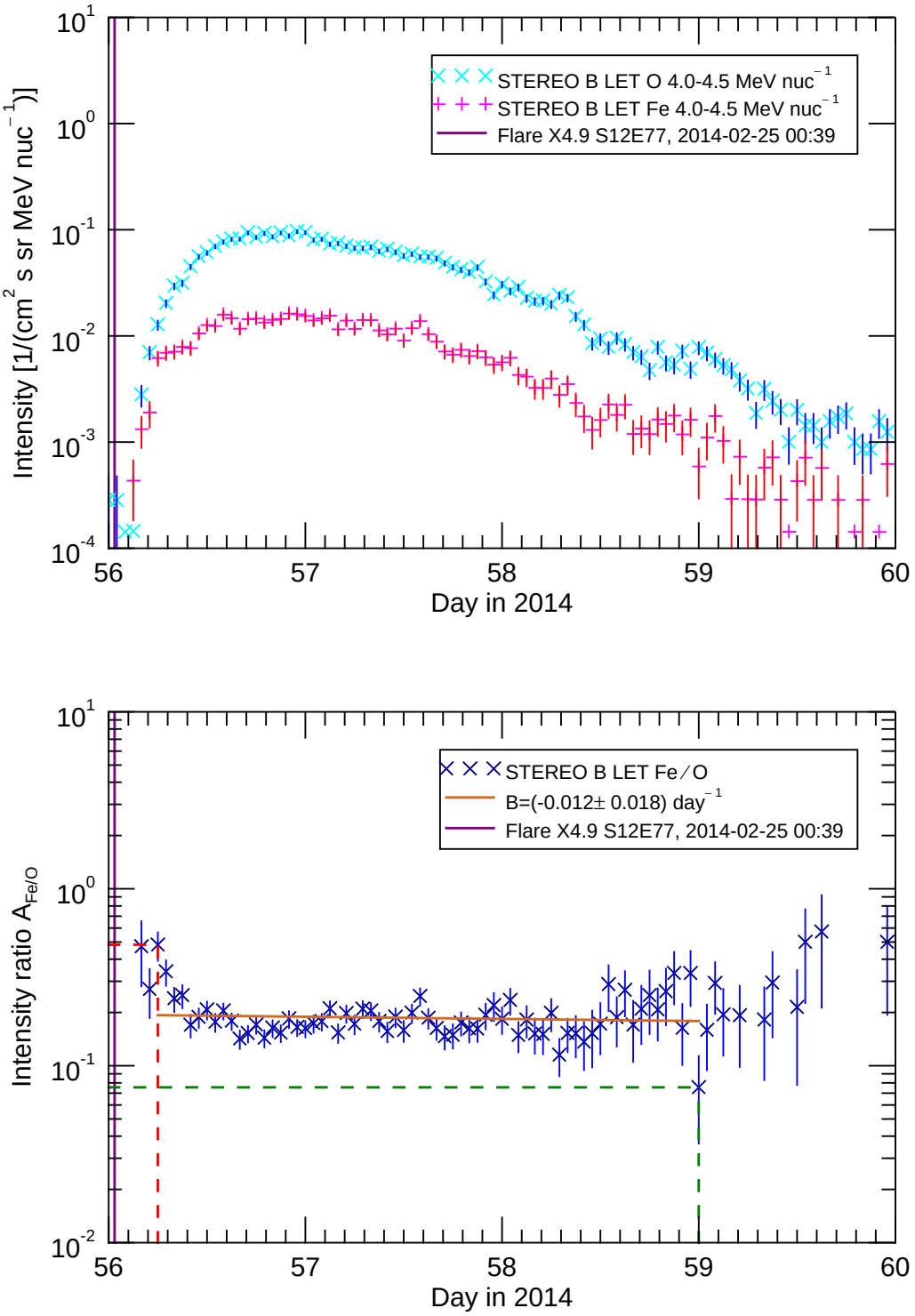

Figure 5.7: Top graph: Fe (magenta) and O (cyan) intensity for event #42 measured at 4.0–4.5 MeV/nucleon by STEREO B/LET. Bottom graph: Fe/O intensity ratio. The SEP ratio data (blue) are overplotted with the fitted exponential function (brown) given by Equation 5.2, where B is the time constant for changes in ion ratio. The line of best fit was fitted to the data in the period Δt, indicated by the dashed lines of the maximum (red) and minimum (green) data point. The vertical purple line denotes the start time of the flare.

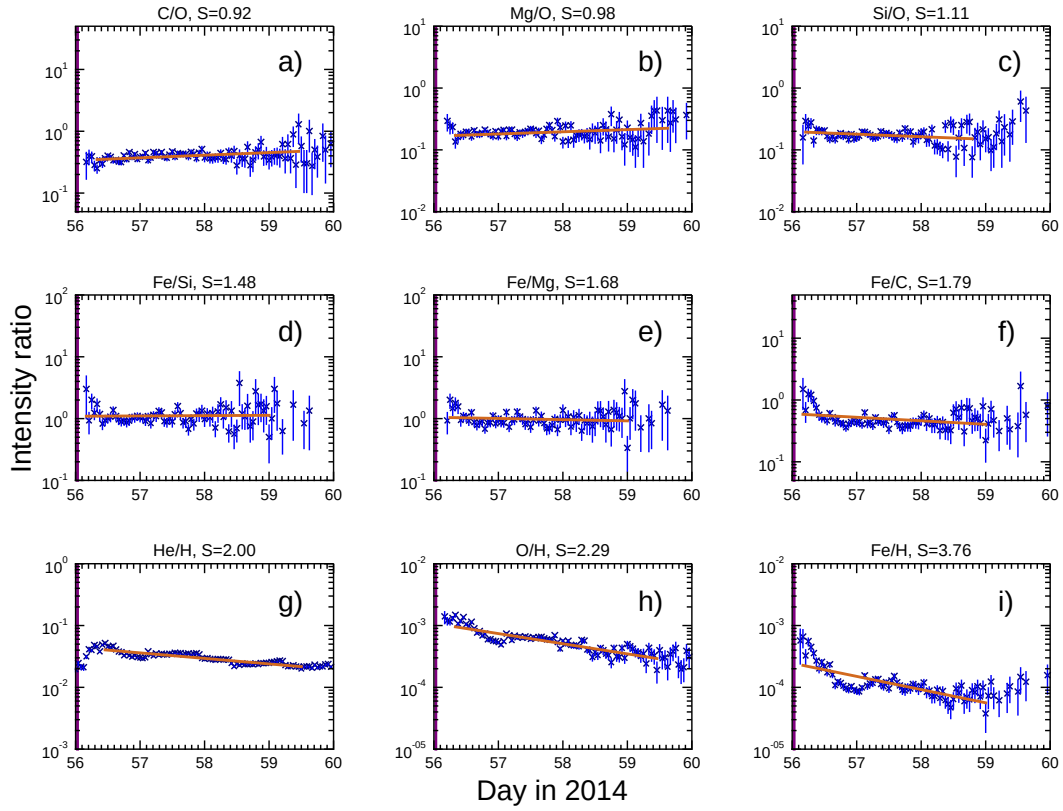

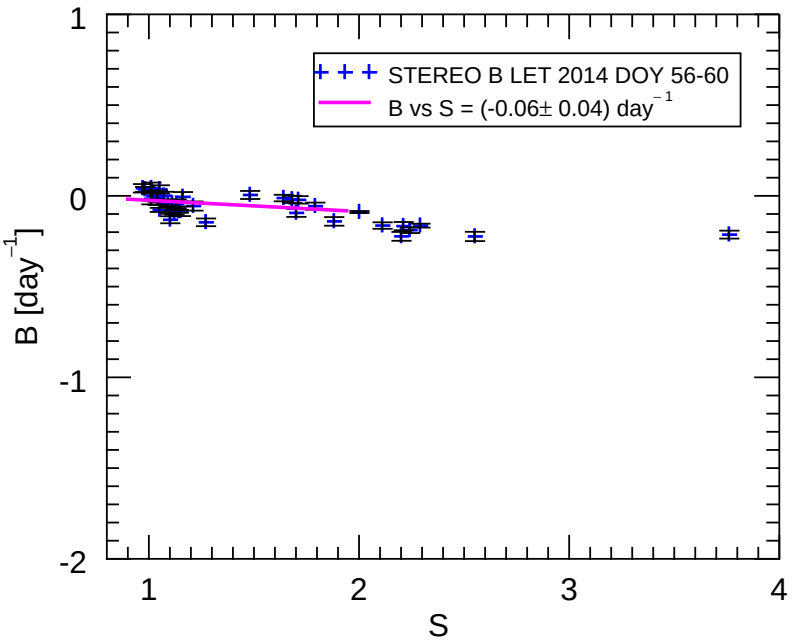

Figure 5.8: Top panels: A succession of SEP ratios with ascending S values (see Table 5.2) for event #42. The SEP ion intensities were measured by STEREO B/LET at 4.0–4.5 MeV/nucleon. The SEP ratio data (blue) in time interval between the maximum and the minimum are overplotted with the fitted function (brown). All intervals on the vertical axes are scaled equally to 3 orders of magnitude. Bottom panel: Time constant values B plotted as a function of S. The monotonic dependence shows that more decrease is observed in ratios with increasing S.

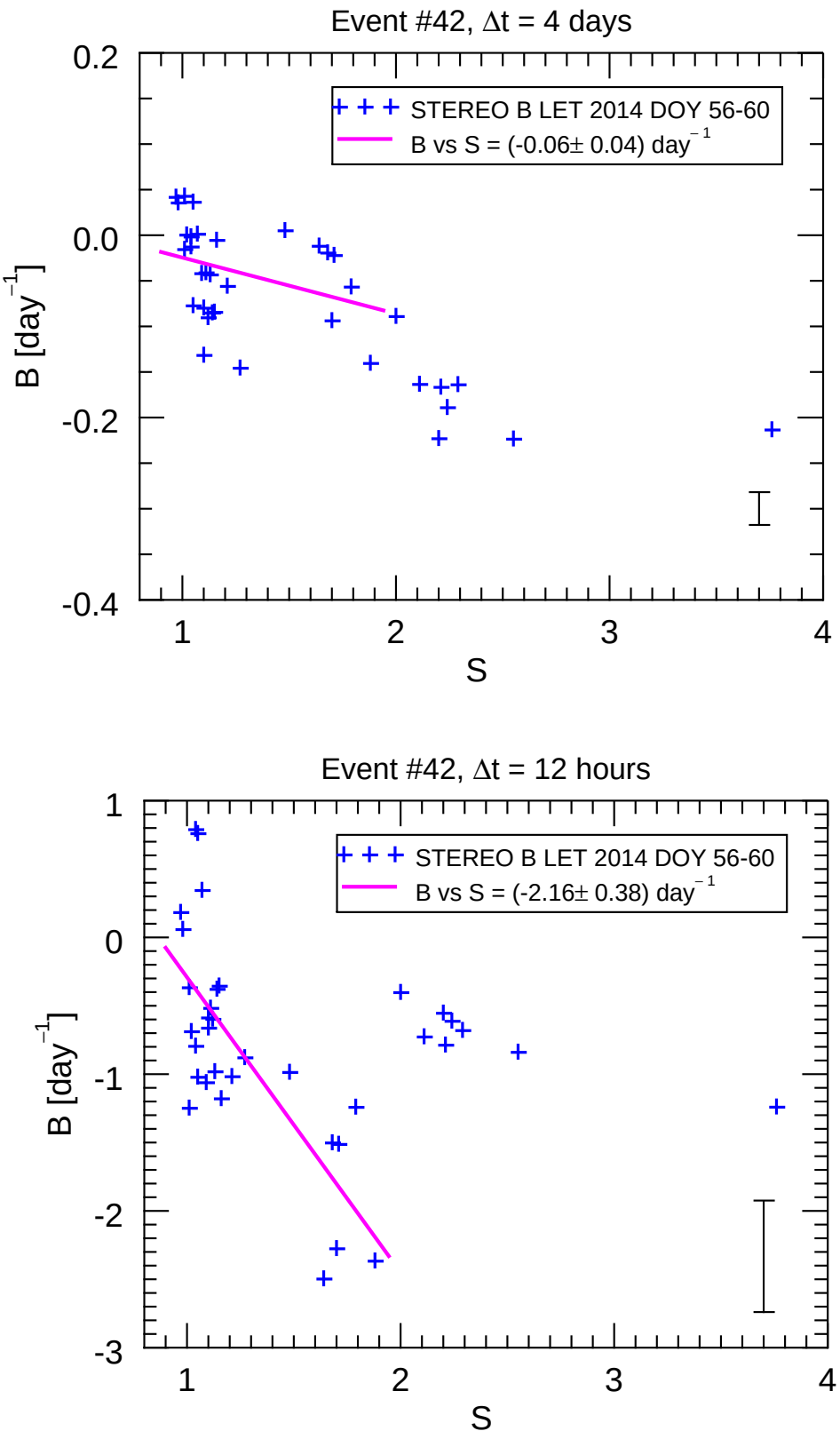

Figure 5.9: B vs S dependence for event #42 over $\Delta t = 4$ days and 12 hours. The B values (blue) are overplotted with the fitted function (magenta) in $S \in [0.9, 2.0)$. Note the different range of the ordinates.

averaged over a longer period, over which the ratios remain relatively unchanged. As can be seen in the bottom graph in Figure 5.9, when the fit is carried out over 12 hours, the obtained B values are larger in magnitude than in the previous events. In the bottom graph, a discontinuity at $S = 2.0$ can observed, as in Figure 5.4 and Figure 5.6, however, that is not observed in the top plot over $\Delta t = 4$ days.

5.4 Summary of the results

Table 5.4 contains the details of solar events and the parameters of SEP events, where the Fe/O decrease was observed and quantified. Further, the table also contains the details about the M/Q–dependence of heavy ion ratio time profiles. The structure of the table and the parameters of solar events follow the pattern as in Table 4.1. All CMEs associated with these SEP events are halo CMEs with dA=360° (CDAW CME Catalog 2017). Additionally, the results of quantitative analysis are quoted for the time dependence of heavy ion ratios, where B is the derived exponential time constant for Fe/O. "Slope" denotes the best fit line to the B versus S dependence in interval $S \in [0.9, 2.0)$, and whether discontinuity was observed. Note that all quoted parameters for STEREO data refer to the energy bin at 4.0–4.5 MeV/nucleon.

Fe/O decreases were quantified for 20 events, which include event #38 observed by STEREO A and B, and event #42 observed by ACE and STEREO B. Event #42 at STEREO B was analysed over 2 intervals of $\Delta t = 4$ days and 12 hours. Typical values of the Fe/O decrease are between $S \approx -0.2$ and -1.2 day^{-1}. Extreme cases consist of the observations in event #42, where very little time variation in Fe/O was observed over the 4–day period, $S = -0.01$ day^{-1}, but very steep decrease was observed over $\Delta t = 12$ hours, $S = -2.5$ day^{-1}.

The M/Q dependence of the time profiles was quantified in 14 events, where the discontinuity in the B versus S dependence was observed in 10 cases. Typical values of the slope in the interval $S \in [0.9, 2.0)$ are between ≈ -0.5 and -1.55 day^{-1}. Again, the extreme cases are the ones in event #42 observed by STEREO B, with the slope

Table 5.4: Details of solar eruptive events and SEP events with Fe/O decrease. For each flare the day, start time (including fractional day of year (DOY)), peak time (if known), flare class and location are recorded. For CMEs, the time indicates when a CME was first observed by the LASCO instrument, v_{CME} is the linear speed in the plane of sky in km/s, MPA is the measured position angle of the fastest moving element of the CME leading edge in degrees. v_{sw} is the solar wind speed at the spacecraft (s/c) at the start of an SEP event in km/s, $\Delta\phi$ is longitudinal separation in degrees (positive is flare west of the spacecraft footpoint), $\Delta\theta$ is latitudinal separation in degrees (positive is flare north of the spacecraft). $A_{\mathrm{Fe/O}}$ is mean Fe/O value, A_2/A_1 is the ratio of Fe/O values (final/initial), Δt the time over which the Fe/O decrease occurs, B is the derived exponential time constant for changes in ion ratio. Slope denotes the best fit line to the B vs S dependence in interval $S \in [0.9, 2.0)$, and whether discontinuity was observed.

Event		Flare						CME			Spacecraft				Fe/O event				B vs S	
#	Year	Day	Start time	(DOY)	Peak	Class	Location	Time	v_{CME}	MPA	s/c	v_{sw}	$\Delta\phi$	$\Delta\theta$	$A_{\mathrm{Fe/O}}$	A_2/A_1	Δt	B	Slope	Discont.
2	2006	Dec 13	02:14	(347.09)	02:40	X3.4	S06W23	02:54	1774	193	ACE	645	–17	–6	0.519	0.120	1.25	-0.54 ± 0.06	-0.54 ± 0.10	N
4	2011	Mar 21	02:10	(80.09)	—	—	N17W130[a]	02:24	1341	274	ACE	364	60	24	0.376	0.055	1.00	-0.77 ± 0.11	—	—
7	2011	Aug 04	03:41	(216.15)	03:57	M9.3	N19W36	04:12	1315	298	ACE	352	–36	13	0.165	0.097	2.00	-0.34 ± 0.02	-0.55 ± 0.05	Y
8	2011	Aug 09	07:48	(221.33)	08:05	X6.9	N17W69	08:12	1610	279	ACE	623	28	11	0.370	0.164	0.50	-1.01 ± 0.26	—	—
12	2012	Jan 23	03:38	(23.15)	03:59	M8.7	N28W21	04:00	2175	326	ACE	450	–36	33	0.014	0.023	1.13	-0.74 ± 0.20	—	—
16	2012	Mar 13	17:12	(73.72)	17:41	M7.9	N17W66	17:36	1884	286	ACE	568	21	24	0.104	0.108	1.17	-0.44 ± 0.11	-1.51 ± 0.28	Y
17	2012	May 17	01:25	(138.06)	01:47	M5.1	N11W76	01:48	1582	261	ACE	363	6	14	0.195	0.020	1.25	-0.50 ± 0.11	-0.57 ± 0.25	Y
22	2012	Jul 19	04:17	(201.18)	05:58	M7.7	S13W88[a]	05:24	1631	275	ACE	411	26	–18	0.245	0.131	1.63	-0.19 ± 0.06	-0.68 ± 0.54	Y
24	2012	Aug 31	19:45	(244.82)	20:43	C8.4	S16E42	20:00	1442	90	STB	323	–5	–12	0.064	0.030	1.25	-0.92 ± 0.06	-1.33 ± 0.04	Y
27	2013	Mar 05	03:26	(64.14)	—	—	N11E146[a]	03:48	1316	137	STA	345	9	6	0.068	0.097	1.42	-0.41 ± 0.04	-0.49 ± 0.06	Y
31	2013	May 22	13:08	(142.55)	13:32	M5.0	N16W68[a]	13:25	1466	287	ACE	446	11	18	0.082	0.046	1.04	-1.14 ± 0.11	-1.55 ± 0.17	Y
33	2013	Sep 29	21:43	(272.90)	22:39	C1.3	N17W29	22:12	1179	343	ACE	266	–67	10	0.188	0.065	1.25	-0.61 ± 0.09	-0.72 ± 0.10	N
38[A]	2013	Nov 07	10:15	(311.43)	—	—	N00E150[a]	10:36	1405	89	STA	530	13	6	0.112	0.170	0.54	-1.11 ± 0.23	-1.67 ± 0.39	Y
38[B]	2013	Nov 07	10:15	(311.43)	—	—	N00E150[a]	10:36	1405	89	STB	582	–50	0	0.067	0.062	1.08	-0.67 ± 0.07	-0.96 ± 0.15	N
40	2014	Jan 06	07:30	(6.31)	07:45	X3.5[b]	S15W110[b]	08:00	1402	274	ACE	379	43	–11	0.708	0.077	1.21	-0.48 ± 0.07	—	—
41	2014	Jan 07	18:04	(7.75)	18:32	X1.2	S12W08	18:24	1830	231	ACE	392	–57	–5	0.091	0.026	1.79	-0.54 ± 0.06	—	—
42[S]	2014	Feb 25	00:39	(56.03)	00:49	X4.9	S12E77	01:25	2147	73	ACE	460	–132	–5	0.270	0.078	3.21	-0.27 ± 0.01	—	—
42[4d]	2014	Feb 25	00:39	(56.03)	00:49	X4.9	S12E77	01:25	2147	73	STB	571	38	–19	0.212	0.156	2.75	-0.01 ± 0.02	-0.06 ± 0.04	N
42[12h]	2014	Feb 25	00:39	(56.03)	00:49	X4.9	S12E77	01:25	2147	73	STB	571	38	–19	0.302	0.352	0.50	-2.50 ± 0.41	-2.16 ± 0.38	Y
43	2014	Apr 02	13:18	(92.55)	14:05	M6.5	N11E53	13:36	1471	60	STB	352	38	5	0.195	0.262	0.54	-0.91 ± 0.12	—	—
45	2014	Sep 01	11:00	(244.46)	—	X2.1[b]	N14E129[a,c]	11:12	1901	65	STB	441	–26	21	0.089	0.027	1.25	-1.10 ± 0.10	-1.48 ± 0.10	Y

[a] The position of the backside flare was calculated using STEREO FITS files.
[b] The flare class for this event was estimated by Pesce–Rollins et al. (2015).
[c] The position of the flare was identified at N14E127 in the CDAW CME Catalog.
[A] SEP event observed by STEREO A/LET.
[B] SEP event observed by STEREO B/LET.
[S] SEP event observed by ACE/SIS.
[4d] SEP event observed by STEREO B/LET analysed for $\Delta t = 4$ days.
[12h] SEP event observed by STEREO B/LET analysed for $\Delta t = 12$ hours.

Note: All CMEs associated with these SEP events are halo CMEs with dA=360 ° (cf. Table 4.1).

values of -0.06 day^{-1} over the 4–day period, and -2.16 day^{-1} over $\Delta t = 12$ hours.

5.5 Discussion

In this chapter, we have studied SEP intensities and time dependence of elemental ratios in 20 SEP events, where Fe/O has been observed to decrease over time, in the $\approx 4 - 15$ MeV/nucleon energy range. We used 1–hour averaged SEP data from energetic particle telescopes onboard ACE, SOHO, STEREO A and B, and systematically quantified the temporal dependence of abundant SEP ratios. The list of SEP events is given in Table 5.4.

We observed that time evolution of heavy ion ratios is a common feature present in the analysed SEP events, with largest variation in Fe/X ratios, where X indicates an abundant SEP element. We found that some abundance ratios, e.g. Mg/O, remained relatively unchanged during an SEP event and some ratios, e.g. Ne/O, even showed an increase over time. This behaviour is ordered by the S value of an SEP ratio, defined as the ratio of M/Q values of the two SEP species in the ratio. Ratios with $S < 1$ ($S > 1$) exhibit an increase (decrease) over time. We also observed that the slope of a ratio tends to be steeper for ratios with larger S value. Therefore, the temporal evolution of SEP heavy ion ratios shows ordering by M/Q.

We quantitatively examined the heavy ion pairs listed in Table 5.2 for 13 SEP events, and for each pair we fitted the time profile of the corresponding intensity ratio, and derived values of the time constant for changes in ion ratio B. For each event we plotted B as a function of S, obtaining plots such as those in Figure 5.2, 5.4, 5.5, 5.6, 5.8, and 5.9. In all events a monotonic dependence of B vs S in the range $S \in [0.9, 2.0)$ is obtained. In 10 out of 14 cases, the B vs S dependence shows a discontinuity at $S = 2.0$, which corresponds to He/H (see e.g. the bottom panel in Figure 5.9). In events #2, #33, and #38 observed by STEREO B, the discontinuity at $S = 2.0$ is not present, probably because the proton intensities, only vary by $\sim$1 order of magnitude during the analysed period and do not decay significantly, and

the X/H ratios decay at higher rate than in the other events. The discontinuity was not observed in event #42, the top graph in Figure 5.9, where $\Delta t = 4$ days was much longer that the period of significant temporal variation, i.e. the first $\sim$12 hours after the start of the flare. The B values obtained by fitting in the two time intervals $\Delta t = 4$ days and $\sim$12 hours in event #42 both showed ordering by M/Q. In event #38 the discontinuity was observed at STEREO A, a well connected spacecraft, and not at STEREO B, for which the event was eastern. It is possible that whether the discontinuity is observed or not might depend on the magnetic connection of the observer.

When plotted in logarithmic–linear plot, intensity ratio time data often exhibit time profiles similar to a linear function between their maximum and minimum values. Every SEP ratio had a minimum and a maximum identified independently. The method of finding the maximum and the minimum of a ratio time profile affected the value of the fitted time constant B, where ratios fitted over a longer time interval showed less average temporal variation, e.g. most of the Fe/X ratios in event #42. This is clearly a limitation of the used method, nevertheless, it allowed us to characterise and quantify the observed temporal evolution in SEP ratio time profiles.

Some events have more complex structure than the monotonic intensity decrease shown for example by event #24. More complicated intensity profiles, from which the ratio profiles are derived, can be caused by interplanetary structures affecting the propagation of ions, multiple events or shocks. This makes the choice of the fit interval Δt more challenging and different ionic ratios might require different Δt values in a single event.

The temporal evolution of heavy ion ratios has previously been interpreted as a signature of a rigidity–dependent acceleration (Tylka et al. 1999). In this model, the decrease in the Fe/O ratio would be caused by Fe ions with large M/Q spending less time at the shock during acceleration and being released earlier than O ions.

However, Mason et al. (2006) presented data on Fe and O intensity profiles at two energy ranges, where they showed that the decrease of Fe/O over time is likely

a result of SEP propagation through the interplanetary medium, in common with other authors (e.g. Scholer et al. 1978; Mason et al. 2012; Tylka et al. 2013). In 1D propagation, the scattering mean free path λ is assumed to depend on M/Q of an SEP ion, e.g. $\lambda_{\mathrm{Fe}} > \lambda_{\mathrm{O}}$. The stronger scattering causes a slower propagation of an ion with lower M/Q values to the observer, which can result in temporal dependence of a ratio profile such as ratios observed in this study.

In a recent study, Dalla et al. (2017b) carried out 3D full–orbit test particle simulations of SEP propagation in a unipolar Parker spiral magnetic field. Fe and O ions injected near the Sun were allowed to propagate in 3D with a rigidity independent scattering mean free path $\lambda = 1$ AU. Their crossings of the 1 AU sphere were counted as a function of time for observers at various locations with respect to the source. The particles experience strong curvature and gradient drifts (Dalla et al. 2013) which cause transport in a direction perpendicular to the magnetic field, with drift velocities proportional to M/Q. For particles at equal energy/nucleon, the ion with larger M/Q propagates across the magnetic field more easily and is able to reach the detector at earlier time. The calculated Fe/O time profiles from the simulations are qualitatively similar to the observations in event #24. Therefore drift as an SEP transport mechanism in 3D could explain the observed temporal variation of heavy ion ratios. In this model, the simulation with the value of mean free path $\lambda = 0.1$ AU produced similar results as in the case with $\lambda = 1$ AU. Comparing the results corresponding to the two values of λ, the variation of the mean free path had little effect on the final Fe/O ratio time profiles.

Several ionic ratios in our figures show an increase towards the end of the SEP event, e.g. Fe/O in Figure 5.1 and Fe/Si, Fe/C and Fe/H in Figure 5.2. This kind of behaviour can also be seen in Figure 5 in Tylka et al. (2013), Figure 2 in Zelina et al. (2015) and Figure 3 in Reames (1990). Such an effect could be in some cases a result of low count statistics, however, for some events it does appear to be a real effect, e.g. events #24 and #42 (Figure 5.1 and Figure 5.7). Simulations by Dalla et al. (2017b) show a similar behaviour in the Fe/O time profiles. In that model the

increase late in the event results from O decaying at a faster rate than Fe since O occupied a narrower longitudinal extent than Fe, due to a smaller drift. The increases could be caused by passing magnetic structures, e.g. shocks and ICMEs, within which the particle populations, magnetic field vectors and transport conditions may be different from the surrounding environment. In event #2, after passing of the shock on 14 December 2006 (DOY 348.59) (Figure 5.3), the O intensity suddenly starts decreasing at a faster rate than Fe, and the Fe/O value increases as the result.

In an analysis of time profiles of heavy ion ratios, Mason et al. (2012) used a propagation model and predicted decreases of He/H, but observed that He/H decreased only in some of the SEP events. Mason et al. (2012) identified the behaviour of protons as anomalous and similar behaviour was observed in SEP events reported by Reames (1990) and Reames et al. (2000). In our analysis, we found that the time profiles of X/H ratios were anomalous compared to other ratios, often showing an increase of the ratio values before the decrease. The decreases of X/H ratios in time that occurred at lower rate compared with other heavy ion ratios resulted in a discontinuity observed in B versus S plots.

Anomalous time profiles of X/H ratios can emerge in a number of scenarios. The ratios could be signatures of differences in SEP acceleration or interplanetary transport between protons and heavier ions. Mason et al. (2012) concluded that the temporal behaviour of protons was different from heavy ion elements. On the other hand, they could be a result of the much higher abundance of protons in the SEP population. At present, the origin of the anomalous nature of X/H time profiles and their slower decay over time remains unknown, and any theory should be able to explain temporal evolution of heavy ion as well as X/H ratios.

The B vs S profiles depend on our assumption of used charge state values. Obtaining values of SEP charge states is challenging and this type of measurement is not routinely carried out for all SEP events. In our analysis, we used charge state values averaged over a number of events by Luhn et al. (1985) that have been used previously in similar studies. While these measurements should be representative of

typical ionic charge state values, charge states of an SEP ion are known to have different values in separate particle events (e.g. $Q_{\mathrm{Fe}} \approx 10 - 20$) and can depend on the kinetic energy (Klecker et al. 2006b). If event–specific values of Q were used, S–values in Table 5.2 would be modified and this would result in a shift of the data points horizontally in the B versus S plots.

The Fe/O ratio in event #42 has a time profile with double power law characteristics, where the observed Fe/O ratio value decreases for a short period, followed by the period with very little variation until the end of the event. It is possible that this behaviour could be a result of an Fe SEP population, where the average charge state of the arriving Fe ions varies with time. This phenomenon was demonstrated in a test particle propagation simulation by Dalla et al. (2017a), in which a distribution of Fe ions with charge states $Q_{\mathrm{Fe}} = 8-21$ was injected at the Sun. Depending on the observer's location, the observers at 1 AU that were not well magnetically connected to the source region observed the average Fe charge state to increase during event, typically from $Q_{\mathrm{Fe}} \sim 10$ to $Q_{\mathrm{Fe}} \sim 15$. Further simulations will be needed to verify the effect of considering different Fe charges on the average S value and the B vs S plots. However, the use of a particle instrument capable of measuring ionic charge states would be essential for resolving the role of different Fe charge states.

The field line meandering is not expected to produce the observed time variation of ionic ratios because it modifies the trajectories of SEP ions, for example Fe and O, equally. However, the turbulence in the solar wind might lead to the spatial diffusion of SEPs that may vary for ions with different Larmor radius.

Overall, the analysis of time evolution of ionic ratios, presented in Chapter 5, is the first quantitative study of the characteristics of ratio profiles over time, carried out over a large number of ionic pairs (as opposed to just Fe/O). While the precise mechanism causing the ordering of B with S will need to be determined in future work, our data are consistent with interplanetary transport effects being the cause of the observed ordering, whether due to 1D (Mason et al. 2012) or 3D drift (Dalla et al. 2013, 2017b) effects.

Chapter 6

Conclusions

In this thesis, I have studied and quantitatively characterised the longitudinal dependence of heavy ion SEP events and the temporal evolution of heavy ion ratios using SEP data from the ACE/SIS, SOHO/ERNE, STEREO/LET and STEREO/HET instruments. The main results are as follows:

1. There are 50 Fe SEP events discussed in this thesis that occurred between 2006 and 2016. Out of these, 12 events were observed simultaneously by multiple spacecraft, and the time dependence of Fe/O and other ionic ratios was quantified for 20 events. (See objective b) in Section 1.5.)

2. The decay over time in the profiles of Fe/O ratio is a common feature of SEP events. However, in some events the Fe/O ratio does not vary significantly over the duration of an SEP event.

3. In SEP events where the Fe/O ratio is observed to decrease, a time variation of elemental abundance ratios for other ionic pairs occurs as well. The temporal evolution of heavy ion ratios is ordered by the ratio of mass–to–charge values of the two SEP ions in the pair, S. (See objective d) in Section 1.5.)

4. Over the range $S \in [0.9, 2.0)$, considering 28 different ionic ratios, we find a clear monotonic behaviour with S, with slopes of B versus S typically given by –0.5 to –1.5 day^{-1}.

5. Ratios of heavy ion to hydrogen, X/H, where X is an abundant SEP element, corresponding to $S \geq 2.0$, often show an increase before the decrease in their time profiles and decay at slower rates. This anomaly is present in the B versus S plots as a discontinuity where the B values jump to a significantly higher value than would be predicted by the B vs S dependence for $S < 2$. The cause of the discontinuity is not presently known, but it may depend on the relative position between the spacecraft and the flare, or the averaging period.

6. In SEP events, if the proton intensities are sufficiently high, Fe SEPs can be observed in regions widely separated in longitude from the source region.

7. The event–averaged Fe/O values show a complicated dependence on longitude. Several SEP events, where a higher Fe/O value was observed at a remote observer, and Fe–rich events was observed over a broad range of longitudes, cannot be fully explained by the two–class paradigm for classification of SEP events. (See objective c) in Section 1.5.)

With the launch of the STEREO spacecraft, many SEP studies have shown observational evidence that protons and electrons can be detected simultaneously at spacecraft widely separated in longitude (e.g Dresing et al. 2014; Richardson et al. 2014; Gómez–Herrero et al. 2015). Multispacecraft observations of Fe SEPs studied in this work complement those observations.

The temporal variation of heavy ion ratios has been observed at various instances in the ecliptic (e.g. Tylka et al. 1999; Mason et al. 2012) and at high heliographic latitudes (Tylka et al. 2013). In recent years, a consensus has emerged that the time evolution of Fe/O and other ionic ratios is an interplanetary transport effect (Mason et al. 2006; Tylka et al. 2013). At the present time, both 1D rigidity–dependent scattering ($\lambda \propto (m/q)^n$, e.g. Mason et al. 2012), and 3D drift associated transport (drift velocity $\propto m/q$, Dalla et al. 2017b), are possible mechanisms that may explain our observations.

The exact mechanism that would result in Fe–rich events observed over a broad

range of longitudes, e.g. observations reported by Cohen et al. (2014), is not yet known. The higher event–averaged Fe/O values observed at the spacecraft, which had poor magnetic connection to the source region, could be a signature of:

- a suprathermal seed particle population that varies as a function of longitude, e.g. as suggested by Cohen et al. (2014);
- an acceleration mechanism that can generate SEP populations that depend on longitude over a broad range of longitudes, e.g. as suggested by Tylka et al. (2005);
- a transport mechanism that can effectively distribute SEPs to regions with poor magnetic connection, under which Fe SEPs propagate across the mean magnetic field more efficiently than O SEPs at the same energy/nucleon, e.g. the particle transport that includes drift, as suggested by Dalla et al. (2013).

To summarise, the longitudinal dependence of event–averaged Fe/O, where a higher Fe/O value is observed at a remote spacecraft, which cannot be fully explained by the two class paradigm for classification of SEP events, could also be interpreted as a signature of SEP transport mechanism that is proposed to cause the Fe/O decreases, i.e. the drift. (See objective e) in Section 1.5.)

6.1 Suggestions for future work

The SEP study contained within this thesis only covered aspects of SEP events that can be observed with the current instrumentation. In my opinion, a number of other objectives could be accomplished using the SEP data available, including those described below.

1. The heavy ion data from ACE/SIS between years 1997–2006 were not used in this work, and together with the STEREO/LET and HET data could be used

to further study and analyse properties of SEP events observed by a single spacecraft.

2. The cause of the anomalous behaviour of the temporal evolution of X/H ratios and the discontinuity in the data present at $S = 2.0$ occurred only in some events, and its cause is currently not fully understood. Further investigation of this phenomenon is desirable.

3. Doran & Dalla (2016) studied the temporal evolution of particle spectra and observed a wave–like structure in the proton spectra, propagating from high to low energies. A similar study with emphasis on the heavy ion spectra might be conducted. Similarities in the temporal evolution of protons and heavy ions could be compared and evaluated, while any differences could be used to study the X/H ratio problem.

4. The longitudinal and temporal dependence of heavy ion intensities, can in principle be extracted from any SEP propagation model. While the study of Dalla et al. (2017b) focussed on the Fe/O ratio, it would be interesting to apply their model to other ratios. More generally, it might be enlightening to compare the observational results obtained in this study to the results obtained from SEP propagation models.

The research objectives could be extended if more data were obtained, as follows:

5. Ionic charge state measurements are not readily available data but historic records of SEP charge states measured by ACE/SEPICA or the SAMPEX spacecraft may exist. Future instruments may be developed that measure charge states routinely. Ideally, detection of multispacecraft events with instrumentation of larger geometric factor would provide improved data.

6. The SEP data from STEREO/LET and ACE/SIS could be combined with data from the Suprathermal Ion Telescope (SIT)[1] instrument (Mason et al.

[1] http://www.srl.caltech.edu/STEREO/docs/SIT_Level1.html

2008) onboard STEREO, and the Electron, Proton, and Alpha Monitor (EPAM)[2] (Gold et al. 1998) and ULEIS[3] (Mason et al. 1998) instruments onboard ACE. If the data were put together, the resulting energy range would span over 3 orders of magnitude. This configuration would be particularly useful to further study the energy dependence of heavy ion abundances.

7. Future spacecraft missions include the Solar Orbiter mission, which is due to be launched in 2018, and its payload will include the Energetic Particle Detector (EPD) instrument (Gómez–Herrero et al. 2017). The EPD instrument that will provide SEP measurements over a broad range of energies at radial distances closer to the Sun than ever approached before. Plans to place a particle detector on a future spacecraft mission that will orbit the Lagrangian point L5 are currently under consideration.

8. Currently, the ACE, SOHO and STEREO A spacecraft and the particle detectors onboard remain fully operational. New particle data that are being collected could be used to further study SEP events in the future studies.

[2] http://www.srl.caltech.edu/ACE/ASC/level2/epam_l2desc.html
[3] http://www.srl.caltech.edu/ACE/ASC/level2/uleis_l2desc.html

Bibliography

Agueda, N., Vainio, R., Lario, D., & Sanahuja, B. 2008, The Astrophysical Journal, 675, 1601

Alexander, D., Richardson, I. G., & Zurbuchen, T. H. 2006, Space Science Reviews, 123, 3

Anders, E. & Grevesse, N. 1989, Geochimica et Cosmochimica Acta, 53, 197

Arnaud, M. & Rothenflug, R. 1985, Astronomy & Astrophysics Supplement Series, 60, 425

Aschwanden, M. J., Caspi, A., Cohen, C. M. S., et al. 2017, The Astrophysical Journal, 836, 17

Aschwanden, M. J., Holman, G., O'Flannagain, A., et al. 2016, The Astrophysical Journal, 832, 27

Aschwanden, M. J., Xu, Y., & Jing, J. 2014, The Astrophysical Journal, 797, 50

Baker, D. N., Li, X., Pulkkinen, A., et al. 2013, Space Weather, 11, 585

Baker, D. N., Mason, G. M., Figueroa, O., et al. 1993, IEEE Transactions on Geoscience and Remote Sensing, 31, 531

Bougeret, J. L., Kaiser, M. L., Kellogg, P. J., et al. 1995, Space Science Reviews, 71, 231

Brueckner, G. E., Howard, R. A., Koomen, M. J., et al. 1995, Solar Physics, 162, 357

Cane, H. V. & Lario, D. 2006, Space Science Reviews, 123, 45

Cane, H. V., von Rosenvinge, T. T., Cohen, C. M. S., & Mewaldt, R. A. 2003, Geophysical Research Letters, 30, 8017

Carmichael, H. 1964, in Proceedings of the AAS–NASA Symposium, ed. W. N. Hess, Vol. 50 (NASA, Washington), 451

Carrington, R. C. 1859, Monthly Notices of the Royal Astronomical Society, 20, 13

CDAW CME Catalog. 2017, `http://cdaw.gsfc.nasa.gov/CME_list/`

Cecconi, B., Bonnin, X., Hoang, S., et al. 2008, Space Science Reviews, 136, 549

Cliver, E. W. 2008, in Proceedings of the International Astronomical Union, No. 257, Vol. 4, Universal Heliophysical Processes, ed. N. Gopalswamy & D. Webb (Cambridge, UK: Cambridge University Press), 401–412

Cliver, E. W., Kahler, S. W., Neidig, D. F., et al. 1995, in Proceedings of 24th International Cosmic Ray Conference, ed. N. Iucci & E. Lamanna, Vol. 4, 257

Cohen, C. M. S., Mason, G. M., Mewaldt, R. A., et al. 2008, in Proceedings of 30th International Cosmic Ray Conference, ed. R. Caballero, 95–98

Cohen, C. M. S., Mason, G. M., Mewaldt, R. A., & von Rosenvinge, T. T. 2013, in AIP Conference Proceedings, Vol. 1539, Outstanding Problems in Heliophysics: From Coronal Heating to the Edge of the Heliosphere, 151

Cohen, C. M. S., Mason, G. M., Mewaldt, R. A., & Wiedenbeck, M. E. 2014, The Astrophysical Journal, 793, 35

Dalla, S., Balogh, A., Krucker, S., et al. 2003, Geophysical Research Letters, 30, 8035

Dalla, S. & Browning, P. K. 2005, Astronomy and Astrophysics, 436, 1103

Dalla, S., Marsh, M., & Battarbee, M. 2017a, The Astrophysical Journal, 834, 167

Dalla, S., Marsh, M., Kelly, J., & Laitinen, T. 2013, Journal of Geophysical Research: Space Physics, 118, 5979

Dalla, S., Marsh, M., Zelina, P., & Laitinen, T. 2017b, Astronomy & Astrophysics, 598, A73

Dalla, S., Marsh, M. S., & Laitinen, T. 2015, The Astrophysical Journal, 808, 62

Desai, M. & Giacalone, J. 2016, Living Reviews in Solar Physics, 13, 3

Doran, D. J. & Dalla, S. 2016, Solar Physics, 291, 2071

Drake, J. F., Swisdak, M., Che, H., & Shay, M. A. 2006, Nature, 443, 553

Dresing, N., Gómez–Herrero, R., Heber, B., et al. 2014, Astronomy and Astrophysics, 567, A27

Dresing, N., Gómez–Herrero, R., Klassen, A., et al. 2012, Solar Physics, 281, 281

Dröge, W., Kartavykh, Y. Y., Klecker, B., & Kovaltsov, G. A. 2010, The Astrophysical Journal, 709, 912

Dröge, W., Kartavykh, Y. Y., Dresing, N., Heber, B., & Klassen, A. 2014, Journal of Geophysical Research: Space Physics, 119, 6074

Fisk, L. A. 1978, The Astrophysical Journal, 224, 1048

Fletcher, L., Dennis, B. R., Hudson, H. S., et al. 2011, Space Science Reviews, 159, 19

Forbush, S. E. 1937, Physical Review, 51, 1108

Forbush, S. E. 1946, Physical Review, 70, 771

Gallagher, P. T., Moon, Y., & Wang, H. 2002, Solar Physics, 209, 171

Galvin, A. B., Kistler, L. M., Popecki, M. A., et al. 2008, Space Science Reviews, 136, 437

Giacalone, J. & Jokipii, J. R. 2012, The Astrophysical Journal Letters, 751, L33

Gold, R., Krimigis, S., Hawkins, S., et al. 1998, Space Science Reviews, 86, 541

Goldston, R. & Rutherford, P. 1995, Introduction to Plasma Physics (CRC Press)

Gopalswamy, N., Yashiro, S., Michalek, G., et al. 2009, Earth, Moon, and Planets, 104, 295

Gopalswamy, N., Yashiro, S., Thakur, N., et al. 2016, The Astrophysical Journal, 833, 216

Gosling, J. T. 1993, Journal of Geophysical Research, 98, 18937

Gosling, J. T., Hildner, E., MacQueen, R. M., et al. 1974, Journal of Geophysical Research, 79, 2156

Grady, K. J. & Neukirch, T. 2009, Astronomy and Astrophysics, 508, 1461

Guo, F. & Giacalone, J. 2012, The Astrophysical Journal, 753, 28

Gómez–Herrero, R., Dresing, N., Klassen, A., et al. 2015, The Astrophysical Journal, 799, 55

Gómez–Herrero, R., Rodríguez–Pacheco, J., Wimmer–Schweingruber, R. F., et al. 2017, ArXiv: 1701.04057

Hirayama, T. 1974, Solar Physics, 34, 323

Hodgson, R. 1859, Monthly Notices of the Royal Astronomical Society, 20, 15

Hovestadt, D., Gloeckler, G., Fan, C. Y., et al. 1978, IEEE Transactions on Geoscience Electronics, 16, 166

Hudson, H. S. 2011, Space Science Reviews, 158, 5

Hudson, H. S., Bougeret, J.–L., & Burkepile, J. 2006, Space Science Reviews, 123, 13

Ilgner, C. J. 2012, in Handbook of Particle Detection and Imaging, ed. C. Grupen & I. Buvat (Berlin, Heidelberg: Springer Berlin Heidelberg), 519–533

Jokipii, J. R. 1982, The Astrophysical Journal, 255, 716

Jokipii, J. R. & Parker, E. N. 1968, Physical Review Letters, 21, 44

Kahler, S. 1994, The Astrophysical Journal, 428, 837

Kallenrode, M. 2004, Space Physics: An Introduction to Plasmas and Particles in the Heliosphere and Magnetospheres, 3rd edn., Advanced Texts in Physics (Springer)

Kallenrode, M.-B. 1993, Journal of Geophysical Research: Space Physics, 98, 5573

Kallenrode, M.-B. 2003, Journal of Physics G: Nuclear and Particle Physics, 29, 965

Kelly, J., Dalla, S., & Laitinen, T. 2012, The Astrophysical Journal, 750, 47

Klecker, B., Kunow, H., Cane, H. V., et al. 2006a, Space Science Reviews, 123, 217

Klecker, B., Möbius, E., & Popecki, M. 2006b, Space Science Reviews, 124, 289

Kontar, E. P., Bian, N. H., Emslie, A. G., & Vilmer, N. 2014, The Astrophysical Journal, 780, 176

Kontar, E. P., Hannah, I. G., & Bian, N. H. 2011, The Astrophysical Journal Letters, 730, L22

Kopp, R. A. & Pneuman, G. W. 1976, Solar Physics, 50, 85

Kosugi, T., Matsuzaki, K., Sakao, T., et al. 2007, Solar Physics, 243, 3

Kouloumvakos, A., Patsourakos, S., Nindos, A., et al. 2016, The Astrophysical Journal, 821, 31

Kwon, R.-Y., Zhang, J., & Vourlidas, A. 2015, The Astrophysical Journal Letters, 799, L29

Kóta, J. 2000, Journal of Geophysical Research, 105, 2403

Kóta, J., Manchester, W. B., Jokipii, J. R., de Zeeuw, D. L., & Gombosi, T. I. 2005, in AIP Conference Proceedings, Vol. 781, 4th Annual IGPP International Astrophysics Conference, 201–206

Labrador, A. W., Leske, R. A., Mewaldt, R. A., et al. 2001, in Proceedings of 27th International Cosmic Ray Conference, 3149–3152

Laitinen, T., Dalla, S., & Marsh, M. S. 2013, The Astrophysical Journal Letters, 773, L29

Lange, I. & Forbush, S. E. 1942, Terrestrial Magnetism and Atmospheric Electricity, 47, 331

Lario, D., Aran, A., Gómez–Herrero, R., et al. 2013, The Astrophysical Journal, 767, 41

Lario, D., Kallenrode, M.-B., Decker, R. B., et al. 2006, The Astrophysical Journal, 653, 1531

Lario, D., Kwon, R.-Y., Vourlidas, A., et al. 2016, The Astrophysical Journal, 819, 72

Lario, D., Raouafi, N. E., Kwon, R.-Y., et al. 2014, The Astrophysical Journal, 797, 8

Lario, D., Roelof, E. C., Decker, R. B., & Reisenfeld, D. B. 2003, Advances in Space Research, 32, 579

Lee, M. A. 1983, Journal of Geophysical Research: Space Physics, 88, 6109

Lee, M. A. & Fisk, L. A. 1982, Space Science Reviews, 32, 205

Lee, M. A. & Ryan, J. M. 1986, The Astrophysical Journal, 303, 829

Lin, R., Dennis, B., Hurford, G., et al. 2002, Solar Physics, 210, 3

Lin, R. P. 1970, Solar Physics, 12, 266

Litvinenko, Y. E. 1996, The Astrophysical Journal, 462, 997

Liu, Y., Luhmann, J. G., Müller–Mellin, R., et al. 2008, The Astrophysical Journal, 689, 563

Luhn, A., Hoverstadt, D., Klecker, B., et al. 1985, in Proceedings of 19th International Cosmic Ray Conference, Vol. 4 (Goddard Space Flight Center), 241–244

Luhn, A. & Hovestadt, D. 1987, The Astrophysical Journal, 317, 852

Malandraki, O. E., Marsden, R. G., Lario, D., et al. 2009, The Astrophysical Journal, 704, 469

Manchester, IV, W. B., Gombosi, T. I., De Zeeuw, D. L., et al. 2005, The Astrophysical Journal, 622, 1225

Mann, G. 2015, Journal of Plasma Physics, 81, 475810601

Marsh, M. S., Dalla, S., Kelly, J., & Laitinen, T. 2013, The Astrophysical Journal, 774, 4

Mason, G., Gold, R., Krimigis, S., et al. 1998, Space Science Reviews, 86, 409

Mason, G. M., Desai, M. I., Cohen, C. M. S., et al. 2006, The Astrophysical Journal Letters, 647, L65

Mason, G. M., Korth, A., Walpole, P. H., et al. 2008, Space Science Reviews, 136, 257

Mason, G. M., Li, G., Cohen, C. M. S., et al. 2012, The Astrophysical Journal, 761, 104

Mason, G. M., Mazur, J. E., Dwyer, J. R., et al. 2004, The Astrophysical Journal, 606, 555

Mason, G. M., Reames, D. V., & Ng, C. K. 1991, in Proceedings of 22nd International Cosmic Ray Conference, Vol. 3 (NASA, Greenbelt, MD), 3.1–3.4

Masuda, S., Kosugi, T., Hara, H., Tsuneta, S., & Ogawara, Y. 1994, Nature, 371, 495

Mazur, J. E., Mason, G. M., Looper, M. D., Leske, R. A., & Mewaldt, R. A. 1999, Geophysical Research Letters, 26, 173

McComas, D., Bame, S., Barker, P., et al. 1998, Space Science Reviews, 86, 563

McGuire, R. E., Van Hollebeke, M. A. I., & Lal, N. 1983, in Proceedings of 18th International Cosmic Ray Conference, ed. N. Durgaprasad, Vol. 10 (Tata Institute of Fundamental Research, Bombay, India), 353

Melrose, D. B. 1985, Theoretical Problems Related to Stellar Radio Emission, ed. R. M. Hjellming & D. M. Gibson, Vol. 116 (Springer Netherlands), 351

Mewaldt, R., Cohen, C., Cook, W., et al. 2008, Space Science Reviews, 136, 285

Mewaldt, R. A., Cohen, C. M. S., Cummings, A. C., et al. 2008, in Proceedings of 30th International Cosmic Ray Conference, ed. R. Caballero, Vol. 1, 107–110

Mewaldt, R. A., Cohen, C. M. S., & Mason, G. M. 2006, Geophysical Monograph Series, Vol. 165, The Source Material for Large Solar Energetic Particle Events, ed. R. M. Natchimuthukonar Gopalswamy & J. Torsti (American Geophysical Union), 115–125

Mewaldt, R. A., Leske, R. A., Shih, A. Y., et al. 2010, in AIP Conference Proceedings, Vol. 1216, 12th International Solar Wind Conference, 592

Meyer, P., Parker, E., & Simpson, J. 1956, Physical Review, 104, 768

Mikić, Z. & Lee, M. A. 2006, Space Science Reviews, 123, 57

Miller, J. A. & Vinas, A. F. 1993, The Astrophysical Journal, 412, 386

Mitchell, J. W. & Hams, T. 2012, in Handbook of Particle Detection and Imaging, ed. C. Grupen & I. Buvat (Berlin, Heidelberg: Springer Berlin Heidelberg), 559–592

Moldwin, M. B. 2008, An Introduction to Space Weather (Cambridge University Press)

Möbius, E., Kistler, L., Popecki, M., et al. 1998, Space Science Reviews, 86, 449

Neupert, W. M. 1968, The Astrophysical Journal, 153, L59

Ng, C. K., Reames, D. V., & Tylka, A. J. 1999, Geophysical Research Letters, 26, 2145

Oetliker, M., Klecker, B., Hovestadt, D., et al. 1997, The Astrophysical Journal, 477, 495

Parker, E. N. 1957, Journal of Geophysical Research, 62, 509

Parker, E. N. 1958, The Astrophysical Journal, 128, 664

Parker, E. N. 1961, The Astrophysical Journal, 133, 1014

Pesce–Rollins, M., Omodei, N., Petrosian, V., et al. 2015, in Proceedings of 34th International Cosmic Ray Conference, ed. A. van den Berg, Proceedings of Science No. 128

Priest, E. & Forbes, T. 2002, The Astronomy and Astrophysics Review, 10, 313

Reames, D. 1990, The Astrophysical Journal Letters, 358, L63

Reames, D. 1995, Advances in Space Research, 15, 41

Reames, D. V. 1998, Space Science Reviews, 85, 327

Reames, D. V. 1999, Space Science Reviews, 90, 413

Reames, D. V. 2013, Space Science Reviews, 175, 53

Reames, D. V. 2014, Solar Physics, 289, 977

Reames, D. V., Meyer, J. P., & von Rosenvinge, T. T. 1994, The Astrophysical Journal Supplement Series, 90, 649

Reames, D. V., Ng, C. K., & Tylka, A. J. 2000, The Astrophysical Journal Letters, 531, L83

Richardson, I., von Rosenvinge, T., Cane, H., et al. 2014, Solar Physics, 289, 3059

Roelof, E. C. 1969, in Lectures in High–Energy Astrophysics, ed. H. Ögelman & J. R. Wayland, NASA Special Publications No. 199 (NASA, Goddard Space Flight Center), 111

Roelof, E. C., Decker, R. B., & Krimigis, S. M. 1983, Journal of Geophysical Research, 88, 9889

Roussev, I. I., Sokolov, I. V., Forbes, T. G., et al. 2004, The Astrophysical Journal Letters, 605, L73

Ruffolo, D. 1995, The Astrophysical Journal, 442, 861

Ryan, J. M. & Lee, M. A. 1991, The Astrophysical Journal, 368, 316

Scholer, M., Hovestadt, D., Klecker, B., Gloeckler, G., & Fan, C. Y. 1978, Journal of Geophysical Research, 83, 3349

Schwenn, R., Raymond, J. C., Alexander, D., et al. 2006, Space Science Reviews, 123, 127

Shibata, K., Masuda, S., Shimojo, M., et al. 1995, The Astrophysical Journal Letters, 451, L83

Simões, P. J. A. & Kontar, E. P. 2013, Astronomy and Astrophysics, 551, A135

Stone, E., Cohen, C., Cook, W., et al. 1998, Space Science Reviews, 86, 357

Sturrock, P. A. 1966, Nature, 211, 695

Sweet, P. A. 1958, in IAU Symposium Proceedings, Vol. 6, Electromagnetic Phenomena in Cosmical Physics, ed. B. Lehnert (International Astronomical Union), 123

Threlfall, J., Neukirch, T., Parnell, C. E., & Eradat Oskoui, S. 2015, Astronomy and Astrophysics, 574, A7

Torsti, J., Valtonen, E., Lumme, M., et al. 1995, Solar Physics, 162, 505

Tousey, R. 1973, Space Research, 13, 713

Turner, R. 2000, IEEE Transactions on Plasma Science, 28, 2103

Tylka, A. J., Cohen, C. M. S., Dietrich, W. F., et al. 2005, The Astrophysical Journal, 625, 474

Tylka, A. J., Malandraki, O. E., Dorrian, G., et al. 2013, Solar Physics, 285, 251

Tylka, A. J., Reames, D. V., & Ng, C. K. 1999, Geophysical Research Letters, 26, 2141

Usoskin, I. G., Solanki, S. K., Kovaltsov, G. A., Beer, J., & Kromer, B. 2006, Geophysical Research Letters, 33, L08107

von Rosenvinge, T., Reames, D., Baker, R., et al. 2008, Space Science Reviews, 136, 391

von Rosenvinge, T., Richardson, I., Reames, D., et al. 2009, Solar Physics, 256, 443

Vourlidas, A., Subramanian, P., Dere, K. P., & Howard, R. A. 2000, The Astrophysical Journal, 534, 456

Wiedenbeck, M. E., Mason, G. M., Cohen, C. M. S., et al. 2013, The Astrophysical Journal, 762, 54

Wild, J. P., Smerd, S. F., & Weiss, A. A. 1963, Annual Review of Astronomy and Astrophysics, 1, 291

Wimmer–Schweingruber, R. F., Crooker, N. U., Balogh, A., et al. 2006, Space Science Reviews, 123, 177

Zelina, P., Dalla, S., Cohen, C. M. S., & Mewaldt, R. A. 2017, The Astrophysical Journal, 835, 71

Zelina, P., Dalla, S., & Laitinen, T. 2015, in Proceedings of 34th International Cosmic Ray Conference, ed. A. van den Berg, Proceedings of Science No. 055

Zurbuchen, T. H. & Richardson, I. G. 2006, Space Science Reviews, 123, 31

Appendix A

A.1.1 Event #15 (2012 DOY 67–73.6)

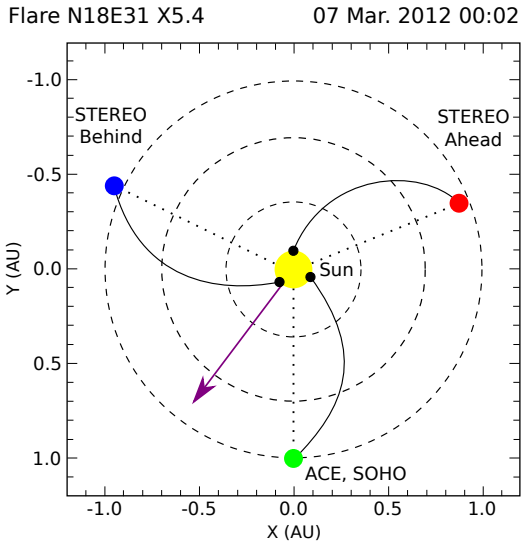

Figure A.1: A diagram of the position of ACE and SOHO (green), STEREO A (red) and B (blue) in the helioequatorial at the time of the X5.4 solar flare on 07 March 2012 at 00:02 UT. The purple arrow indicates the radial direction of the solar flare. The X1.3 solar flare from the same active region followed at 01:05 UT.

Two X–class flares erupted on 07 March 2012 (DOY 67) from AR 11429, an X5.4 flare at N18E31 at 00:02 UT and an X1.3 flare at N15E26 at 01:05 UT. Both flares were followed by halo CMEs with linear speed 2684 km/s observed by LASCO C2 at 00:24 UT and 1825 km/s at 01:31 UT, respectively. An interplanetary shock associated with the ICME was observed at STEREO B on 08 March at 13:36 UT (DOY 68.57). This event was also studied in more detail by Kouloumvakos et al. (2016).

The SEP event 2012 DOY 67–73.6 (event #15) ocurred when the spacecraft

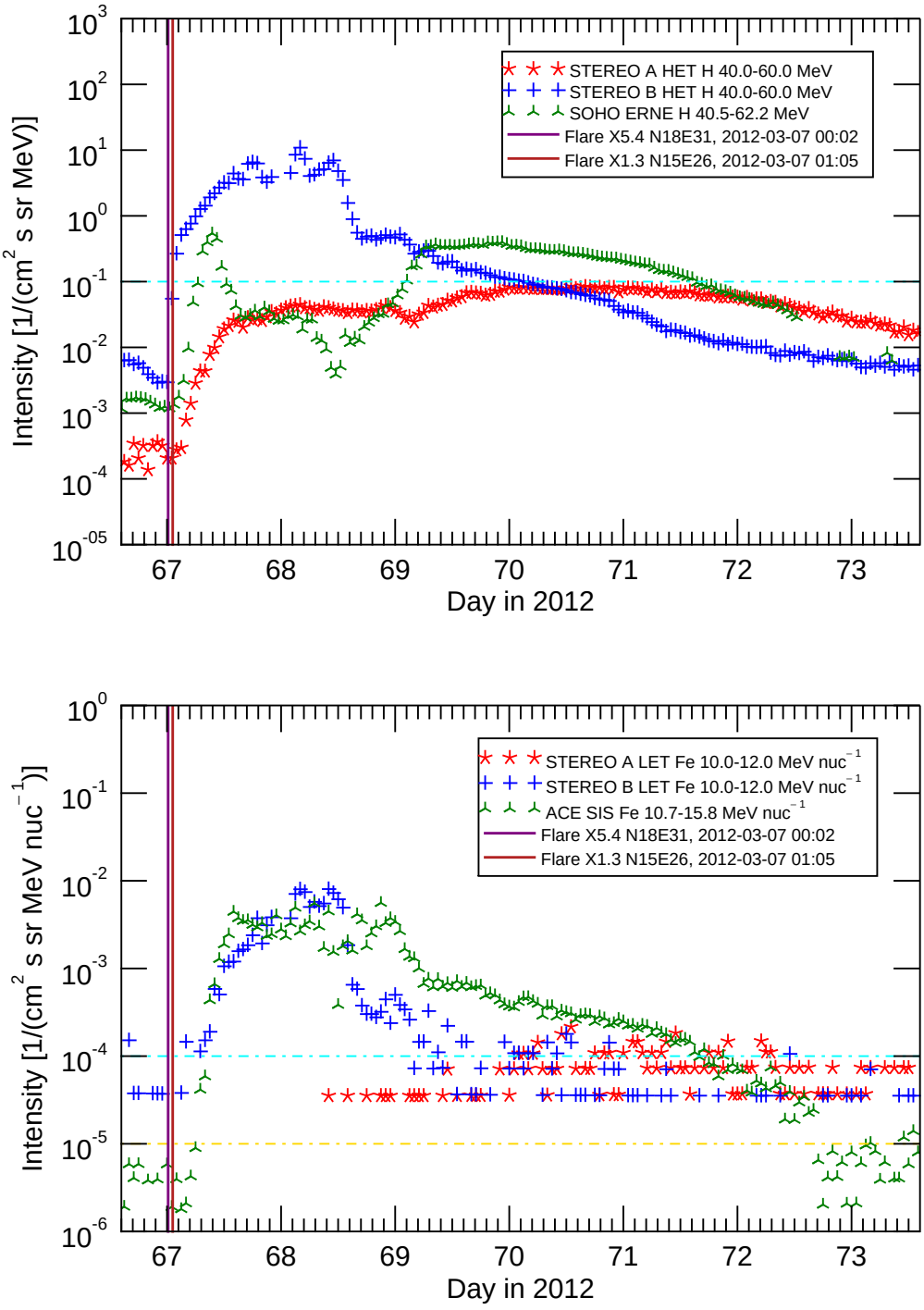

Figure A.2: Particle intensity time profiles for event #15 (2012 DOY 67–73.6). The plotted interval starts on DOY 66.6. Top plot: 40–60 MeV proton intensity for STA/LET (red), STB/LET (blue) and 40.5–62.2 MeV proton intensity for SOHO/ERNE (green). The cyan horizontal line is the proton intensity value $I_{\mathrm{H}} = 10^{-1}\,(\mathrm{cm^2\,s\,sr\,MeV})^{-1}$. Bottom plot: 10–12 MeV/nucleon Fe intensity for STA/LET (red), STB/LET (blue) and 10.7–15.8 MeV/nucleon Fe intensity for ACE/SIS (green). The vertical purple and brown lines denote the start time of the flares. The horizontal lines are the threshold values for STE/LET (cyan) and ACE/SIS (yellow).

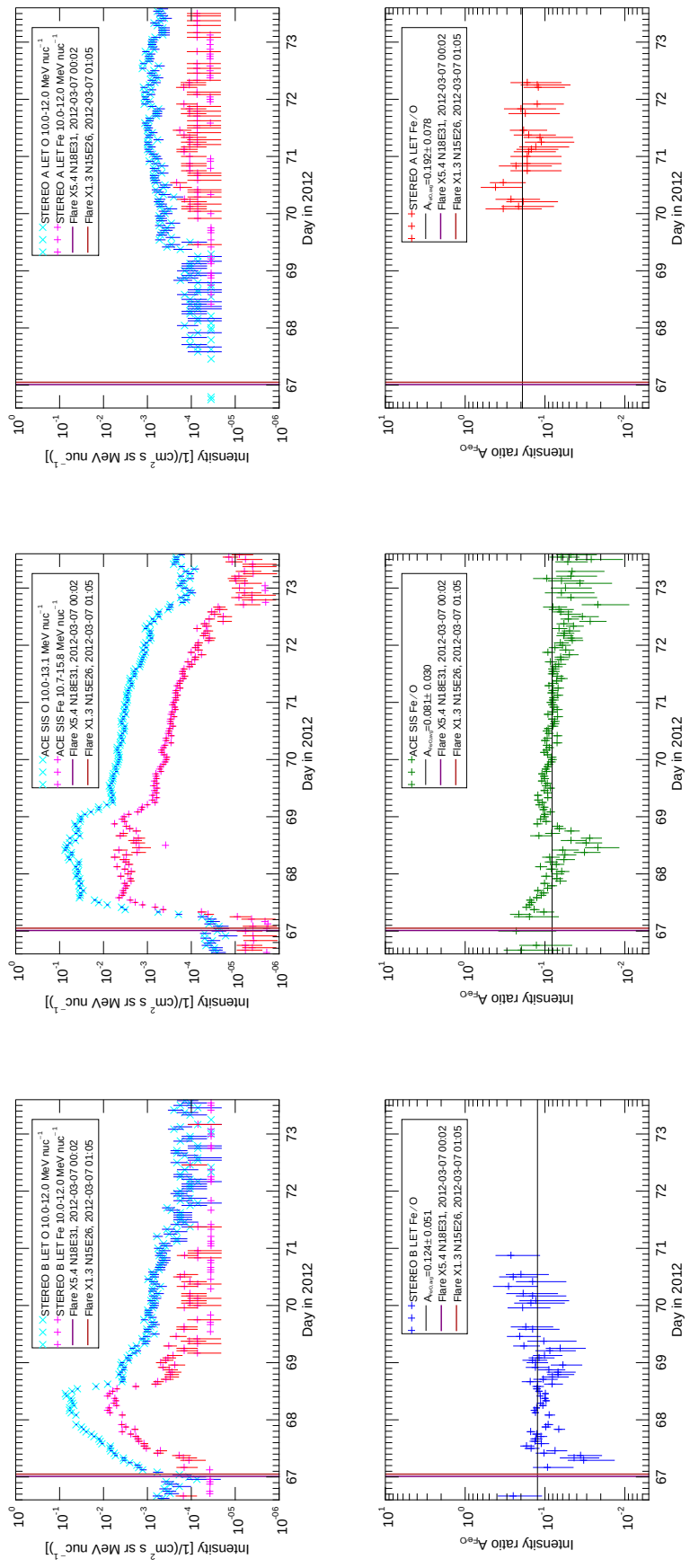

Figure A.3: Top row: Intensities of O (blue) and Fe (red) measured at STEREO B (left), ACE (middle) and STEREO A (right) event #15 (2012 DOY 67–73.6). The plotted interval starts on DOY 66.6. Bottom row: Fe/O ratio time profiles at the three spacecraft. The horizontal black line is the average Fe/O value at each spacecraft. The vertical purple and brown lines denote the start time of the flares.

were significantly (and almost equally) separated in longitude from each other, see Figure A.1. The angular separation, obtained using the STEREO orbit tool, between STEREO B and the Earth was –118 ° and between STEREO A and the Earth 109 °. The STEREO spacecraft were separated from each other by 133 °. The spacecraft were magnetically separated in longitude from the first flare by $\Delta\phi_{\mathrm{STB}} = 14\,^{\circ}$, $\Delta\phi_{\mathrm{ACE}} = -100\,^{\circ}$, $\Delta\phi_{\mathrm{STA}} = 144\,^{\circ}$, and from the second flare by $\Delta\phi_{\mathrm{STB}} = 19\,^{\circ}$, $\Delta\phi_{\mathrm{ACE}} = -94\,^{\circ}$, $\Delta\phi_{\mathrm{STA}} = 147\,^{\circ}$. In this event the spacecraft magnetic footpoints moved by approximately 1–2 ° within 1 hour between the flares.

The proton and Fe SEPs were observed by all three spacecraft, see Figure A.2, including the Fe intensity increase above the threshold values. Type III radio bursts, which indicate the injection of electrons into the IPM, were observed in association with both the X5.4 and the X1.3 flare, the former being significantly more intense than the latter. Type III and II radio bursts, detected using Wind/WAVES and STEREO/Waves, were also observed at all spacecraft positions.

The top graph in Figure A.2 shows proton intensity time profiles at the three spacecraft. STEREO A and B proton time profiles, observed by the HET instruments, are typical for poorly and well magnetically–connected observers, respectively. The protons measured by SOHO/ERNE show a sharp increase and a decrease, followed by another increase and then the gradual decrease towards the end of the SEP event. No interplanetary shocks were observed in this period at ACE or STEREO A. The Fe SEP time profiles at ACE and STEREO B, shown in the bottom plot in Figure A.2, show increase and gradual decrease of particle intensity. Fe SEPs at STEREO A are only observed on the fourth day of the SEP event (DOY 70) and rise only slightly above $I_{\mathrm{Fe}} = 10^{-1}\,(\mathrm{cm^2\,s\,sr\,MeV/nucleon})^{-1}$. Interestingly, the time periods during which the Fe intensity increases at all three spacecraft are observed above $I_{\mathrm{Fe}} = 10^{-1}\,(\mathrm{cm^2\,s\,sr\,MeV/nucleon})^{-1}$ are approximately similar to the periods of 40–60 MeV protons observed above $I_{\mathrm{H}} = 10^{-1}\,(\mathrm{cm^2\,s\,sr\,MeV})^{-1}$.

Fe and O intensity time profiles and the Fe/O values for the three spacecraft are shown in Figure A.3. The event–averaged Fe/O values calculated for each of the

three spacecraft are plotted as the black horizontal line in graphs in the bottom row of Figure A.3. The best magnetically connected spacecraft, STEREO B ($\Delta\phi_{\mathrm{STB}} = 14\,^{\circ}$), observed an Fe–poor event ($A_{\mathrm{Fe/O},avg} = 0.124$) as well as did ACE, for which this SEP event was eastern at ACE $A_{\mathrm{Fe/O},avg} = 0.081$, ($\Delta\phi_{\mathrm{ACE}} = -100\,^{\circ}$). However, the spacecraft furthest from the flare, at STEREO A ($\Delta\phi_{\mathrm{STA}} = 144\,^{\circ}$), observed an event rich in Fe $A_{\mathrm{Fe/O},avg}(\mathrm{STA}) = 0.192$.

A.1.2 Event #13 (2012 DOY 27–35)

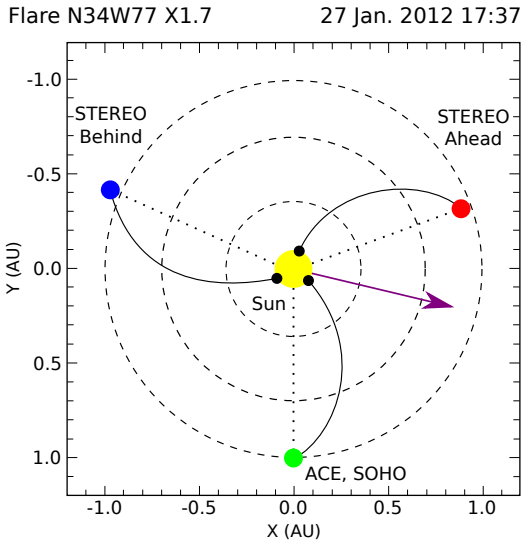

Figure A.4: A diagram of the position of ACE and SOHO (green), STEREO A (red) and B (blue) in the helioequatorial at the time of the X1.7 solar flare on 27 January 2012 at 18:37 UT. The purple arrow indicates the radial direction of the solar flare.

On 27 January 2012 at 17:37 UT (DOY 27.73) an X1.7 flare erupted from AR 11402 at N34W77 and it was accompanied by a fast CME with a speed of 2508 km/s, observed at 18:27 UT. Two closely following ICME shocks were observed at STEREO A on 29 January at 02:13 UT (DOY 29.09), and at 20:52 UT (DOY 29.87). ICME–associated shocks were also observed later at STEREO B on 30 January at 11:07 UT (DOY 30.46), and at Wind on 30 January at 15:43 UT (DOY 30.65).

The SEP event 2012 DOY 27–35 (event #13) was mainly observed at ACE, SOHO and STEREO A, as seen in Figure A.4. ACE was the best magnetically

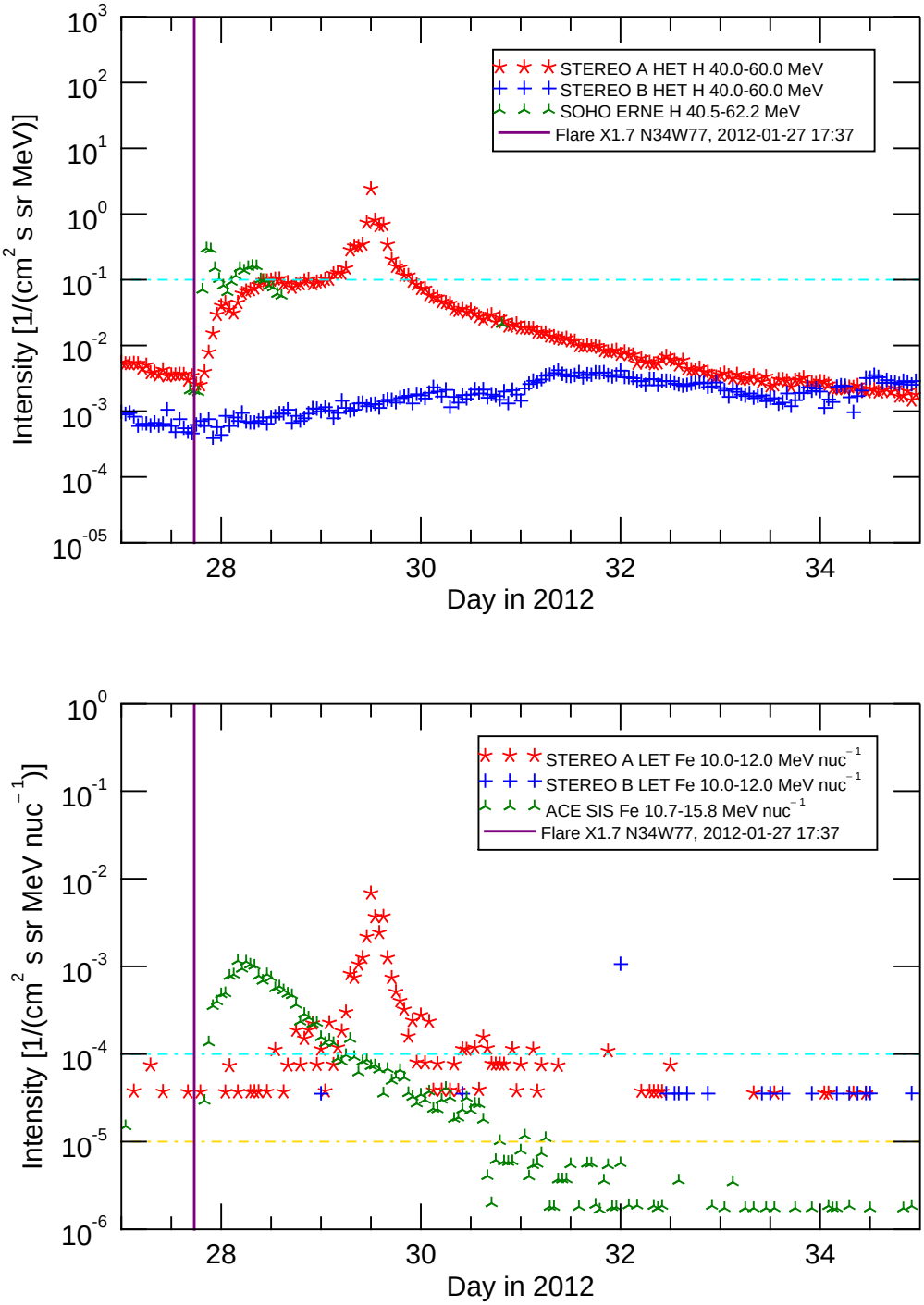

Figure A.5: Particle intensity time profiles for event #13 (2012 DOY 27–35). Top plot: 40–60 MeV proton intensity for STA/LET (red), STB/LET (blue) and 40.5–62.2 MeV proton intensity for SOHO/ERNE (green). The cyan horizontal line is the proton intensity value $I_{\mathrm{H}} = 10^{-1}$ (cm^2 s sr MeV)$^{-1}$. Bottom plot: 10–12 MeV/nucleon Fe intensity for STA/LET (red), STB/LET (blue) and 10.7–15.8 MeV/nucleon Fe intensity for ACE/SIS (green). The vertical purple line denotes the start time of the flare. The horizontal lines are the threshold values for STE/LET (cyan) and ACE/SIS (yellow).

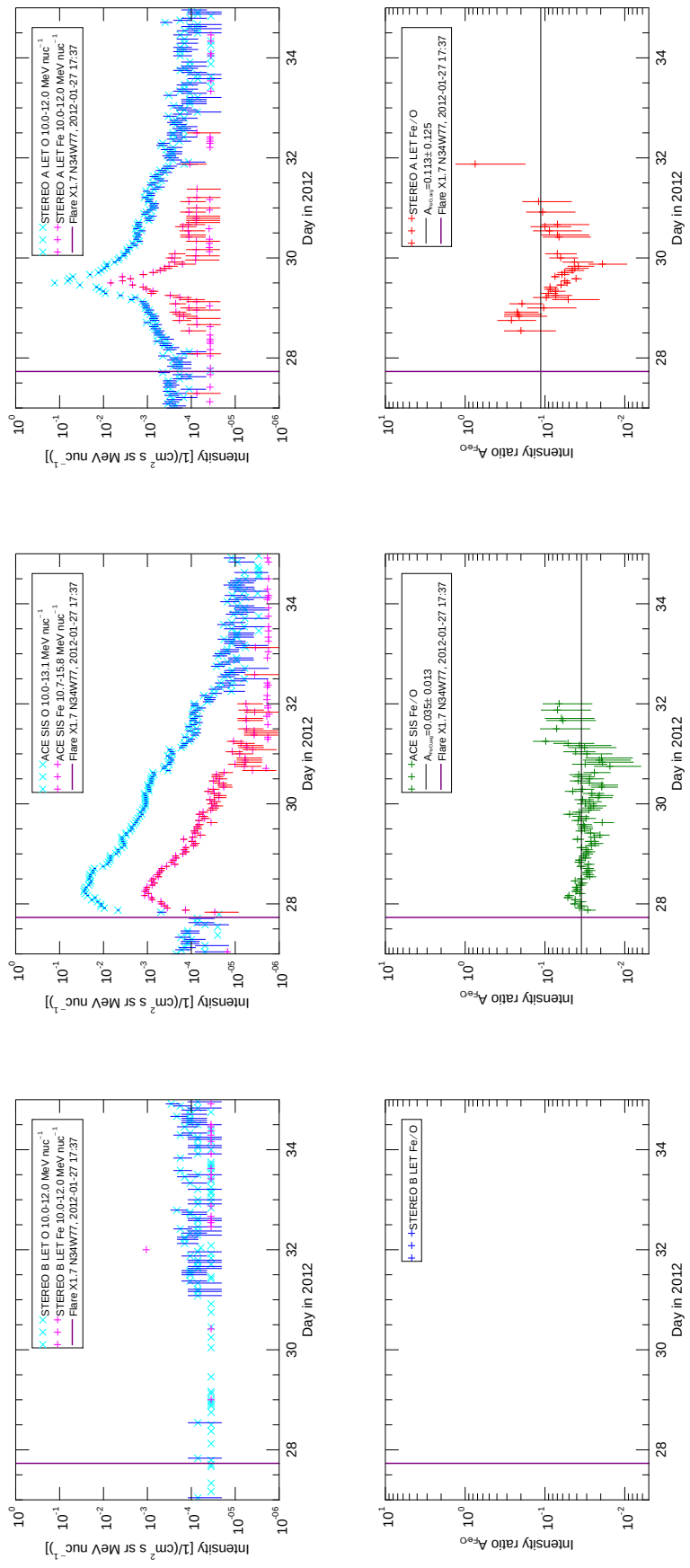

Figure A.6: Top row: Intensities of O (blue) and Fe (red) measured at STEREO B (left), ACE (middle) and STEREO A (right) event #13 (2012 DOY 27–35). Bottom row: Fe/O ratio time profiles at the three spacecraft. The horizontal black line is the average Fe/O value at each spacecraft. The vertical purple line denotes the start time of the flare.

connected spacecraft with $\Delta\phi_{\mathrm{ACE}} = 28\,^{\circ}$, followed by STEREO A $\Delta\phi_{\mathrm{STA}} = -92\,^{\circ}$ and STEREO B $\Delta\phi_{\mathrm{STB}} = 134\,^{\circ}$. At the time of the flare, the STEREO spacecraft were separated by 138 ° from each other, STEREO B from the Earth by –114 °, and STEREO A from the Earth by 108 °. Type II and III radio bursts were observed at all three spacecraft.

The top plot of Figure A.5 shows that the 40–60 MeV proton intensity SOHO rises rapidly after the start of the flare but is missing after approximately 1 day into the event. STEREO A observed proton intensity increase for an eastern event followed by a sharp peak in proton (and Fe) intensity midday on 29 January (DOY 29.5), followed by a gradual decrease. STEREO B only observed a mild increase in proton intensity. The Fe particle intensities above $I_{\mathrm{Fe}} = 10^{-4}\ (\mathrm{cm^2\,s\,sr\,MeV/nucleon})^{-1}$ lasted for approximately 1.25 days at ACE and 1 day at STEREO A, as seen in the bottom plot of Figure A.5. The periods where $I_{\mathrm{H}} > 10^{-1}\ (\mathrm{cm^2\,s\,sr\,MeV})^{-1}$ are timed similarly to the periods where $I_{\mathrm{Fe}} > 10^{-4}\ (\mathrm{cm^2\,s\,sr\,MeV/nucleon})^{-1}$ at ACE and STEREO A, but are shorter. STEREO B did not observe any Fe SEPs above the threshold value $I_{\mathrm{Fe}} = 10^{-4}\ (\mathrm{cm^2\,s\,sr\,MeV/nucleon})^{-1}$.

Fe and O intensity time profiles and the Fe/O values for the three spacecraft are shown in Figure A.6. In this SEP event, ACE, the best magnetically–connected spacecraft ($\Delta\phi_{\mathrm{ACE}} = 28\,^{\circ}$), observed an Fe–poor event and with a lower Fe content ($A_{\mathrm{Fe/O},avg} = 0.035$) than STEREO A ($A_{\mathrm{Fe/O},avg} = 0.113$), for which this SEP event was an eastern event ($\Delta\phi_{\mathrm{STA}} = -92\,^{\circ}$). A dip in the Fe/O value associated with the ESP peak at STEREO A.

A.1.3 Event #23 (2012 DOY 205–212)

On 23 July 2012 at 02:15 UT (DOY 205.09) a back–side flare erupted from AR 11520 at S15W134[4], and it was accompanied by a fast CME with a speed of 2003 km/s, observed at 02:36 UT. ICME shocks were observed at STEREO A on 23 July at 20:55 UT (DOY 205.87), and at STEREO B on the same day at 21:21 UT

[4]The position of the flare was identified at S17W20 from the STEREO A point of view, and at S17W141 from the Earth point of view (Gopalswamy et al. 2016).

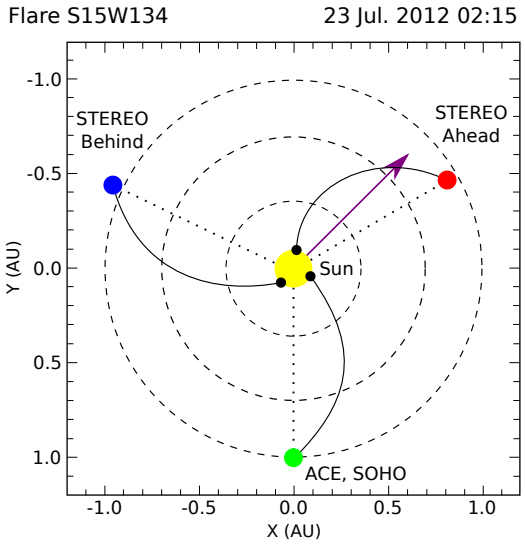

Figure A.7: A diagram of the position of ACE and SOHO (green), STEREO A (red) and B (blue) in the helioequatorial at the time of the back–side solar flare on 23 July 2012 at 02:15 UT. The purple arrow indicates the radial direction of the solar flare.

(DOY 205.89). An ICME–related shock was also observed later in the event at STEREO B on 28 July at 14:58 UT (DOY 210.62). This eruptive event attracted the attention of many researchers because the effects of this event could exceed those caused by the Carrington event in 1859, had it been directed towards the Earth (Baker et al. 2013).

The major particle increase of the SEP event 2012 DOY 205–215 (event #23) was observed at STEREO A, but SEP increases were also detected at other two spacecraft positions, as seen in Figure A.7. STEREO A was the best magnetically connected spacecraft with $\Delta\phi_{\mathrm{STA}} = -42\,^{\circ}$, followed by ACE with $\Delta\phi_{\mathrm{ACE}} = 75\,^{\circ}$ and STEREO B with $\Delta\phi_{\mathrm{STB}} = 174\,^{\circ}$. At the time of the flare, the STEREO spacecraft were separated by $124\,^{\circ}$ from each other, STEREO B from the Earth by $-115\,^{\circ}$, and STEREO A from the Earth by $121\,^{\circ}$. Both type II and III radio bursts were observed at all three spacecraft.

The top plot of Figure A.8 shows that the 40–60 MeV proton intensity at STEREO A rose rapidly, about 4 orders of magnitude in 3 hours, after the start of the flare, and peaked above $I_{\mathrm{H}} \approx 10^2\ (\mathrm{cm^2\,s\,sr\,MeV})^{-1}$. The protons at SOHO rose more gradually, followed by STEREO B, and their intensities culminated at $I_{\mathrm{H}} \approx$

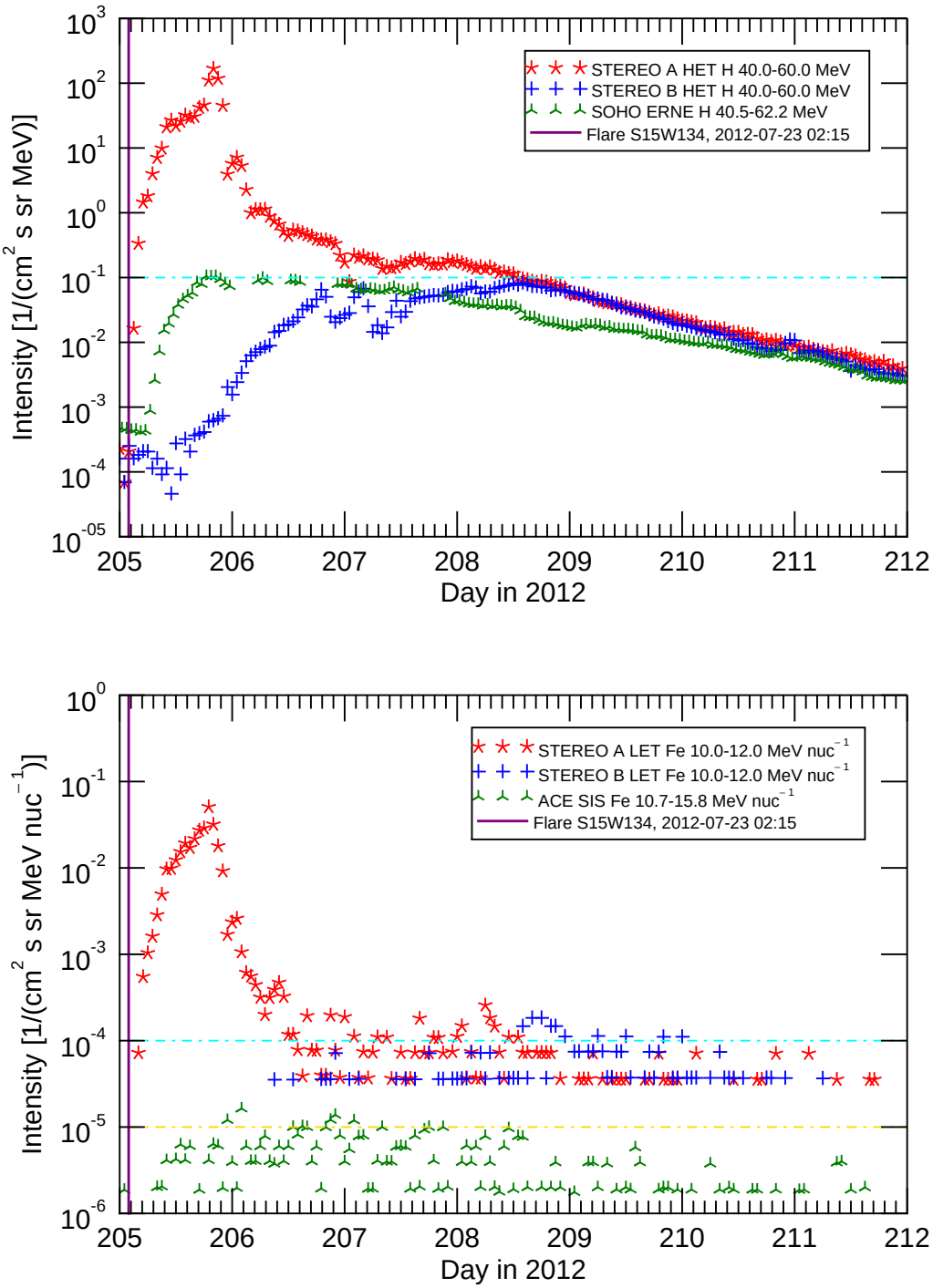

Figure A.8: Particle intensity time profiles for event #23 (2012 DOY 205–212). Top plot: 40–60 MeV proton intensity for STA/LET (red), STB/LET (blue) and 40.5–62.2 MeV proton intensity for SOHO/ERNE (green). The cyan horizontal line is the proton intensity value $I_{\mathrm{H}} = 10^{-1}\,(\mathrm{cm^2\,s\,sr\,MeV})^{-1}$. Bottom plot: 10–12 MeV/nucleon Fe intensity for STA/LET (red), STB/LET (blue) and 10.7–15.8 MeV/nucleon Fe intensity for ACE/SIS (green). The vertical purple line denotes the start time of the flare. The horizontal lines are the threshold values for STE/LET (cyan) and ACE/SIS (yellow).

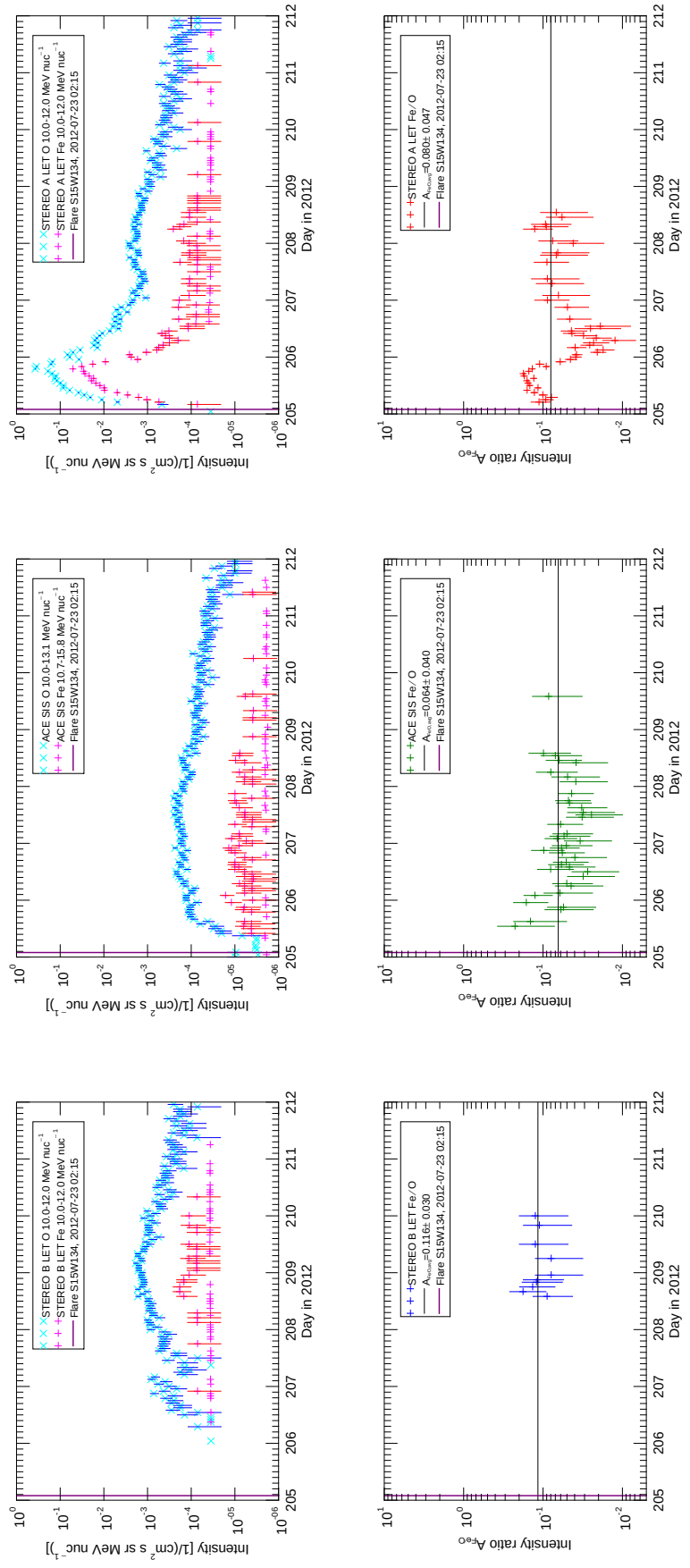

Figure A.9: Top row: Intensities of O (blue) and Fe (red) measured at STEREO B (left), ACE (middle) and STEREO A (right) event #23 (2012 DOY 205–212). Bottom row: Fe/O ratio time profiles at the three spacecraft. The horizontal black line is the average Fe/O value at each spacecraft. The vertical purple line denotes the start time of the flare.

10^{-1} $(\mathrm{cm}^2\,\mathrm{s}\,\mathrm{sr}\,\mathrm{MeV})^{-1}$. The Fe particle intensity at STEREO A above the threshold value $I_{\mathrm{Fe}} = 10^{-4}\,(\mathrm{cm}^2\,\mathrm{s}\,\mathrm{sr}\,\mathrm{MeV/nucleon})^{-1}$ lasted for approximately 1.5 days. The Fe SEP intensities at ACE and STEREO B only rose slightly above the threshold values, $I_{\mathrm{Fe}} = 10^{-5}(\mathrm{cm}^2\,\mathrm{s}\,\mathrm{sr}\,\mathrm{MeV/nucleon})^{-1}$ for ACE and $I_{\mathrm{Fe}} = 10^{-4}(\mathrm{cm}^2\,\mathrm{s}\,\mathrm{sr}\,\mathrm{MeV/nucleon})^{-1}$ for STEREO B, but sufficiently enough to calculate the Fe/O ratio values. Fe and O intensity time profiles and the Fe/O values for the three spacecraft are shown in Figure A.9.

In this SEP event, ACE, for which the SEP event was a western event ($\Delta\phi_{\mathrm{ACE}} = 75\,^\circ$), observed an Fe–poor event with lower Fe content ($A_{\mathrm{Fe/O},avg} = 0.064$) than STEREO A ($A_{\mathrm{Fe/O},avg}(\mathrm{STA}) = 0.080$), for which this SEP event was an eastern event ($\Delta\phi_{\mathrm{STA}} = -42\,^\circ$). The Fe/O value at STEREO B, which was magnetically connected to the opposite side of the Sun ($\Delta\phi_{\mathrm{STB}} = 174\,^\circ$) at the time of the flare, was only observed very late in the event, on DOY 208–210, but of the three spacecraft it had the highest Fe/O value $A_{\mathrm{Fe/O},avg} = 0.116$.

A.1.4 Event #28 (2013 DOY 101–105)

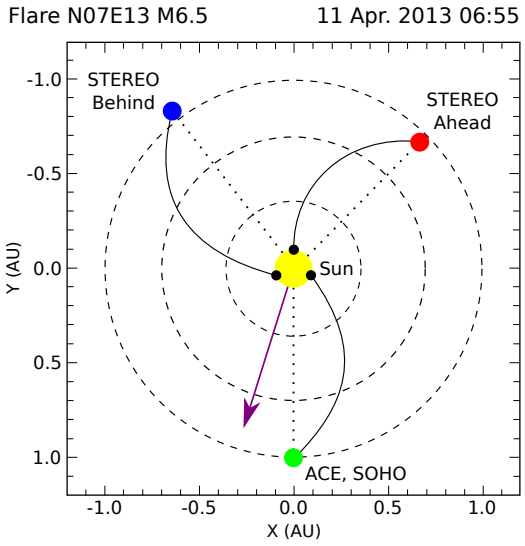

Figure A.10: A diagram of the position of ACE and SOHO (green), STEREO A (red) and B (blue) in the helioequatorial at the time of the M6.5 solar flare on 11 April 2013 at 06:55 UT. The purple arrow indicates the radial direction of the solar flare.

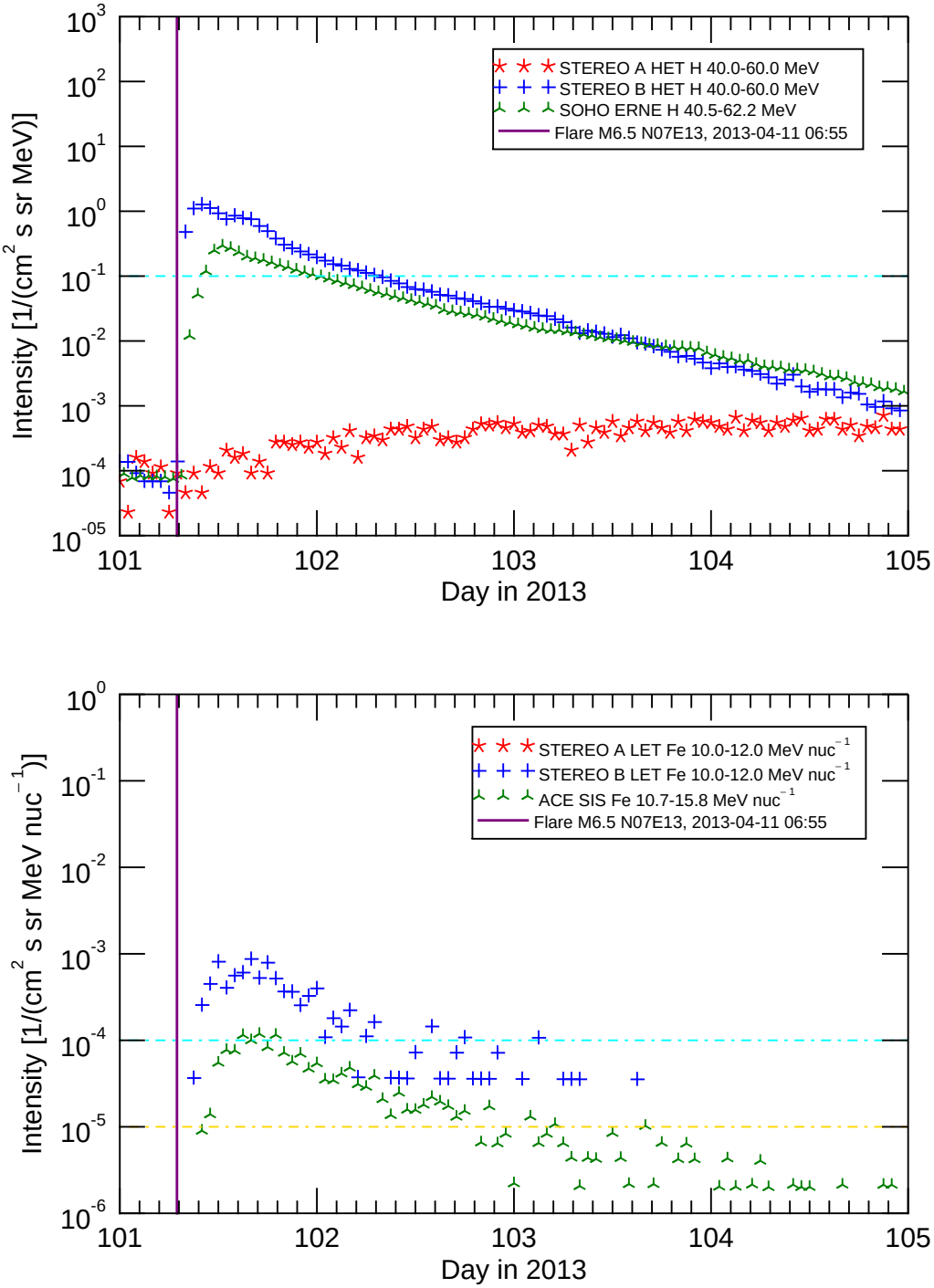

Figure A.11: Particle intensity time profiles for event #28 (2013 DOY 101–105). Top plot: 40–60 MeV proton intensity for STA/LET (red), STB/LET (blue) and 40.5–62.2 MeV proton intensity for SOHO/ERNE (green). The cyan horizontal line is the proton intensity value $I_{\mathrm{H}} = 10^{-1}\,(\mathrm{cm^2\,s\,sr\,MeV})^{-1}$. Bottom plot: 10–12 MeV/nucleon Fe intensity for STA/LET (red), STB/LET (blue) and 10.7–15.8 MeV/nucleon Fe intensity for ACE/SIS (green). The vertical purple line denotes the start time of the flare. The horizontal lines are the threshold values for STE/LET (cyan) and ACE/SIS (yellow).

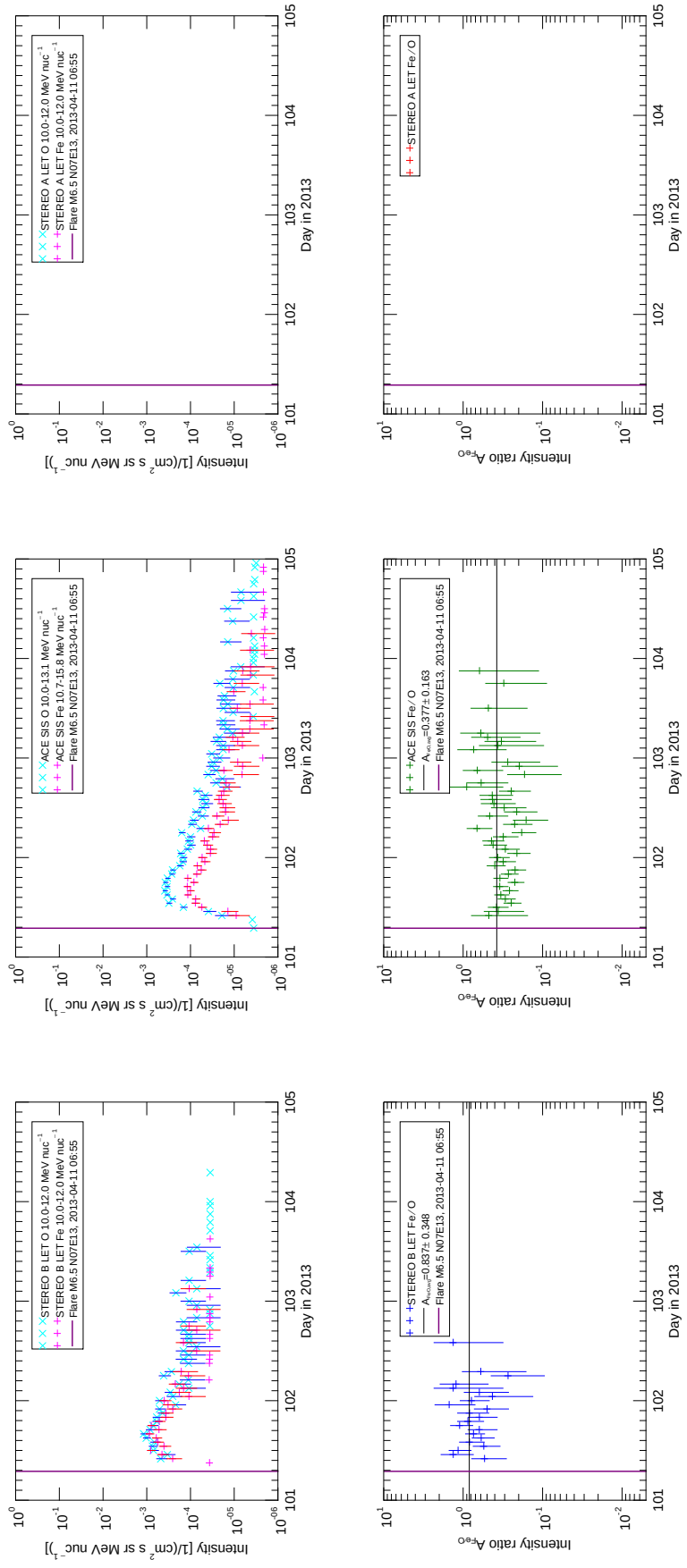

Figure A.12: Top row: Intensities of O (blue) and Fe (red) measured at STEREO B (left), ACE (middle) and STEREO A (right) event #28 (2013 DOY 101–105). Bottom row: Fe/O ratio time profiles at the three spacecraft. The horizontal black line is the average Fe/O value at each spacecraft. The vertical purple line denotes the start time of the flare.

On 11 April 2013 at 06:55 UT (DOY 101.29), a moderately strong M6.5 flare, erupted from AR 11719 at N07E13, and it was accompanied by a CME with a speed of 861 km/s, observed at 07:24 UT. An ICME–associated shock was observed later in the event at ACE on 13 April at 22:13 UT (DOY 103.93). This SEP event was also studied in more detail by Cohen et al. (2014).

The SEP event 2013 DOY 101–105 (event #28) was observed at STEREO B, and at ACE and SOHO, in which the flare was almost centered between these spacecraft, as seen in Figure A.10. None of the three spacecraft can be considered magnetically well–connected, STEREO B with $\Delta\phi_{\mathrm{STB}} = 54\,^{\circ}$, ACE with $\Delta\phi_{\mathrm{ACE}} = -78\,^{\circ}$, and STEREO A with $\Delta\phi_{\mathrm{STA}} = 166\,^{\circ}$. At the time of the flare, the STEREO spacecraft were separated by 85 °, STEREO B from the Earth by –142 °, and STEREO A from the Earth by 133 °. Type III radio bursts were observed at all three spacecraft, but the type II radio bursts were only observed at STEREO B and Wind (Cohen et al. 2014).

The top plot of Figure A.11 shows that the 40–60 MeV proton intensities at SOHO and STEREO B rose rapidly after the start of the flare. The protons at STEREO A rose only very gradually by 1 order of magnitude over the SEP event. The Fe particle intensity increase above $I_{\mathrm{Fe}} = 10^{-4}\ (\mathrm{cm^2\,s\,sr\,MeV/nucleon})^{-1}$ at STEREO B lasted approximately 1 day, similar to the period of 40–60 MeV protons $I_{\mathrm{H}} > 10^{-1}\ (\mathrm{cm^2\,s\,sr\,MeV})^{-1}$ at STEREO B, and was about 10 times higher than Fe intensity observed at ACE, as seen in the bottom plot of Figure A.9. No Fe SEPs were observed at STEREO A.

In this SEP event, neither STEREO B nor ACE were magnetically well connected to the flare ($\Delta\phi_{\mathrm{STB}} = 54\,^{\circ}$, $\Delta\phi_{\mathrm{ACE}} = -78\,^{\circ}$), but both spacecraft observed Fe–rich events, $A_{\mathrm{Fe/O},avg} = 0.837$ at STEREO B and $A_{\mathrm{Fe/O},avg} = 0.377$ at ACE.

Appendix B

Appendix B includes a copy of Zelina et al. (2017): Zelina, P., Dalla, S., Cohen, C. M. S., & Mewaldt, R. A. 2017. "Time evolution of elemental ratios in solar energetic particle events." *The Astrophysical Journal*, Vol. 835, pp. 71 (13 pages).

Erratum

The published text in Zelina et al. (2017), page 4 (page XXI in Appendix B), line 3 in the right column, describing Figure 2[5] on page 5 (page XXII Appendix B) reads:

> The ratio profiles also show that the slope of temporal variation scales with S, where, e.g., Mg/O shown in Figure 2(a), a ratio with $S > 1$, remains almost unchanged over the duration of the SEP event. The O/C ratio with $S = 1.09$, Figure 2(b), shows a slight but steady decrease over time. The rate of decay of Si/O with $S = 1.11$, Figure 2(c), is higher than that of O/C, but the duration of Si/O evolution is also shorter due to the lower relative abundance of silicon in the SEP event.

The correct text should read:

> The ratio profiles also show that the slope of temporal variation scales with S, where e.g., Mg/O shown in Figure 2(b), a ratio with $S \approx 1$, remains almost unchanged over the duration of the SEP event. The C/O ratio with $S = 0.92$, Figure 2(a), shows a slight but steady increase over

[5]This figure is identical to the one shown in top panels in Figure 5.2 on page 75.

time, and the Si/O ratio with $S = 1.11$, Figure 2(c), shows a decrease. The duration of Si/O is also shorter than due to the lower relative abundance of silicon in the SEP event.

The Astrophysical Journal, 835:71 (13pp), 2017 January 20 doi:10.3847/1538-4357/aa5274

TIME EVOLUTION OF ELEMENTAL RATIOS IN SOLAR ENERGETIC PARTICLE EVENTS

P. Zelina[1], S. Dalla[1], C. M. S. Cohen[2], and R. A. Mewaldt[2]
[1] Jeremiah Horrocks Institute, University of Central Lancashire, Preston PR1 2HE, UK; pzelina@uclan.ac.uk
[2] California Institute of Technology, Pasadena, CA 91125, USA
Received 2016 October 17; revised 2016 December 2; accepted 2016 December 5; published 2017 January 19

ABSTRACT

Heavy ion ratio abundances in solar energetic particle (SEP) events, e.g., Fe/O, often exhibit decreases over time. Using particle instruments on the *Advanced Composition Explorer*, *Solar and Heliospheric Observatory* and *Solar Terrestrial Relations Observatory* spacecraft, we analyzed heavy ion data from 4 SEP events taking place between 2006 December and 2014 December. We constructed 36 different ionic pairs and studied their time evolution in each event. We quantified the temporal behavior of abundant SEP ratios by fitting the data to derive a decay time constant B. We also considered the ratio of ionic mass-to-charge for each pair, the S value given, e.g., for Fe/O by $S_{\mathrm{Fe/O}} = (M/Q)_{\mathrm{Fe}}/(M/Q)_{\mathrm{O}}$. We found that the temporal behavior of SEP ratios is ordered by the value of S: ratios with $S > 1$ showed decreases over time (i.e., $B < 0$) and those with $S < 1$ showed increases ($B > 0$). We plotted B as a function of S and observed a clear monotonic dependence: ratios with a large S decayed at a higher rate. A prominent discontinuity at $S = 2.0$ (corresponding to He/H) was found in three of the four events, suggesting anomalous behavior of protons. The X/H ratios often show an initial increase followed by a decrease, and decay at a slower rate. We discuss possible causes of the observed B versus S trends within current understanding of SEP propagation.

Key words: Sun: abundances – Sun: heliosphere – Sun: particle emission

1. INTRODUCTION

Solar energetic particles (SEPs) are ions and electrons released into the interplanetary medium due to solar eruptive activity. They are accelerated by solar flares and coronal mass ejections (CMEs) and can be observed as particle intensity increases by instruments onboard spacecraft. SEPs (mainly H, He, electrons) can be detected at locations widely separated from the parent eruptive event in longitude and latitude (e.g., Dalla et al. 2003; Gómez-Herrero et al. 2015). In large, so-called gradual SEP events, mean ionic abundances are similar to the solar wind ones but event-to-event variation of ratios such as Fe/O can vary by significantly more than typical solar wind ratios. Type II radio bursts from the associated CME-driven shock are observed in addition to type III radio bursts generated by particles released from solar flares. The wide longitudinal extent of SEP events is usually ascribed to acceleration at extended regions, such as shocks, because according to the accepted paradigm for SEP propagation, SEPs travel along magnetic field lines without significant transport perpendicular to the average interplanetary magnetic field (Reames 1999). SEP events with high Fe/O abundance and rich in ^{3}He are called impulsive events. These events are of short duration and commonly associated only with type III radio bursts. According to the standard paradigm, impulsive SEPs should be detectable only in narrow regions of $<20°$ in longitude, i.e., locations with good magnetic connection to the flare.

Since the launch of the *Solar Terrestrial Relations Observatory* (*STEREO*) spacecraft, there have been many reports of simultaneous observations by multiple spacecraft that showed that proton and electron SEP events can indeed be detected at locations widely separated in longitude (e.g., Dresing et al. 2012, 2014; Lario et al. 2013; Richardson et al. 2014; Gómez-Herrero et al. 2015). In a study of ^{3}He rich events detected by multiple spacecraft, Wiedenbeck et al. (2013) reported an impulsive event that was observed by three spacecraft, two of which were separated by 136°, but as part of a statistical study of 17 impulsive events they showed that simultaneous SEP detections at two spacecraft at longitudinal separation $>60°$ were not uncommon. An SEP event rich in Fe was reported by Cohen et al. (2014), where two spacecraft separated by 135° in longitude detected enhanced average Fe/O values, which showed a dependence on longitude. In separate studies, Gómez-Herrero et al. (2015) and Zelina et al. (2015) used data from three spacecraft and found that Fe and O SEPs from a single parent active region can reach locations widely separated in longitude and be detected over almost 360°.

SEP ratios, such as Fe/O, often decrease over the duration of an SEP event. Using 3 hr averaged data, Scholer et al. (1978) observed Fe/O ratios decreasing in time while the C/O ratios were time independent. Tylka et al. (1999) reported observations of the temporal evolution of several heavy ion ratios during the 1998 April 20 SEP event that were ordered by their M/Q values, where M is atomic mass of an SEP ion and Q its charge. Mason et al. (2012) studied the temporal evolution of Fe/O, O/He, and He/H ratios in 17 SEP events, where, in the majority of events, the ratios exhibited temporal variation. Tylka et al. (2013) used *Ulysses* and near-Earth spacecraft data to show that Fe SEPs can reach high heliographic latitudes. They also observed the characteristic Fe/O decrease over time at the two spacecraft, both of which had poor magnetic connection to the parent flare. In all the considered events analyzed by Zelina et al. (2015) the Fe/O ratio decreased over time, a behavior therefore identified as a common feature of SEP events.

Several researchers have proposed interpretations of the observed time dependence of elemental ratios, either as an effect of acceleration or of transport. It was suggested that the high Fe/O ratio early in the SEP event is a result of an initial flare component (rich in Fe) while the decrease that follows is associated with a shock-accelerated component (with lower

Table 1
Details of Solar Flares and Coronal Mass Ejections (CMEs) Obtained from SolarMonitor.org and the CDAW CME Catalog

	Event #1	#2	#3	#4
Year	2012	2006	2014	2014
Flare start time	Aug 31/19:45	Dec 13/02:14	Sep 01/11:00	Feb 25/00:39
Flare class	C8	X3.4	X2.1	X4.9
Solar disk location	S16E42	S07W22	N14E129	S12E77
CME start time	22:00	02:54	11:12	01:25
CME speed (km s^{-1})	1442	1774	1901	2147

Note. The position of the backside flare (event #3) was calculated using *STEREO* FITS files. The flare class for this event was estimated by Pesce-Rollins et al. (2015).

Table 2
Details of the SEP Events

	Event #1	#2	#3	#4
Year	2012	2006	2014	2014
Duration (DOY)	244–248	347–349	244–248	56–60
Best connected s/c	*STB*	*SOHO,ACE*	*STB*	*STB*
SW speed (km s^{-1})	325	650	450	500
$\Delta\phi$	−5°	−17°	−25°	32°
$\Delta\theta$	−12°	−6°	21°	−19°
Fe/O A_2/A_1	0.030	0.121	0.027	0.150
Fe/O Δt (day)	1.25	1.25	1.25	2.75
Fe/O B (day^{-1})	−0.92 ± 0.06	−0.54 ± 0.06	−1.1 ± 0.1	−0.01 ± 0.02

Note. The duration is the time span with good Fe count statistics in *day of year* units, for which heavy ion ratios are plotted and analyzed. $\Delta\phi$ is longitudinal separation (positive is flare west of the spacecraft footpoint), $\Delta\theta$ is latitudinal separation (positive is flare north of the spacecraft), A_2/A_1 is the ratio of Fe/O values (final/initial), Δt the time over which the Fe/O decrease occurs, and B is the derived exponential decay time constant.

Fe/O) later in the event (Cane et al. 2003). Tylka et al. (1999) explained it as due to the ions with high M/Q (i.e., Fe) escaping the accelerating shock region more easily. Others proposed that the observed time dependence is a propagation effect due to the rigidity dependence of the mean free path (Scholer et al. 1978; Mason et al. 2012), or more generally transport effects (Tylka et al. 2013).

The observed temporal variation of SEP ratios may be related to M/Q -dependent cross-field transport of SEPs, where SEPs with different M/Q follow different trajectories. Gradient and curvature drifts in the Parker spiral magnetic field depend on M/Q and kinetic energy (Dalla et al. 2013). Full-orbit simulations of heavy ions show that drifts are an important mechanism of perpendicular transport that can distribute SEPs across the interplanetary magnetic field (Marsh et al. 2013). The charge state affects how much a particle can drift across the mean magnetic field, since particles with higher M/Q exhibit more drift. Simulations by Dalla et al. (2015, 2016) show that an SEP model including drifts can qualitatively reproduce the decrease in time of the Fe/O ratio.

In this work, we studied the temporal behavior of SEP abundance ratios for four SEP events in a quantitative manner. We systematically analyzed the decay in time of a number of elemental ratios, including Fe/O and less commonly used ratios such as Fe/C, Fe/Mg, and Fe/Si. We quantified the temporal evolution of SEP ratios by fitting the time profiles to an exponential function and deriving a decay time constant, and studied any correlations of this parameter with ionic M/Q values of the two species in the ratio. Section 2 presents SEP data for the selected events, followed by a Discussion (Section 3) and Conclusions (Section 4).

2. OBSERVATIONS

For the study of heavy ion particles, we used SEP data measured in situ by the following particle instruments: Solar Isotope Spectrometer (SIS; Stone et al. 1998) onboard *Advanced Composition Explorer* (*ACE*), Energetic and Relativistic Nuclei and Electron (ERNE; Torsti et al. 1995) onboard *SOlar and Heliospheric Observatory* (*SOHO*), and Low Energy Telescopes (LET; Mewaldt et al. 2008) and High Energy Telescopes (HET; von Rosenvinge et al. 2008) onboard the *STEREO Ahead* (*STA*) and *Behind* (*STB*) spacecraft.

We examined SEP events between 2006 December and 2014 December with the Fe particle intensity above 10^{-3} (cm^2 s sr MeV/nuc)$^{-1}$ in the 10–12 MeV nuc^{-1} energy channel for *STEREO* and 10^{-4} (cm^2 s sr MeV/nuc)$^{-1}$ in the 10.7–15.8 MeV nuc^{-1} energy channel for *ACE*. The lower threshold in the *ACE* data is due to ∼10x larger geometrical factor of the *ACE*/SIS instrument compared to the *STEREO*/LET instruments. We selected four SEP events: 2006 December 13, 2012 August 31, 2014 February 25 and 2014 September 1, which have intensity profiles with monotonic rise and decay phases. Each of the selected events was linked to a single parent active region. Details of the solar eruptive events are given in Table 1.

Details of the SEP events are given in Table 2. For each SEP event we used the spacecraft with the best magnetic connection to the flare. In all events other spacecraft did not measure sufficient particle intensities of heavy ion SEPs to quantitatively analyze the observed temporal variation of heavy ion ratios, or intensity time profiles did not show monotonic rise and decay phase. In Table 2, the duration of an SEP event

Table 3
Atomic Mass Number M, Ionic Charge State Number Q, and M/Q of Abundant SEP ions

Element	M	Q	M/Q
H	1	1.00	1.00
He	4	2.00	2.00
C	12	5.70	2.11
N	14	6.37	2.20
O	16	7.00	2.29
Ne	20	9.05	2.21
Mg	24	10.70	2.24
Si	28	11.00	2.55
Fe	56	14.90	3.76

Note. The ionic charge states are from Luhn et al. (1985) except for H and He, which are assumed to be fully ionized. The heavy ion charge state values are subject to 5% systematic uncertainty.

indicates the number of days when there were sufficient Fe particles to yield good statistics. We used the local solar wind speed value at the beginning of an SEP event at the spacecraft to calculate the nominal Parker spiral footpoint of the spacecraft on the solar surface ϕ_{sc}. The angular separation in longitude between the flare and the spacecraft is calculated as $\Delta\phi = \phi_{flare} - \phi_{sc}$, where ϕ_{flare} is the longitude of the flare. A positive $\Delta\phi$ means that the flare is western with respect to the observer footpoint. In a similar manner, latitudinal separation between the flare and the observer was calculated as $\Delta\theta = \theta_{flare} - \theta_{sc}$. A positive $\Delta\theta$ means the flare is north of the spacecraft.

For each event, time intensity profiles for all abundant elements, which include H, He, C, N, O, Ne, Mg, Si, and Fe, were analyzed and ionic were ratios constructed. For ratios observed by *STEREO*/LET, we used the lowest energy channel common for all elements that is 4.0–4.5 MeV nuc^{-1}. *ACE*/SIS energy channels do not cover exactly the same energy range as *STEREO*/LET for any of the heavy ions. Therefore, we used the closest available channels to the *STEREO*/LET energy channel. Note that the heavy ion energy bins in *ACE*/SIS data change depending on the analyzed element due to the SIS instrument response function for the analyzed nuclei (see Stone et al. 1998, Figure 19 for reference). For example, the lowest energy bin for He is 3.4–4.7 MeV nuc^{-1} while the lowest Fe energy bin is 10.7–15.8 MeV nuc^{-1}. The energy channels for a pair of two elements were chosen to be the closest to each other, e.g., in order to obtain the Fe/O ratio, Fe intensity at 10.7–15.8 MeV nuc^{-1} was divided by O intensity measured at 10.0–13.1 MeV nuc^{-1}. We used proton measurements from *SOHO*/ERNE to complement the heavy ion data by *ACE*/SIS. For all the intensities, uncertainties were calculated as $\sigma = \sqrt{N}$, where N is the particle count within the accumulation time.

For each pair of SEP elements X_1 and X_2 we define a parameter S given by

$$S_{X_2/X_1} \equiv \left(\frac{M_2}{Q_2}\right) \Big/ \left(\frac{M_1}{Q_1}\right) \quad (1)$$

where M_i is atomic mass number and Q_i is the ionic charge state in elementary charge units, for species X_i.

SEPs in the interplanetary medium are partially ionized. Measurement of the charge state Q is challenging and is not routinely carried out for all SEP events (Klecker et al. 2006).

Table 4
Table of S Values, for all Common Pairs of Abundant SEP Elements

Element (1)	Element (2)							
	He	C	N	O	Ne	Mg	Si	Fe
H	2.00	2.11	2.20	2.29	2.21	2.24	2.55	3.76
He	1	1.05	1.10	1.14	1.10	1.12	1.27	1.88
C	⋯	1	1.04	1.09	1.05	1.07	1.21	1.79
N	⋯	⋯	1	1.04	1.01	1.02	1.16	1.71
O	⋯	0.92	0.96	1	0.97	0.98	1.11	1.64
Ne	⋯	⋯	⋯	⋯	1	1.01	1.15	1.70
Mg	⋯	⋯	⋯	⋯	⋯	1	1.13	1.68
Si	⋯	⋯	⋯	⋯	⋯	⋯	1	1.48

Note. Ratio $= \frac{\text{Element(2)}}{\text{Element(1)}}$.

For this reason, for the purpose of calculating the S-values, we use charge state measurements by Luhn et al. (1985), shown in Table 3, which provide an estimate of ionic charge states at ≈0.5–3.3 MeV nuc^{-1} in a similar energy range to the one considered in our study. The charge state measurements given in Luhn et al. (1985), obtained by averaging over a number of SEP events, are subject to systematic errors of 5%. It should be noted that Q can vary event-to-event, and in some SEP events it increases with energy (Klecker et al. 2006; Mewaldt et al. 2006, pp. 115–125).

For the event of 2006 December 13, one of the events in our analysis, we estimate from the SAMPEX data, using the same method described by Oetliker et al. (1997), that the iron charge state was $Q_{Fe} = 16.2^{+1.7}_{-1.5}$ at 25–90 MeV nuc^{-1}. Therefore we can say that, for this event, the value of Q at the lower energies that we consider in our study, as given in Table 3, is not inconsistent with the measured value at higher energies.

To our best knowledge there were no operational instruments measuring ionic charges in the other three events. Charge states are known to vary event-to-event, and the charge state of iron in particular can take a broad range of values $Q_{Fe} \approx$ 10–20 (Labrador et al. 2005). Other ionic charge states vary too but to a lesser extent.

We use the atomic mass number of the dominant isotope as a mass estimate for an SEP species. The difference between this value and the isotopic SEP compositions, e.g., given by Anders & Grevesse (1989), is estimated to be $\leqslant$2%, but it is substantially less than the uncertainty in SEP charge state. Using the mass and charge state values in Table 3, we consider all combinations of ionic ratios and calculate their S-value. The corresponding values are shown in Table 4.

2.1. 2012 August 31 Event

A filament eruption occurred in the south-eastern region of the solar disk as viewed from Earth on 2012 August 31 (day of year; DOY 244) and launched a CME with linear speed 1442 km s^{-1}.[3] An associated C8 X-ray flare at S16E42 started at 19:45 UT and peaked at 20:43 UT (Gallagher et al. 2002). A shock passed the *STEREO B* spacecraft on September 3 (DOY 247) at 07:11 UT.[4] As viewed from Earth, the flare and the CME were not particularly strong or fast but they caused a significant particle event at *STEREO B* with magnetic

[3] http://cdaw.gsfc.nasa.gov/CME_list/
[4] ftp://stereodata.nascom.nasa.gov/pub/ins_data/impact/level3/STEREO_Level3_Shock.pdf

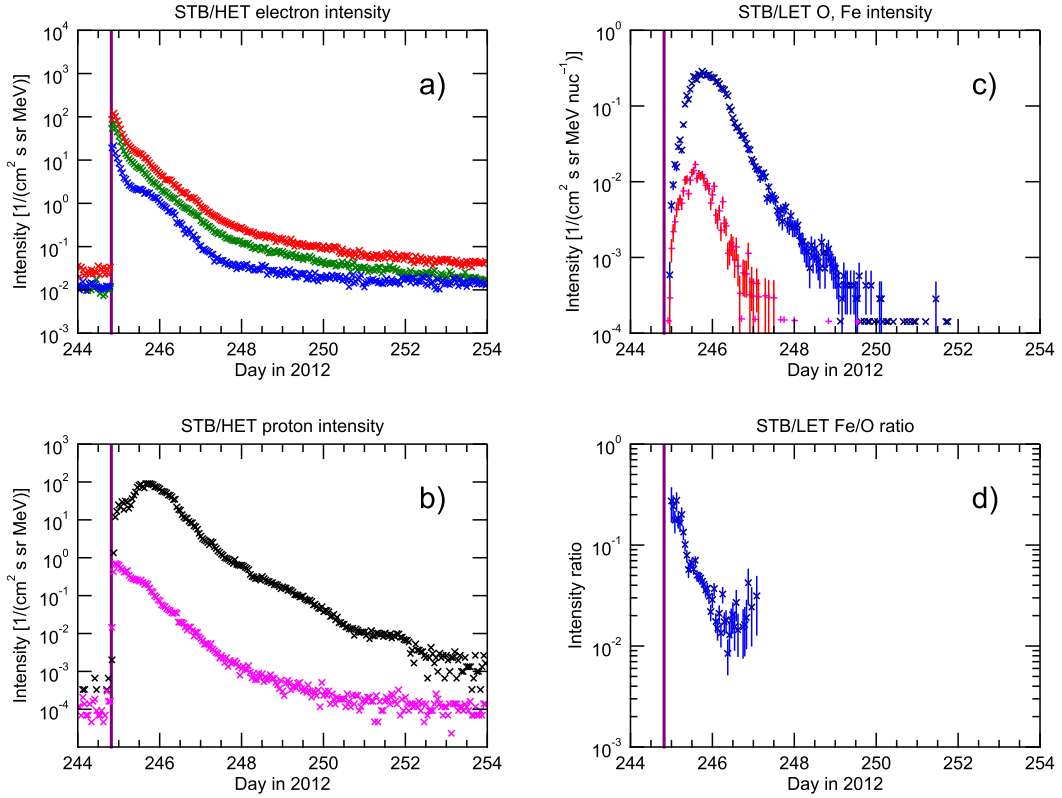

Figure 1. SEP event of 2012 August 31 (event #1): (a) relativistic electron intensity (energy channels: 0.7–1.4 (red), 1.4–2.8 (green), 2.8–4.0 MeV (blue)), (b) proton intensities at high (40–60 MeV, magenta) and low (13.6–15.1 MeV, black) energy, (c) Fe (red) and O (blue) intensity at 4.0–4.5 MeV/nuc, (d) Fe/O intensity ratio. Electron and proton intensities were measured by *STEREO B*/HET, Fe and O intensity by *STEREO B*/LET. The vertical purple line denotes the start time of the flare.

connection $\Delta\phi = -5°$. The event (labeled in the following as event #1) could in many respects be considered an exemplary proton SEP event. Electron, proton, oxygen, and iron particle intensity-time profiles and Fe/O ratio are shown in Figure 1. Both the electron and proton intensity profiles, Figure 1, panels (a) and (b), show a rapid increase followed by a gradual decrease with smooth profile and no significant shock-associated particle intensity component was observed over 10 days. Figures 1(c) and (d) show oxygen and iron intensities, and the Fe/O ratio, respectively. The intensity of oxygen peaks later than that of iron and the oxygen SEP event lasts longer. The Fe/O ratio is decreasing from values typical of impulsive events to values more than 1 order of magnitude below the average gradual event abundance of 0.134 (Reames 1995). This event would be classified as Fe-poor with average Fe/O value over the event $A_{\rm avg}$(Fe/O) = 0.064. The Fe/O decrease occurred over $\Delta t_{\rm Fe/O} = 1.25$ days. After Fe/O reaches its minimum, it increases for the next ~1 day. Considering the intensity profiles of Fe and O, it is apparent that the increase is a result of the low Fe counts at the limit of the instrument's sensitivity.

For the same event, Figure 2 shows a subset of SEP ratios versus time ordered by increasing S values. The graphs show a 4 day period, during which the temporal evolution of heavy ion ratios takes place. From a qualitative point of view, the time variation of the ratio displays a correlation with S: a ratio shows decrease (increase) in time when $S > 1$ ($S < 1$). The ratio profiles also show that the slope of temporal variation scales with S, where, e.g., Mg/O shown in Figure 2(a), a ratio with $S \approx 1$, remains almost unchanged over the duration of the SEP event. The O/C ratio with $S = 1.09$, Figure 2(b), shows a slight but steady decrease over time. The rate of decay of Si/O with $S = 1.11$, Figure 2(c), is higher than that of O/C, but the duration of Si/O evolution is also shorter due to the lower relative abundance of silicon in the SEP event. These ratios show far less variation than the ratios with high values of S, i.e., Fe/Si, Fe/Mg and Fe/C, Figure 2 panels (d), (e) and (f), all of which have larger S. Ratios of elements with respect to hydrogen, e.g., He/H, O/H and Fe/H are somewhat anomalous, showing an initial increase followed by a decrease, as can be seen in the last row of Figure 2 in panels (g), (h) and (i). The decay rate of Fe/H is higher than that of O/H, which is higher than He/H, therefore increasing with increasing S of an SEP ratio. The decay period is shorter for Fe/H than it is for O/H and He/H respectively, due to relative abundances of the elements in the SEP event. The initial increase is observed in all X/H ratios.

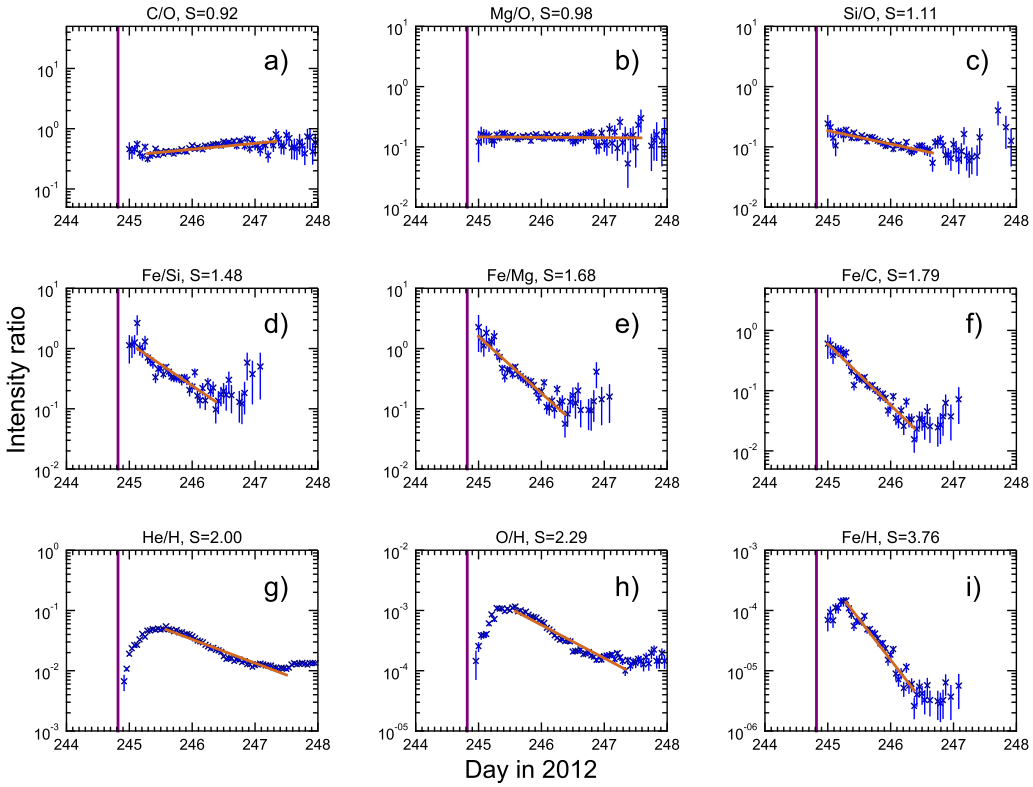

Figure 2. A succession of SEP ratios vs. time with ascending S values (see Table 4) for event #1. SEP ion intensities were measured by *STB*/LET at 4.0–4.5 MeV nuc^{-1}. Ratio data points (blue) in time interval between the maximum and the minimum were fitted to Equation (2) (plotted in brown), where B is the ratio decay time constant. Ratios with larger S show more temporal evolution, i.e., lower B. Ratios X/H increase before they start decreasing. All intervals on the vertical axes are scaled equally to 3 orders of magnitude.

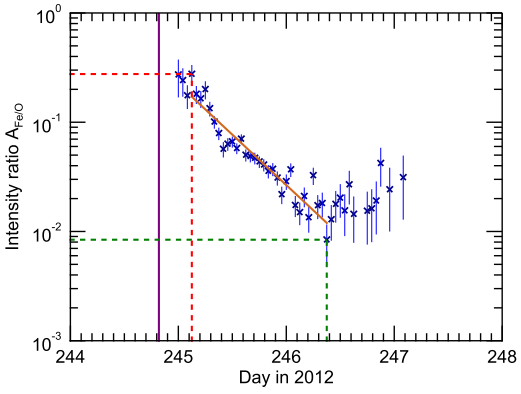

Figure 3. Ratio of Fe/O measured by *STEREO B*/LET at 4.0–4.5 MeV nuc^{-1} with the time of the preceding flare (vertical purple line), maximum (red) and minimum (green). The line of best fit (brown) was fitted to the data in the period between the maximum and minimum.

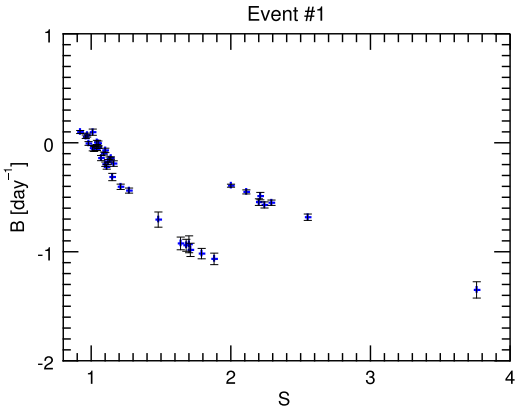

Figure 4. Decay time constants B plotted as a function of S for event #1. The monotonic dependence shows that more decrease is observed in ratios with increasing S. A discontinuity is observed at $S = 2.0$ (He/H).

2.1.1. Quantitative Analysis

We carried out a quantitative analysis of the temporal variation of heavy ion ratios in the SEP events as follows. We indicate A as the heavy ion ratio, calculated as the ratio of two particle intensity values I, e.g., $A_{Fe/O} = I_{Fe}/I_O$. As an example, Figure 3 shows the Fe/O ratio in event #1 at

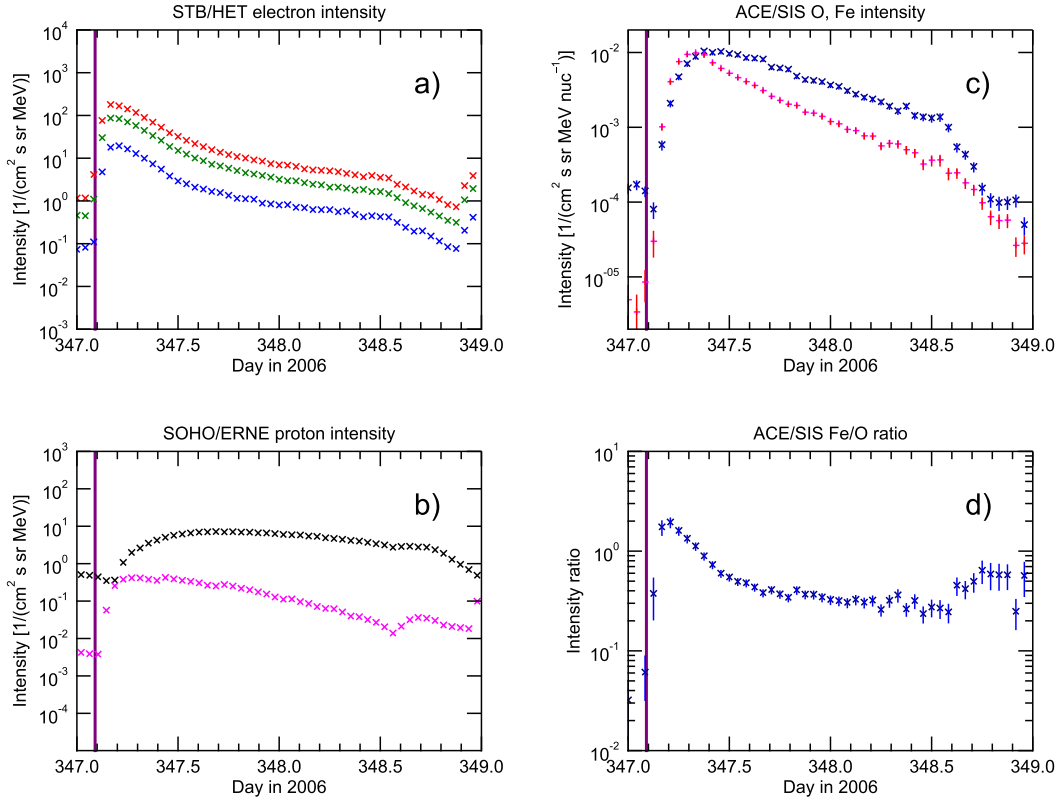

Figure 5. SEP event 2006 December 13 (event #2): (a) relativistic electron intensity (energy channels: 0.7–1.4 (red), 1.4–2.8 (green), 2.8–4.0 MeV (blue)), (b) proton intensities at high (40.5–62.2 MeV, magenta) and low (13.8–14.6 MeV, black) energy, (c) Fe (10.7–15.8 MeV nuc^{-1}, red) and O (10.0–13.1 MeV nuc^{-1}, blue) intensity, (d) Fe/O intensity ratio. Electron intensities were measured by *STEREO B*/HET, proton intensities by *SOHO*/ERNE, Fe and O intensity by *ACE*/SIS. The vertical purple line denotes the start time of the flare.

4.0–4.5 MeV nuc^{-1} over a 4 day period. Ratio data points used in further analysis are those that have more than 2 particle counts in a 1 hr time bin for both ion species. An input to the analysis is the time range Δt from the start of the flare over which data should be fitted. We marked the first occurring maximum or minimum data point within Δt as A_1, and the last occurring as A_2. When the Fe/O ratio decreases over time, the maximum precedes the minimum and $A_2/A_1 < 1$, but other heavy ion ratios may show an increase over time, i.e., $A_2/A_1 > 1$. All the data points between the maximum and the minimum were fitted using the function

$$A = 10^{\alpha + Bt} \quad (2)$$

where B is the ratio decay time constant in units of day^{-1}, and α is a unitless fitting constant. For the example of Figure 3, the decay time constant, obtained using Equation (2), is $B_{\mathrm{Fe/O}} = (-0.92 \pm 0.06)$ day^{-1}. In a similar manner, the values of B were obtained for all abundant ratios considered in Table 4.

In Figure 4 we plot the decay time constant B as a function of S for all SEP ratios in event #1. The plot shows a quantitative description of the qualitative behavior seen in Figure 2. Between $S = 1$ and $S = 2$ a monotonic decrease of B with S is observed corresponding to faster decay rates as S increases. There is a discontinuity present at $S = 2.0$, the S value for He/H, followed by another monotonic decrease. As can be seen from Table 4, the ratios with $S \geqslant 2$ are ratios of a heavy ion and hydrogen, X/H.

The location of the data points along the horizontal axis is influenced by the values of the charge states Q that are used to calculate S. We analyzed how S values change when different values of Q_{Fe}, the Q value that can vary by the largest amount, are considered. The S value for Fe/O in our plot is $S = 1.64$. This value changes to $S = 2.04$ when $Q_{\mathrm{Fe}} = 12$ and $S = 1.36$ when $Q_{\mathrm{Fe}} = 18$. If the Fe charge changes, ionic charges for all the other ions would change too, therefore it is not easy to quantify the effect on the B versus S plot unless charge states for the event for all ions were available.

2.2. 2006 December 13 Event

Next we considered the event on 2006 December 13 (DOY 347, event #2), which shows similar heavy ion profiles to event #1. Event #2 was caused by an X3.4 flare at S05W23, which started at 02:14 UT and peaked at 02:40 UT. The flare was accompanied by a CME with speed 1774 km s^{-1} and an interplanetary shock passed *ACE* on December 14th (DOY

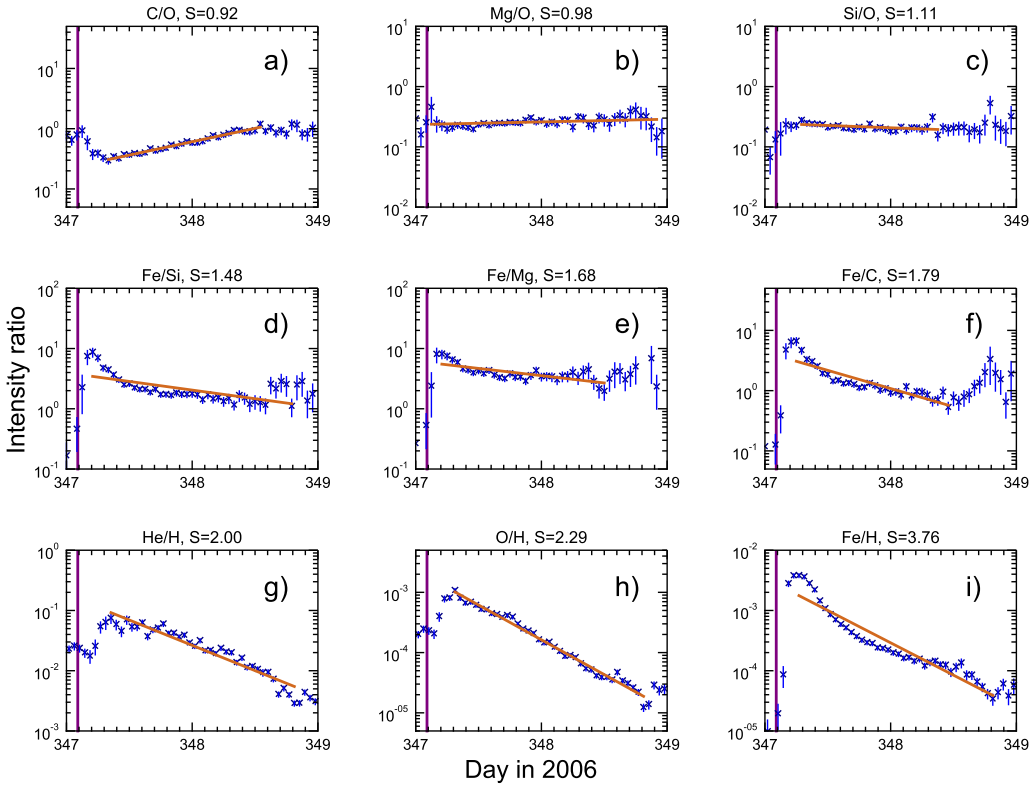

Figure 6. A succession of SEP ratios with ascending S values (see Table 4) for event #2. Proton intensities were measured by *SOHO*/ERNE and heavy ion intensities by *ACE*/SIS. Energy channels for a pair of ions in each ratio, which were selected to be the closest match, are the following: C/O–C 6.4—8.6 MeV nuc^{-1}, O 7.3–10.0 MeV/nuc; Mg/O–Mg 8.7–12.2 MeV nuc^{-1}, O 10.0–13.1 MeV nuc^{-1}; Si/O–Si 9.2–13.0 MeV nuc^{-1}, O 10.0–13.1 MeV nuc^{-1}; Fe/Si–Fe 10.7–15.8 MeV nuc^{-1}, Si 9.2–13.0 MeV nuc^{-1}; Fe/Mg 10.7–15.8 MeV nuc^{-1}, Mg 12.2–16.0 MeV nuc^{-1}; Fe/C–Fe 10.7–15.8 MeV nuc^{-1}, C 11.2–13.4 MeV nuc^{-1}; He/H–He 3.4–4.7 MeV nuc^{-1}, H 3.5–4.1 MeV; O/H 7.3–10.0 MeV nuc^{-1}, H 8.1–10.1 MeV; Fe/H–Fe 10.7–15.8 MeV nuc^{-1}, H 13.8–14.6 MeV.

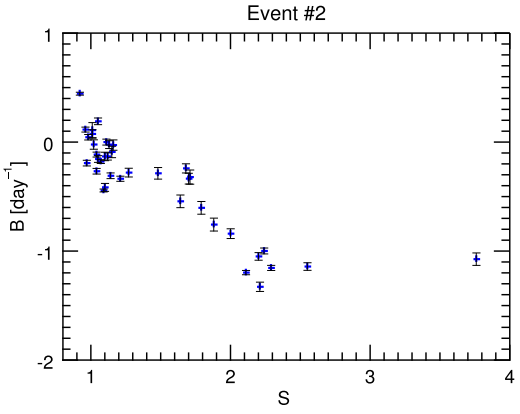

Figure 7. Decay time B plotted as a function of S for event #2. The monotonic dependence as in event #1 is observed but without the discontinuity.

348) at 14:14 UT. The event was studied in detail by Liu et al. (2008) and von Rosenvinge et al. (2009). Particle intensity profiles for event #2 are shown in Figure 5. Event #2 was followed by another SEP event on December 14 at 22:14 UT, therefore the analyzed period was cut off on 2006 December 15 (DOY 349). The SEP event occurred while the particle intensity was elevated from a preceding event, see Figure 5(b), but the proton intensity increase due to event #2 was several orders of magnitude. The pre-event background for heavy ions was less significant than for protons because heavy ion events decay faster. We use the heavy ion data from *ACE* because the *STEREO* spacecraft were still performing manoeuvres near the Earth (von Rosenvinge et al. 2009). At the time of the flare, the magnetic connection of *ACE* was $\Delta\phi = -17°$. The Fe/O ratio, Figure 5(d), decreases for $\Delta t_{\mathrm{Fe/O}} = 1.25$ days. Fe/O decays to a value of about 2×10^{-1}, higher than the value reached in event #1. This event is Fe-rich with average Fe/O value $A_{\mathrm{avg}}(\mathrm{Fe/O}) = 0.540$. Figure 6 shows a subset of heavy ion ratios as in Figure 2. The ratios show similar temporal evolution to that observed in event #1, except for the initial increases observed in most heavy ion ratio time profiles, which may be the result of the elevated background from the preceding event.

We applied the quantitative analysis to the SEP ratios as in event #1 and plotted the function B versus S as shown in Figure 7. The dependence shows a monotonic behavior but in this case the discontinuity at $S = 2.0$ is not present. Instead, the

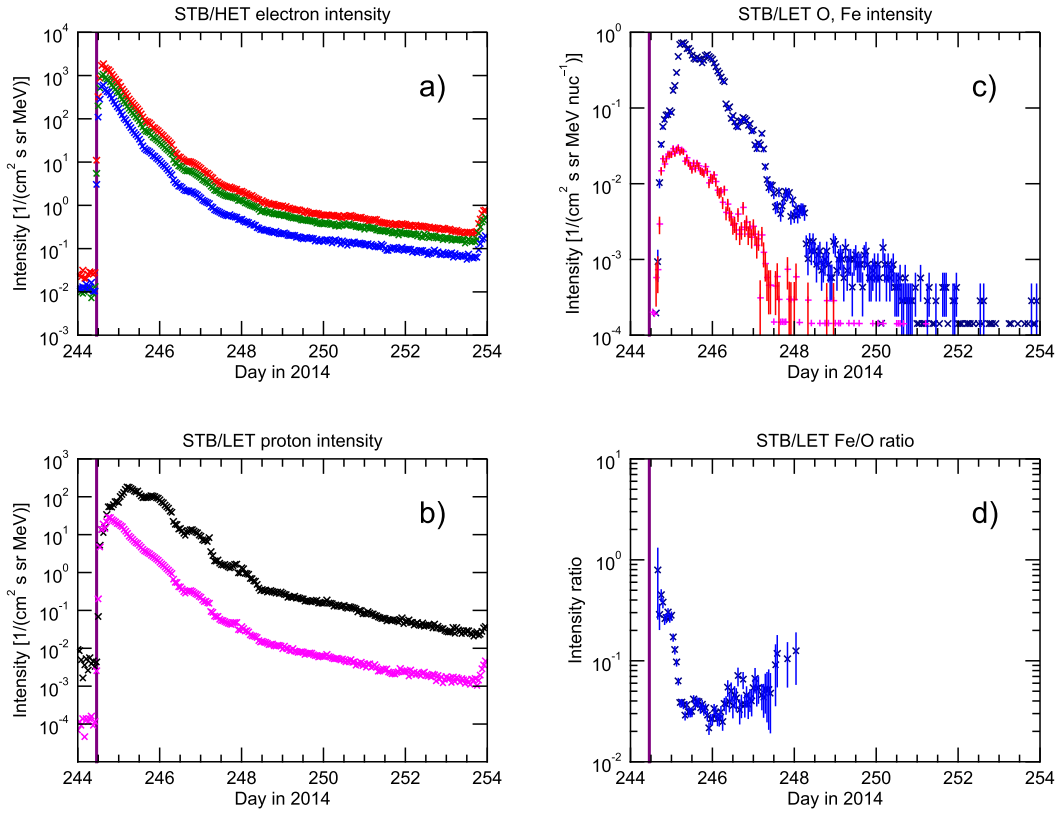

Figure 8. SEP event 2014 September 1 (event #3): (a) relativistic electron intensity (energy channels: 0.7–1.4 (red), 1.4–2.8 (green), 2.8–4.0 MeV (blue)), (b) proton intensities at high (40–60 MeV, magenta) and low (13.6–15.1 MeV, black) energy, (c) Fe (red) and O (blue) intensity at 4.0–4.5 MeV nuc^{-1}, (d) Fe/O intensity ratio. Electron and proton intensities were measured by *STEREO B*/HET, Fe and O intensity by *STEREO B*/LET. The vertical purple line denotes the start time of the flare.

X/H ratios decay at a faster rate than other heavy ion ratios. This behavior is observed because the proton intensity at these energies only changes by ≈1 order of magnitude over the 2 day period (see proton intensity at 13.8–14.6 MeV in Figure 5(b)).

2.3. 2014 September 1 Event

Event #3 originated from an active region behind the eastern limb of the Sun as viewed from Earth on 2014 September 1 (DOY 244) at 11:00 UT. We determined the location of the flare at N14E129 using FITS data from the *STEREO B* EUVI instrument. Pesce-Rollins et al. (2015) estimated the flare class as X2.1, located at N14E126. The associated CME had a speed of 1901 km s^{-1}. *STEREO B*, which was the best magnetically connected spacecraft ($\Delta\phi = -25°$), encountered a passing shock on September 3 (DOY 246) at 07:45 UT.[5] The particle intensity profiles are shown in Figure 8. A sudden increase in the oxygen particle intensity of ≈1 order of magnitude (Figure 8(c), blue) was observed ∼13 hr after the flare started, which is not present in the iron particle intensity (red). This increase in oxygen occurred more than a day before the shock passed the spacecraft. The Fe/O ratio dropped rapidly due to the increase in oxygen intensity and reached its minimum $\Delta t = 1.25$ days after the maximum. The event-averaged Fe/O value is $A_{\rm avg}$(Fe/O) = 0.089. Figure 9 shows a subset of heavy ion ratios. Many heavy ion ratios, including Fe/Si, Fe/Mg, Fe/C and Si/O, show a rapid drop in ratio value followed by a plateau, a similar to the Fe/O time. Apart from the sudden drop, the ratios in event #3 show qualitatively similar behavior to events #1 and #2 in the ordering of the decreases (increases) by *S*.

We applied the quantitative analysis to the SEP ratios as in event #1. The values of decay time constant *B* obtained by fitting in this event largely depend on the length of the interval Δt, where the data points are fitted. For example, *B* values obtained in two ratios Fe/Si and Fe/Mg (Figures 9(d) and (e)) are $B_{\rm Fe/Si} = (-0.19 \pm 0.03)$ day^{-1} and $B_{\rm Fe/Mg} = (-0.89 \pm 0.09)$ day^{-1} but the corresponding fitting interval for Fe/Si ($\Delta t_{\rm Fe/Si} = 2.63$ day) is more than twice as long as it is for Fe/Mg ($\Delta t_{\rm Fe/Mg} = 1.17$ day). Such differences can be seen in O/H and Fe/H ratios in Figure 9 panels (h) and (i). We plotted *B* versus *S*, shown in Figure 10, and the data point at $S = 1.48$ corresponding to Fe/Si deviates from the otherwise monotonic dependence in $S \in [0.9, 2.0)$. Nevertheless, the obtained dependence qualitatively resembles the *B* versus *S* dependence in event #1 (Figure 4).

[5] ftp://stereodata.nascom.nasa.gov/pub/ins_data/impact/level3/STEREO_Level3_Shock.pdf

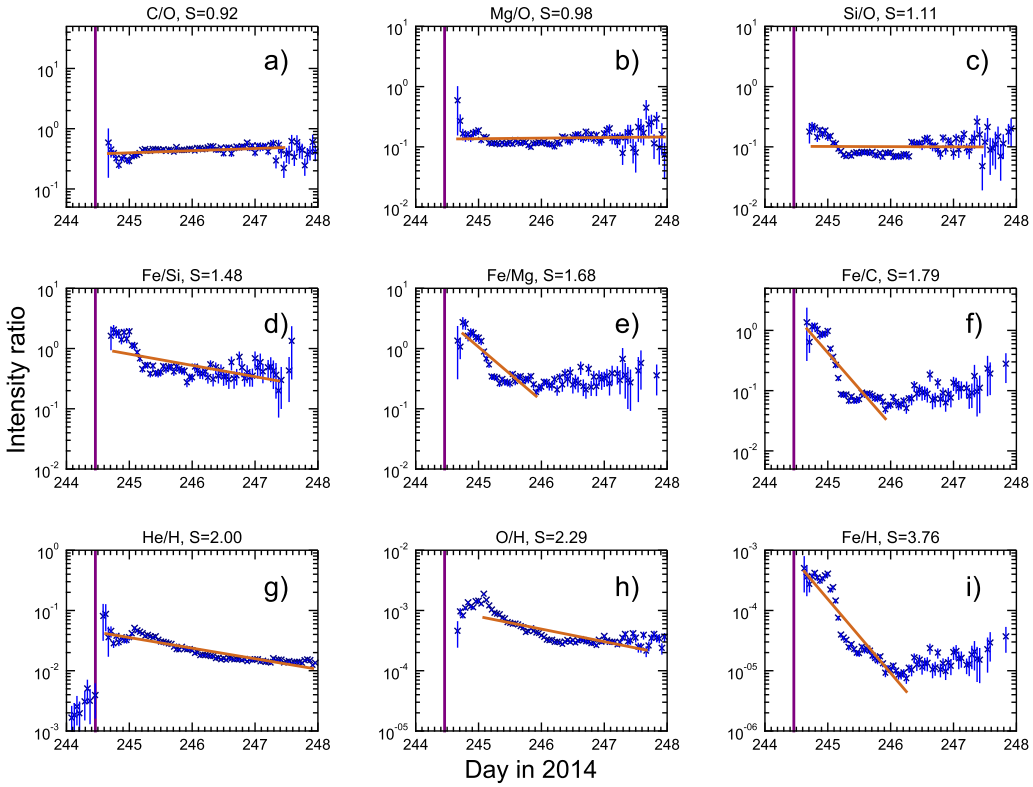

Figure 9. A succession of SEP ratios with ascending S values (see Table 4) for event #3. As in Figure 2, the SEP ion intensities were measured by STB/LET at 4.0–4.5 MeV nuc^{-1}. The SEP ratio data (blue) are overplotted with the fitted function (brown).

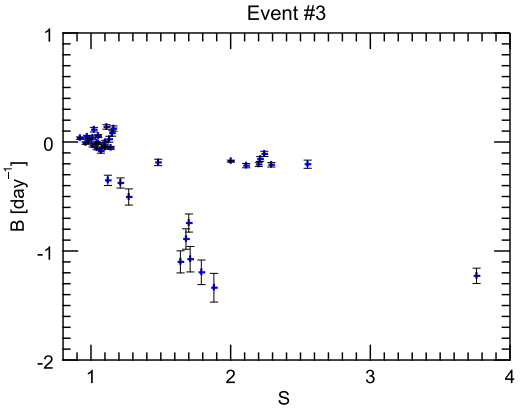

Figure 10. Decay time B plotted as a function of S for event #3. The dependence is qualitatively very similar to event #1.

2.4. 2014 February 25 Event

SEP event #4, which occurred on 2014 February 25 (DOY 56), was caused by an X4.9 flare that erupted at S12E77 and it was accompanied by an exceptionally fast CME with a speed of 2147 km s^{-1}. *STEREO B* was the best magnetically connected spacecraft with the magnetic footpoint separated from the flare by $\Delta\phi = 32°$. Figure 11 shows intensity profiles for the event at *STEREO B*. Fe and O intensities were also detected by *ACE* and *STEREO A* but these spacecraft were not magnetically well connected (Zelina et al. 2015). As can be seen in Figure 11(d), the SEP event at *STEREO B* shows the Fe/O ratio decreased for $\Delta t = 2.75$ days but a significant decrease occurred during the first ~12 hr followed by Fe/O remaining relatively unchanged for the rest of the event. This event is Fe-rich with average Fe/O value $A_{\rm avg}$(Fe/O) = 0.212. Heavy ion ratios of event #4 are shown in Figure 12. Similarly to the Fe/O ratio, other heavy ion ratios also show little variation over time after ≈1 day.

The quantitative analysis was applied to the SEP data in event #4 in two ways: first the fitting procedure was applied to the entire event (i.e., over a time range $\Delta t = 4$ days), second it was applied only to the first 12 hr after the start of the flare. The first 12 hr are when a fast decrease (increase) occurs in some ratios. The graphs of B versus S dependence for the two Δt values are shown in Figure 13. The B versus S graph for $\Delta t = 4$ days (Figure 13(a)), shows that the decay time constants are smaller because the initial decrease in Fe/X ratios is averaged over a longer period, over which the ratios remain relatively unchanged. A discontinuity can hardly be observed due to small B values of the ratios. As can be seen in

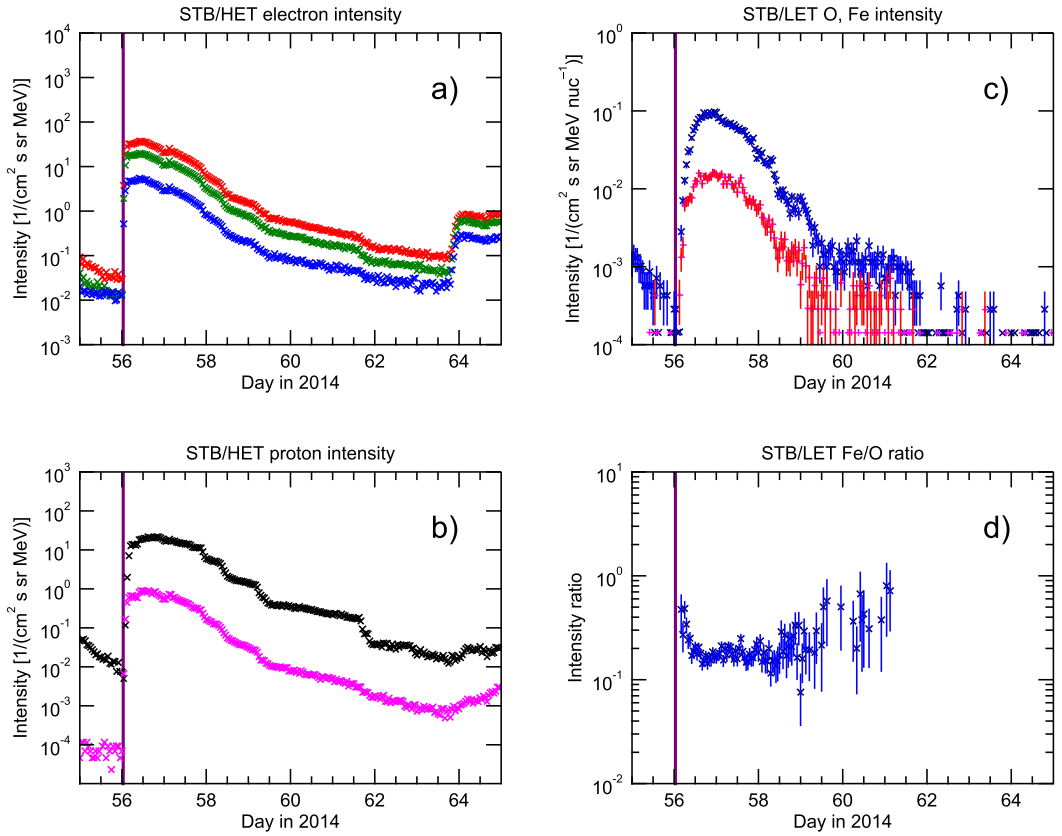

Figure 11. SEP event 2014 February 25 (event #4): (a) relativistic electron intensity (energy channels: 0.7–1.4 (red), 1.4–2.8 (green), 2.8–4.0 MeV (blue)), (b) proton intensities at high (40–60 MeV, magenta) and low (13.6–15.1 MeV, black) energy, (c) Fe (red) and O (blue) intensity at 4.0–4.5 MeV nuc^{-1}, (d) Fe/O intensity ratio. Electron and proton intensities were measured by *STEREO B*/HET, Fe and O intensity by *STEREO B*/LET. The vertical purple line denotes the start time of the flare.

Figure 12(b), when the fit is carried out over 12 hr, the obtained B values are larger in magnitude than in the previous events. In the latter plot, a discontinuity at $S = 2.0$ is observed, as in Figure 4.

3. DISCUSSION

We have studied SEP intensities and elemental ratios in four SEP events, where Fe/O has been observed to decrease over time, in the ≈4–15 MeV/nuc energy range. We used 1 hr averaged SEP data from energetic particle telescopes onboard *ACE*, *SOHO*, and *STEREO B*, and systematically quantified the temporal dependence of abundant SEP ratios. Each of the SEP events was observed by a well-connected spacecraft with a magnetic footpoint within 32° of the flare.

We observed that time evolution of heavy ion ratios is a common feature present in all four analyzed SEP events, with the largest variation in Fe/X ratios, where X indicates an abundant SEP element. We found that some abundance ratios, e.g., Mg/O, remained relatively unchanged during an SEP event, and some ratios, e.g., Ne/O, even showed an increase over time. This behavior is ordered by the S value of an SEP ratio, defined as the ratio of M/Q values of the two SEP species in the ratio. Ratios with $S < 1$ ($S > 1$) exhibit an increase (decrease) over time. We also observed that the slope of a ratio tends to be steeper for ratios with larger S value. Therefore, the temporal evolution of SEP heavy ion ratios shows ordering by M/Q.

We quantitatively examined the ratios listed in Table 4 for the 4 SEP events, and for each event we plotted the values of decay time constant B as a function of S. Each of the obtained plots, Figures 4, 7, 10 and 13, shows a monotonic dependence of B versus S in the range $S \in [0.9, 2.0)$. The B versus S dependence in three out of four events, (including Figure 13(b)), shows a discontinuity at $S = 2.0$ that corresponds to He/H. In event #2 (Figure 7) the discontinuity at $S = 2.0$ is not present, probably because the proton intensity, shown in Figure 5(b), only varies by ∼1 order of magnitude during the analyzed period and does not decay significantly. As a result, the X/H ratios in event #2 decay at a much faster rate than in the other events. Event #3 showed B versus S dependence that is qualitatively similar to event #1. The discontinuity was not observed in event #4 (Figure 13(a)), where $\Delta t = 4$ days was much longer that the period of significant temporal variation, i.e., the first ∼12 hr after the start of the flare. The B values obtained by fitting in the two time

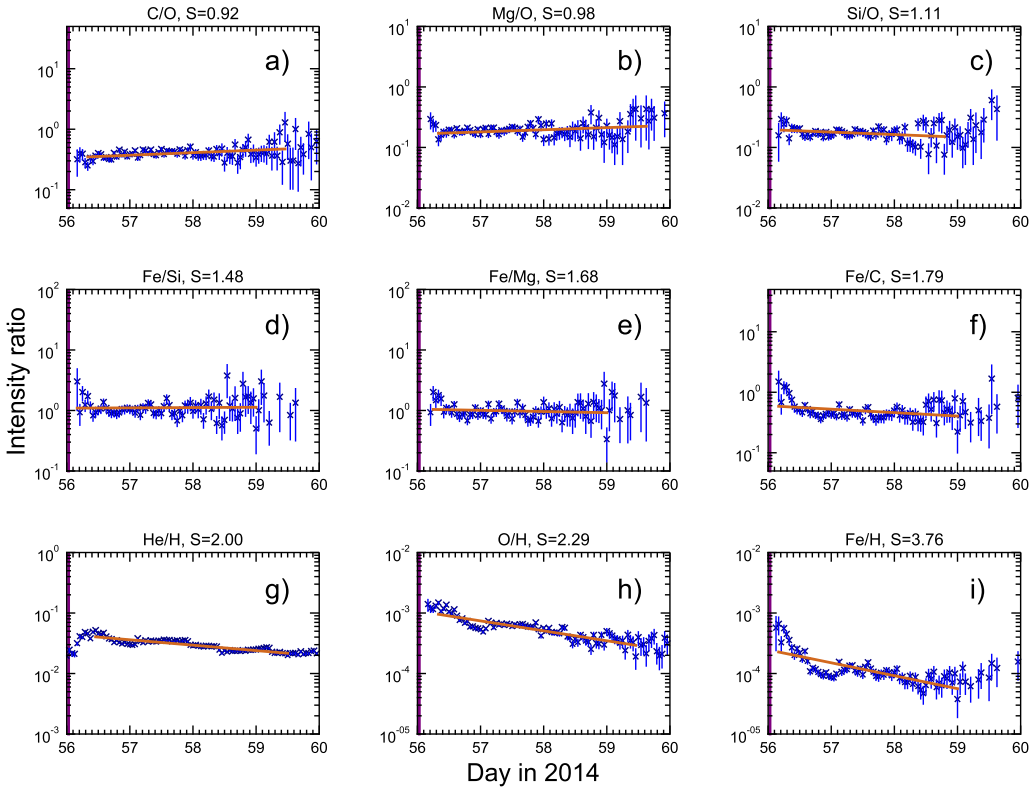

Figure 12. A succession of SEP ratios with ascending S values (see Table 4) for event #4. As in Figure 2, the SEP ion intensities were measured by STB/LET at 4.0–4.5 MeV nuc^{-1}. The SEP ratio data (blue) are overplotted with the fitted function (brown). Much of the temporal variation is observed during the first day of the event.

intervals, $\Delta t = 4$ days and 12 hr in event #4, showed ordering by M/Q.

When plotted on a logarithmic–linear plot, intensity ratio time data often exhibit time profiles similar to a linear function between their maximum and minimum values. Every SEP ratio had a minimum and a maximum identified independently. The method of finding the maximum and the minimum of a ratio time profile affected the value of the fitted decay constant B, where ratios fitted over a longer time interval showed less average temporal variation, in particular the Fe/Si ratio in event #3 and most of the ratios in event #4. This is clearly a limitation of the used method; nevertheless, it allowed us to characterize and quantify the observed temporal evolution in SEP ratio time profiles.

Some events have a more complex structure than the monotonic intensity decrease shown for example by event #1. More complicated intensity profiles, from which the ratio profiles are derived, can be caused by interplanetary structures affecting the propagation of ions, multiple events, or shocks. This makes the choice of the fit interval Δt more challenging and different ionic ratios might require different Δt values in a single event (see, e.g., event #3).

The temporal evolution of heavy ion ratios has previously been interpreted as a signature of a rigidity-dependent acceleration (Tylka et al. 1999). In this model, the decrease in the Fe/O ratio would be caused by Fe ions with large M/Q spending less time at the shock during acceleration and being released earlier than O ions.

However, Mason et al. (2006) presented data on Fe and O intensity profiles at two energy ranges, where they showed that the decrease of Fe/O over time is likely a result of SEP propagation through the interplanetary medium, in common with other authors (e.g., Scholer et al. 1978; Mason et al. 2012; Tylka et al. 2013). In 1D propagation, the scattering mean free path λ is assumed to depend on M/Q of an SEP ion, e.g., $\lambda_{Fe} > \lambda_O$. The stronger scattering causes a slower propagation of an ion with lower M/Q values to the observer, which can result in temporal dependence of a ratio profile such as ratios observed in this study.

In a recent study, Dalla et al. (2016) carried out 3D full-orbit test particle simulations of SEP propagation in a unipolar Parker spiral magnetic field. Fe and O ions injected near the Sun were allowed to propagate in 3D with a rigidity independent scattering mean free path $\lambda = 1$ au. Their crossings of the 1 au sphere were counted as a function of time for observers at various locations with respect to the source. The particles experienced strong curvature and gradient drifts (Dalla et al. 2013) which caused transport in a direction perpendicular to the magnetic field, with drift velocities proportional to M/Q. For particles at equal energy/nucleon, the ion with larger

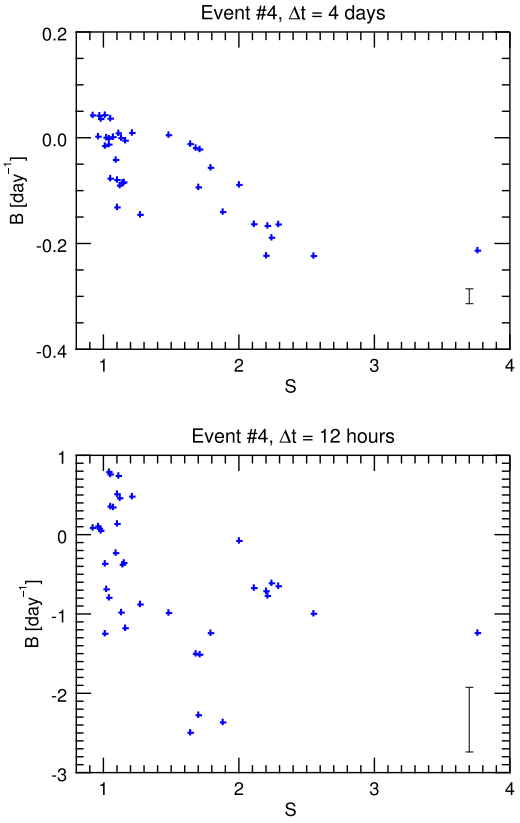

Figure 13. Decay time B plotted as a function of S for event #4. The top panel shows the results of fits using $\Delta t = 4$ days, the bottom one using $\Delta t = 12$ hr. Note the different scaling of the ordinate. A typical size of error bars ($\pm 1\sigma$) is shown in the right bottom corner of the graphs.

M/Q propagated across the magnetic field more easily and was able to reach the detector earlier. The calculated Fe/O time profiles from the simulations were qualitatively similar to the observations in events #1–3. Therefore, drift as an SEP transport mechanism in 3D could explain the observed temporal variation of heavy ion ratios. In this model, the simulation with the value of mean free path $\lambda = 0.1$ au produced similar results to the case with $\lambda = 1$ au. Comparing the results corresponding to the two values of λ, the variation of the mean free path had little effect on the final Fe/O ratio time profiles.

Several ionic ratios in our figures show an increase toward the end of the SEP event, e.g., Fe/O in Figure 1 and Fe/Si, Fe/C and Fe/H in Figure 2. This kind of behavior can also be seen in Figure 5 in Tylka et al. (2013), Figure 2 in Zelina et al. (2015) and Figure 3 in Reames (1990). Such an effect could be in some cases a result of low count statistics, however, for some events it does appear to be a real effect, e.g., events #1 and #4 (Figures 1 and 11(d)). Simulations by Dalla et al. (2016) show a similar behavior in the Fe/O time profiles. In that model the increase late in the event results from O decaying at a faster rate than Fe since O occupied a narrower longitudinal extent than Fe, due to a smaller drift. The increases could be caused by passing magnetic structures, e.g., shocks and interplanetary coronal mass ejections, within which the particle populations, magnetic field vectors, and transport conditions may be different from the surrounding environment. In event #2, after passing of the shock on 2006 December 14 at 14:14 UT (Figure 5(c)), the O intensity suddenly starts decreasing at a faster rate than Fe, and the Fe/O value increases as the result. The Fe intensity profile in event #3 (Figure 8(c)) has a smooth intensity profile but O intensity in the same event has a more complicated intensity profile with sharp rises and decreases. As a result, the Fe/O ratio (Figure 8(d)) also has a complicated time profile with increases and decreases.

In an analysis of time profiles of heavy ion ratios, Mason et al. (2012) noted that the He/H ratio showed a decrease only in some of the 17 SEP events, while it did not decrease in others. They concluded that the temporal behavior of protons was different from heavy ion elements. In our analysis, we found that the time profiles of X/H ratios were anomalous compared to other ratios, often showing an increase of the ratio values before the decrease. The decreases in time occurred at a lower rate compared with other heavy ion ratios, which resulted in a discontinuity observed in B versus S plots.

Anomalous time profiles of X/H ratios can emerge in a number of scenarios. The ratios could be signatures of differences in SEP acceleration or interplanetary transport between protons and heavier ions. On the other hand, they could be a result of the much higher abundance of protons in the SEP population. At present, the origin of the anomalous nature of X/H time profiles and their slower decay over time remains unknown, and any theory should be able to explain temporal evolution of heavy ion as well as X/H ratios.

The B versus S profiles depend on our assumption of used charge state values. Obtaining values of SEP charge states is challenging and this type of measurement is not routinely carried out for all SEP events. In our analysis, we used charge state values averaged over a number of events by Luhn et al. (1985) that have been used previously in similar studies. While these measurements should be representative of typical ionic charge state values, charge states of an SEP ion are known to have different values in separate particle events (e.g., $Q_{\rm Fe} \approx 10$–20) and can depend on the kinetic energy (Klecker et al. 2006). If event-specific values of Q were used, S-values in Table 4 would be modified and this would result in a shift of the data points horizontally in the B versus S plots (Figures 4, 7, 10 and 13).

4. CONCLUSIONS

In this study, we used SEP data from *ACE*/SIS, *SOHO*/ERNE and *STEREO*/LET and *STEREO*/HET to quantitatively characterize the temporal evolution of SEP ratios. Our main results are as follows:

1. The temporal evolution of heavy ion ratios is ordered by the ratio of mass-to-charge values of the two SEP ions, S.
2. Between $S = 0.9$ and $S = 2.0$, considering 28 different ionic ratios, we find a clear monotonic behavior with S, with slopes of B versus S typically given by -0.5 day^{-1} for event #2, to -1.5 day^{-1} for event #3.
3. Ratios of heavy ion to hydrogen, X/H, where X is an abundant SEP element, corresponding to $S \geqslant 2.0$, often show an increase before the decrease in their time profiles and decay at slower rates. This anomaly is present in the

B versus S plots as a discontinuity where the B values jump to a significantly higher value than would be predicted by a monotonic B versus S dependence.

Our analysis and previously reported observations of heavy ion SEP data suggest that the temporal variation of heavy ion ratios is a common feature of SEP events. This phenomenon has been observed at various instances in the ecliptic (e.g., Tylka et al. 1999; Mason et al. 2012; Zelina et al. 2015) and at high heliographic latitudes (Tylka et al. 2013).

In recent years, a consensus has emerged that the time evolution of Fe/O and other ionic ratios is an interplanetary transport effect (Mason et al. 2006; Tylka et al. 2013). At the present time, both 1D rigidity dependent scattering ($\lambda \propto (M/Q)^{\alpha}$, e.g., Mason et al. 2012) and 3D drift associated transport (drift velocity $\propto M/Q$, Dalla et al. 2016) are possible mechanisms that may explain our observations.

We thank the instrument teams of *ACE*/SIS, *STEREO*/LET, *STEREO*/HET and *SOHO*/ERNE for providing Level 2 data, made publicly available through *ACE* and *STEREO* Science Centers, and the Space Research Laboratory at the University of Turku. P.Z. acknowledges support from the JHI at the University of Central Lancashire through a PhD studentship. S.D. acknowledges support from the UK Science and Technology Facilities Council (STFC) (grant ST/M00760X/1) and the Leverhulme Trust (grant RPG-2015-094). The work at Caltech was supported by the National Science Foundation grant NSF-1156004, NASA grants NNX13A66G and subcontract 00008864 of NNX15AG09G.

Facilities: ACE, *GOES*, *SOHO*, *STEREO*.

REFERENCES

Anders, E., & Grevesse, N. 1989, GeCoA, 53, 197
Cane, H. V., von Rosenvinge, T. T., Cohen, C. M. S., & Mewaldt, R. A. 2003, GeoRL, 30, 8017
Cohen, C. M. S., Mason, G. M., Mewaldt, R. A., & Wiedenbeck, M. E. 2014, ApJ, 793, 35
Dalla, S., Balogh, A., Krucker, S., et al. 2003, GeoRL, 30, 8035
Dalla, S., Marsh, M., Kelly, J., & Laitinen, T. 2013, JGRA, 118, 5979
Dalla, S., Marsh, M., Zelina, P., & Laitinen, T. 2015, in 34th Int. Cosmic Ray Conf., ed. A. M. van den Berg et al., 213
Dalla, S., Marsh, M., Zelina, P., & Laitinen, T. 2016, A&A, submitted (arXiv:1606.05612) doi:10.1051/0004-6361/201628618
Dresing, N., Gómez-Herrero, R., Heber, B., et al. 2014, A&A, 567, A27
Dresing, N., Gómez-Herrero, R., Klassen, A., et al. 2012, SoPh, 281, 281
Gallagher, P. T., Moon, Y., & Wang, H. 2002, SoPh, 209, 171
Gómez-Herrero, R., Dresing, N., Klassen, A., et al. 2015, ApJ, 799, 55
Klecker, B., Möbius, E., & Popecki, M. 2006, SSRv, 124, 289
Labrador, A. W., Leske, R. A., Mewaldt, R. A., Stone, E. C., & von Rosenvinge, T. T. 2005, in 29th Int. Cosmic Ray Conf., ed. B. Sripathi Acharya et al., 99
Lario, D., Aran, A., Gómez-Herrero, R., et al. 2013, ApJ, 767, 41
Liu, Y., Luhmann, J. G., Müller-Mellin, R., et al. 2008, ApJ, 689, 563
Luhn, A., Hoverstadt, D., Klecker, B., et al. 1985, 19th Int. Cosmic Ray Conf. (Hampton, VA: STI), 241
Marsh, M. S., Dalla, S., Kelly, J., & Laitinen, T. 2013, ApJ, 774, 4
Mason, G. M., Desai, M. I., Cohen, C. M. S., et al. 2006, ApJL, 647, L65
Mason, G. M., Li, G., Cohen, C. M. S., et al. 2012, ApJ, 761, 104
Mewaldt, R., Cohen, C., Cook, W., et al. 2008, SSRv, 136, 285
Mewaldt, R. A., Cohen, C. M. S., & Mason, G. M. 2006, in The Source Material for Large Solar Energetic Particle Events, Vol. 165 ed. R. M. Natchimuthukonar Gopalswamy & J. Torsti (Washington, DC: American Geophysical Union), 115
Oetliker, M., Klecker, B., Hovestadt, D., et al. 1997, ApJ, 477, 495
Pesce-Rollins, M., Omodei, N., Petrosian, V., et al. 2015, in 34th Int. Cosmic Ray Conf., ed. A. M. van den Berg et al., 128
Reames, D. 1990, ApJL, 358, L63
Reames, D. 1995, AdSpR, 15, 41
Reames, D. V. 1999, SSRv, 90, 413
Richardson, I., von Rosenvinge, T., Cane, H., et al. 2014, SoPh, 289, 3059
Scholer, M., Hovestadt, D., Klecker, B., Gloeckler, G., & Fan, C. Y. 1978, JGR, 83, 3349
Stone, E., Cohen, C., Cook, W., et al. 1998, SSRv, 86, 357
Torsti, J., Valtonen, E., Lumme, M., et al. 1995, SoPh, 162, 505
Tylka, A. J., Malandraki, O. E., Dorrian, G., et al. 2013, SoPh, 285, 251
Tylka, A. J., Reames, D. V., & Ng, C. K. 1999, GeoRL, 26, 2141
von Rosenvinge, T., Reames, D., Baker, R., et al. 2008, SSRv, 136, 391
von Rosenvinge, T., Richardson, I., Reames, D., et al. 2009, SoPh, 256, 443
Wiedenbeck, M. E., Mason, G. M., Cohen, C. M. S., et al. 2013, ApJ, 762, 54
Zelina, P., Dalla, S., & Laitinen, T. 2015, in 34th Int. Cosmic Ray Conf., ed. A. M. van den Berg et al., 055

Appendix C

Appendix C includes a copy of Dalla et al. (2017b): Dalla, S., Marsh, M. S., Zelina, P., & Laitinen, T. 2017. "Time dependence of Fe/O ratio within a 3D solar energetic particle propagation model including drift." *Astronomy & Astrophysics*, Vol. 598, pp. A73 (6 pages).

A&A 598, A73 (2017)
DOI: 10.1051/0004-6361/201628618

Astronomy & Astrophysics

Time dependence of Fe/O ratio within a 3D solar energetic particle propagation model including drift

S. Dalla[1], M. S. Marsh[2], P. Zelina[1], and T. Laitinen[1]

[1] Jeremiah Horrocks Institute, University of Central Lancashire, Preston, PR1 2HE, UK
e-mail: sdalla@uclan.ac.uk
[2] Met Office, Exeter, EX1 3PB, UK

Received 31 March 2016 / Accepted 3 November 2016

ABSTRACT

Context. The intensity profiles of iron and oxygen in Solar Energetic Particle (SEP) events often display differences that result in a decreasing Fe/O ratio over time. The physical mechanisms behind this behaviour are not fully understood, but these observational signatures provide important tests of physical modelling efforts.
Aims. In this paper we study the propagation of iron and oxygen SEP ions using a 3D model of propagation which includes the effect of guiding centre drift in a Parker spiral magnetic field. We derive time intensity profiles for a variety of observer locations and study the temporal evolution of the Fe/O ratio.
Methods. We use a 3D full orbit test particle model which includes scattering. The configuration of the interplanetary magnetic field is a unipolar Parker spiral. Particles are released instantaneously from a compact region at two solar radii and allowed to propagate in 3D.
Results. Both Fe and O experience significant transport across the magnetic field due to gradient and curvature drifts. We find that Fe ions drift more than O ions due to their larger mass-to-charge ratio, so that an observer that is not magnetically well connected to the source region will observe Fe arriving before O, for particles within the same range in energy per nucleon. As a result, for the majority of observer locations, the Fe/O ratio displays a decrease in time.
Conclusions. We conclude that propagation effects associated with drifts produce a decay over time of the Fe/O ratio, qualitatively reproducing that observed in SEP event profiles.

Key words. Sun: particle emission – Sun: heliosphere – Sun: activity

1. Introduction

While protons and electrons are the main species in solar energetic particle (SEP) events, often detected in the interplanetary medium following flares and coronal mass ejections (CMEs), ions with mass number $A > 1$ are also present. Heavy ion observations display a wealth of signatures that can be used to infer the properties of the acceleration and propagation processes acting on the particles before they reach an observer at 1 AU.

One of the observational signatures that is often emphasised is the temporal evolution of the Fe/O ratio: this ratio has been shown, by many observers, to decay over time over the duration of an SEP event (Scholer et al. 1978; Mason et al. 2006, 2012; Zelina et al. 2015). For an example of typical time profiles of Fe and O intensities and Fe/O ratio, see Figs. 1 and 2 of Mason et al. (2006). In many, so-called gradual, events, thought to be associated with acceleration at CME-driven interplanetary shocks, the Fe/O ratio at the beginning of the event can have values considered typical of flare-associated events, and decay over time to values near or below the typical average value for gradual events (Tylka et al. 2013).

Several different explanations for the observed Fe/O decay over time have been put forward. In the first reports of the effect, it was proposed that it results from the rigidity dependence of the scattering mean free path λ (Scholer et al. 1978), whereby $\lambda_{\rm Fe} > \lambda_{\rm O}$ due to the larger mass-to-charge ratio, m/q, of Fe in SEP events. In this interpretation, ions are assumed to be tied to the magnetic field line onto which they are injected: as a result, a single spatial variable, the distance travelled along the magnetic field line, is thought to be sufficient to describe propagation, so that the modelling is spatially 1D. A larger mean free path means that Fe ions arrive first at the spacecraft, so that their number is enhanced at the start of the event. A recent 1D focussed transport model including a mean free path proportional to $(m/q)^{1/3}$ was shown to reproduce the observed heavy ion ratio time variations in several SEP events (Mason et al. 2012).

Other authors have suggested that the temporal characteristics of Fe/O are a signature of the acceleration process. Cane et al. (2003) proposed that the high Fe/O ratio values at the beginning of an SEP event are due to a flare-accelerated SEP component, while later, lower values are due to SEPs accelerated by the CME-driven shock. A model of acceleration at a CME-driven shock in the presence of self-generated waves produced heavy ion profiles with a variety of temporal behaviours, similar to those observed in the 20th April 1998 event (Ng et al. 1999).

Mason et al. (2006) showed that when Fe intensity profiles at 273 keV nucleon^{-1} and 12 MeV nucleon^{-1} are compared with O profiles in channels with average energy per nucleon double that of Fe, the differences between Fe and O profiles, and therefore the decay in time of the Fe/O ratio, disappeared. They concluded that Fe/O decays are a result of interplanetary transport

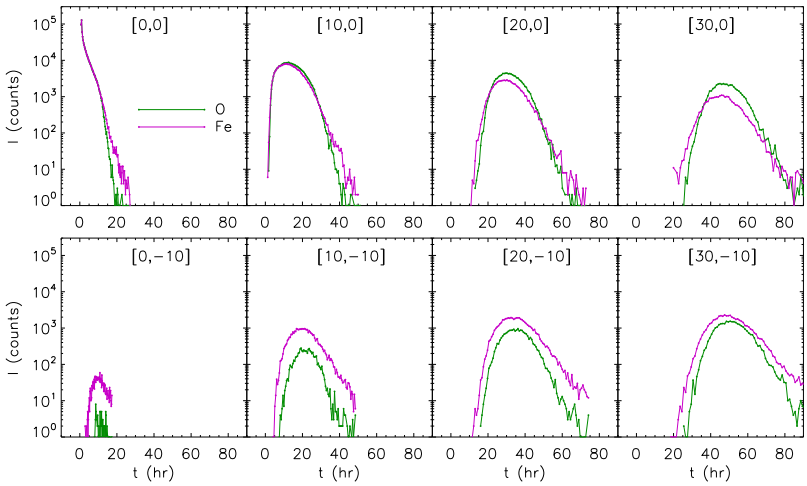

Fig. 1. Fe (*magenta line*) and O (*green line*) intensities versus time for the energy range 10–30 MeV nucleon^{-1} at various 1 AU locations relative to the magnetic field line connected to the centre of the injection region at the Sun. Labels in each panel give the observer's angular position as $[\Delta\phi_{1\ \mathrm{AU}}, \Delta\delta_{1\ \mathrm{AU}}]$, where $\Delta\phi_{1\ \mathrm{AU}}$ is the heliographic longitude and $\Delta\delta_{1\ \mathrm{AU}}$ the heliographic latitude relative to the position of the Parker spiral field line through to the centre of the injection region. Here $\lambda = 1$ AU. The same number of Fe and O ions were injected.

effects and cannot be explained by rigidity-dependent acceleration and release from the source region.

An analysis of SEP measurements at Ulysses and Wind (Tylka et al. 2013) showed that a qualitatively similar decrease in the Fe/O ratio can be detected at widely separated locations in interplanetary space. The authors concluded that the observed behaviour is the result of propagation effects.

In this paper, we study the propagation of partially ionised iron and oxygen SEP ions in a simplified model of the interplanetary magnetic field by solving their trajectories by means of a test particle code. Here all three spatial variables are retained in the description, making the modelling spatially 3D. Therefore, unlike traditional 1D models, we allow for the possibility that particles leave the field line on which they were initially injected. Our previous work has shown that, within a 3D model, particles experience transport perpendicular to the magnetic field due to drifts associated with the gradient and curvature of the Parker spiral magnetic field (Marsh et al. 2013; Dalla et al. 2013). Partially ionised heavy ions drift significantly more than protons (at the same energy per nucleon) due to their larger m/q. Here, for the first time, we derive the 3D propagation of Fe and O populations and study the Fe/O ratio at 1 AU as measured by several observers at locations of varying magnetic connection to the injection region. Some initial results related to this work were presented by Dalla et al. (2015b).

2. Simulations

Simulations are carried out by means of a 3D full-orbit test particle code, which integrates charged particle trajectories through a unipolar (outward pointing) Parker spiral interplanetary magnetic field (IMF; Marsh et al. 2013). Injection is instantaneous and from a compact region of angular extent $6° \times 6°$, located at $r = 2\ R_{\mathrm{sun}}$. The heliographic longitude and latitude of the center of the injection region are $\phi = 0°$ and $\delta = 20°$, respectively.

We inject the same number $N = 10^6$ of Fe and O ions. The measured charge states of Fe SEPs can vary within a relatively wide range of values, depending on the event. In the simulations presented here we chose a charge state for iron $Q_{\mathrm{Fe}} = 15$, while for oxygen $Q_{\mathrm{O}} = 7$, consistent with typical SEP measured charge states (Luhn et al. 1985). This gives mass-to-charge ratios $(A/Q)_{\mathrm{Fe}} = 3.7$ and $(A/Q)_{\mathrm{O}} = 2.3$. The injection spectrum of the heavy ions has a power law shape in energy per nucleon, with spectral index $\gamma = 1.1$, in the range 10–400 MeV nucleon^{-1}. Other parameters of the runs are the same as in Marsh et al. (2013).

Within our simulations, a low level of scattering is introduced, with a mean free path $\lambda = 1$ AU. The value of λ is the same for the different species, thus any rigidity dependence of the mean free path is neglected in our simulation. We do this deliberately to isolate the effects of drifts from those that would be caused by a rigidity-dependent mean-free path. No scattering across the magnetic field is present in our model.

Fe and O ion trajectories are integrated up to a final time $t_{\mathrm{f}} = 100$ h. Drifts due to the gradient and curvature of the Parker spiral magnetic field cause a significant fraction of particles to propagate outside the flux tube delimited by the corners of the injection region, experiencing transport perpendicular to the magnetic field (Marsh et al. 2013; Dalla et al. 2015a). Because of their larger mass-to-charge ratio ($(A/Q)_{\mathrm{Fe}} = 1.6\ (A/Q)_{\mathrm{O}}$), and consequently larger drift velocity at the same energy per nucleon, Fe ions move across the field more efficiently than O ions. Scatter plots showing the locations of Fe and O ions at the final time were presented by Dalla et al. (2015b).

Figure 1 shows profiles of Fe and O counts versus time for the energy range 10–30 MeV nucleon^{-1}, for several 1 AU observers. Labels in each panel specify the observer's angular location at 1 AU from the Sun as $[\Delta\phi_{1\ \mathrm{AU}}, \Delta\delta_{1\ \mathrm{AU}}]$, where $\Delta\phi_{1\ \mathrm{AU}}$ is the heliographic longitude and $\Delta\delta_{1\ \mathrm{AU}}$ the heliographic latitude relative to the position of the Parker spiral field line through to the centre of the injection region at the Sun. Therefore [0, 0] corresponds to an observer's location directly connected to the centre of the injection region, and the other panels correspond to less well connected observers. Panels to the right of [0, 0]

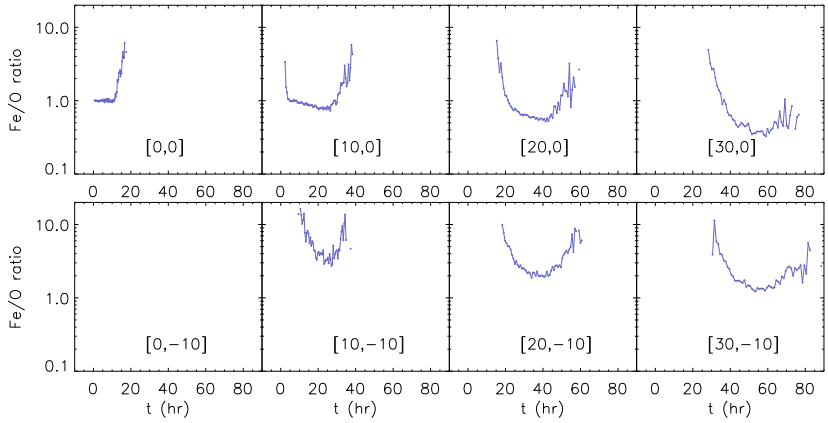

Fig. 2. Fe/O ratio versus time for the energy range 10–30 MeV nucleon^{-1} for the same 1 AU locations and parameters as in Fig. 1. The Fe/O ratio is calculated only for time intervals during which at least 10 Fe ions and 10 O ions were detected.

correspond to observers at the same latitude and more Western longitudes (i.e. the source region is more Eastern relative to the observer), and panels below them show observers at latitudes further south. The collecting area for each profile is $10° \times 10°$.

Figure 1 shows that significant heavy ion intensities are detected by observers that are not directly connected to the injection region (see all panels apart from [0, 0]). Hence, heavy ion propagation is taking place in 3D and not only along magnetic field lines, as is conventionally assumed. At the majority of not well connected observers, Fe arrives earlier than O due to its larger drift velocity at the same energy per nucleon. Fe also tends to peak earlier. One can see that moving from left to right in the top row of Fig. 1, peak intensities tend to decrease, while they increase going from left to right in the bottom row, corresponding to latitudes below that of the injection region. This behaviour results from drift in latitude which is downwards for the unipolar outward-pointing magnetic field used here (Marsh et al. 2013; Dalla et al. 2013).

Figure 2 shows the time evolution of the Fe/O ratio for the same locations and energy ranges as in Fig. 1. Here we can see that, at the majority of locations, the Fe/O ratio displays a decrease over time early in the event. It should be noted that since the same number of Fe and O ions are followed in our simulation, the injection Fe/O ratio is 1. In many cases, towards the end of the event, the Fe/O ratio displays an increase over time. This is due to the fact that the overall longitudinal extent of the flux tubes filled with O ions is smaller than for the case of Fe, due to smaller drift, resulting in a faster decay of O compared with Fe.

An important question is whether the overall qualitative behaviour shown in Figs. 1 and 2 for a mean free path $\lambda = 1$ AU will change for different scattering conditions. Marsh et al. (2013) analysed proton drift across the magnetic field for $\lambda =$ 0.3, 1 and 10 AU, and showed that drift behaviour is very similar in the three situations and therefore only weakly dependent on the scattering conditions. To study the effect of a different choice of mean free path on our results, we performed simulations of Fe and O propagation for $\lambda = 0.1$ AU for the same ionic parameters considered earlier. Figure 3 shows the effect of varying the mean free path on the 1 AU intensity profiles of Fe ions only, for four representative observer locations, where the green lines are for $\lambda = 0.1$ AU and the blue ones for $\lambda = 1$ AU. Here, one can see that for the well connected observer (the location indicated

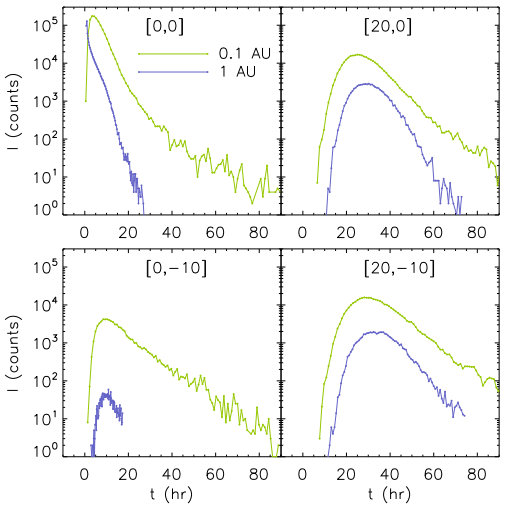

Fig. 3. Fe intensities versus time for $\lambda = 0.1$ AU (green) and $\lambda = 1$ AU (blue), for the energy range 10–30 MeV nucleon^{-1} for four representative 1 AU observer locations.

as [0, 0]), decreasing the mean free path produces a strong qualitative change in the intensity profile. The time of peak intensity is delayed and the slope of the decay phase becomes less steep, as is well known from 1D transport modelling. For the not well connected observers, the change in λ has a less pronounced effect on the overall shape of the profile and the main difference observed is the fact that the peak intensity is larger for $\lambda = 0.1$ AU, since particles remain close to the Sun for a longer time and have more time to drift across the field. The slope of the decay phase varies with λ less than for the well-connected case, and the time of peak intensity and start time of the event for $\lambda = 1$ AU are in some cases later than for $\lambda = 0.1$ AU, the opposite of what would be predicted by a 1D transport model. This is because in a 3D model, at locations other than [0, 0], the time variation of intensities results from the combination of drift, corotation, deceleration and scattering along the field line. The O intensity

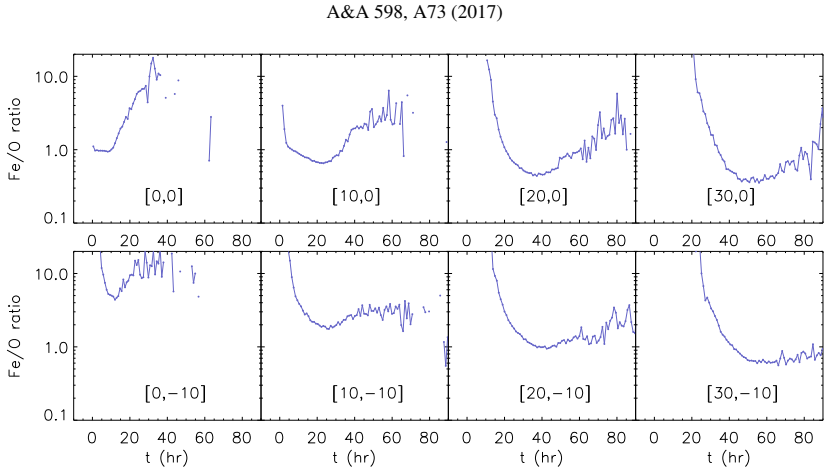

Fig. 4. Fe/O ratio versus time for the energy range 10–30 MeV nucleon^{-1} for the same 1 AU parameters as in Fig. 2 and mean free path $\lambda = 0.1$ AU.

profiles, not shown here, have a dependence on the value of the mean-free path similar to that shown in Fig. 3.

In Fig. 4 we present a plot of the Fe/O ratio for $\lambda = 0.1$ AU: here one can see that the qualitative trend of decreasing Fe/O, for observers not well connected in the initial phase of the event, is very similar to that in Fig. 2, where $\lambda = 1$ AU. This shows that within our 3D model the early temporal evolution of Fe/O at observers away from the well connected field line is not strongly affected by the scattering conditions, because it is dominated by drift effects. The increase in Fe/O seen late in the event in several cases for $\lambda = 1$ AU is no longer present for some of the observer locations for $\lambda = 0.1$ AU, due to the fact that both O and Fe fill a wider longitudinal region.

3. Discussion

In Sect. 2 we analysed the 3D propagation of SEP Fe and O ions through interplanetary space by means of a full orbit test particle model that naturally describes the effects of drifts on heavy ions. Fe and O were injected from a compact region at the Sun and propagated through a Parker spiral magnetic field in the presence of a low level of scattering. The ions were injected with charge states $Q_{\rm Fe} = 15$ and $Q_{\rm O} = 7$, resulting in significantly different mass-to-charge ratios.

Our results show that, for the same energy per nucleon range, Fe ions experience more drift than O. Both species are able to reach an observer not directly connected to the injection region, but Fe arrives and peaks first.

Consequently, the Fe/O ratio from our simulations decays over time, in a way that qualitatively matches the behaviour observed in SEP events (see e.g. Zelina et al. 2015). While Figs. 1 and 2 focus on the energy range 10–30 MeV nucleon^{-1}, the same qualitative behaviour is observed in all SEP energy ranges within our simulation. We also show that the chosen value of the scattering mean free path in the simulations does not significantly affect the observed trends, since drift is only weakly dependent on the scattering conditions (Marsh et al. 2013).

We conclude that propagation effects caused by drift are a possible cause of the observed temporal behaviour of the Fe/O ratio. Within the drift scenario, differences in the profiles of Fe and O are due to the 3D transport of these ions across the magnetic field, while in 1D models incorporating a rigidity-dependent mean-free path, they are caused by differences in the amount of scattering experienced while propagating along the field lines (Scholer et al. 1978; Mason et al. 2012). Overall, in SEP events, both rigidity-dependent mean-free paths and drift effects may combine to produce the observed decays of Fe/O, though our simulations show that, for an observer not well connected to the particle source, the drift effects are dominant.

The intensity profiles shown in Fig. 1 are shaped not only by the drift-dominated transport across the magnetic field, but also by deceleration taking place in the interplanetary medium. As discussed by Dalla et al. (2015a), drift-induced deceleration is present alongside adiabatic deceleration.

Mason et al. (2006) presented SEP observations showing that, while Fe and O intensity profiles in the same energy per nucleon range are rather different from each other, resulting in decaying Fe/O, the profiles become almost indistinguishable when O data with average energy per nucleon double that of the Fe channel are used in the comparison. In the latter case, the profile of Fe/O becomes flat. The authors interpreted this behaviour as resulting from the rigidity dependence of the mean free path along the magnetic field.

The observation could, however, also be explained as resulting from drift processes: drift velocities are proportional to the product $m_0\gamma v^2/q$ (Dalla et al. 2013), where m_0 is the rest mass, γ the relativistic factor and v the particle speed. For non-relativistic particles, drift velocities are proportional to AE/Q, where E is kinetic energy per nucleon. Therefore, for O ions, having lower A/Q than Fe, a larger value of E is required for the drift velocity to be comparable to that of Fe, so as to reach a not well connected observer in similar times. It should be noted that drift velocities in the Parker spiral field have a dependence on position within the heliosphere (Dalla et al. 2013), and particles of different energies propagate differently to a fixed radial distance from the Sun. Therefore it is not possible to immediately calculate the value of the energy per nucleon of O that will result in similar drift-dominated transport to an observer, and this value is not simply related to $(A/Q)_{\rm Fe}/(A/Q)_{\rm O}$ (parameter that, in our simulations, is 1.6).

To investigate whether our simulations support the above qualitative explanation and compare with the observations of Mason et al. (2006), in Fig. 5 we consider Fe profiles for the range 10–30 MeV nucleon^{-1} and O profiles in the range 30–50 nucleon^{-1}, at double the average energy. While there are some differences in the absolute values of the intensities, one can

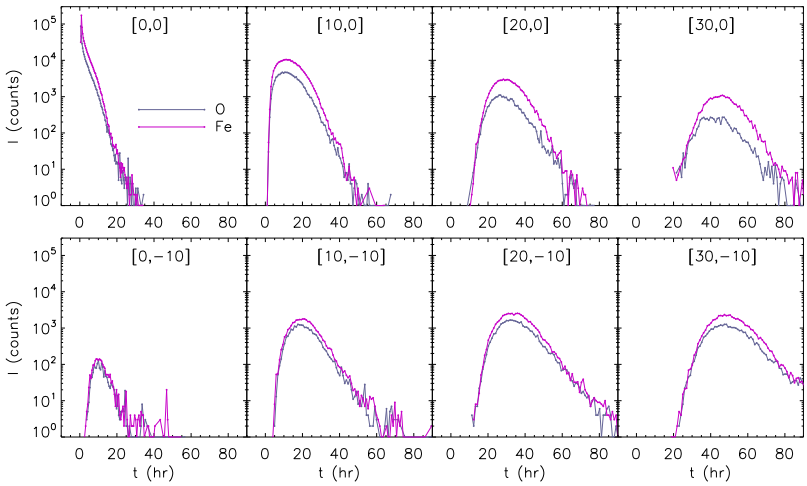

Fig. 5. SEP intensities versus time for Fe in the energy range 10–30 MeV nucleon^{-1} (magenta line) and O in the range 30–50 MeV nucleon^{-1} (blue line) for the same observer locations as in Fig. 1.

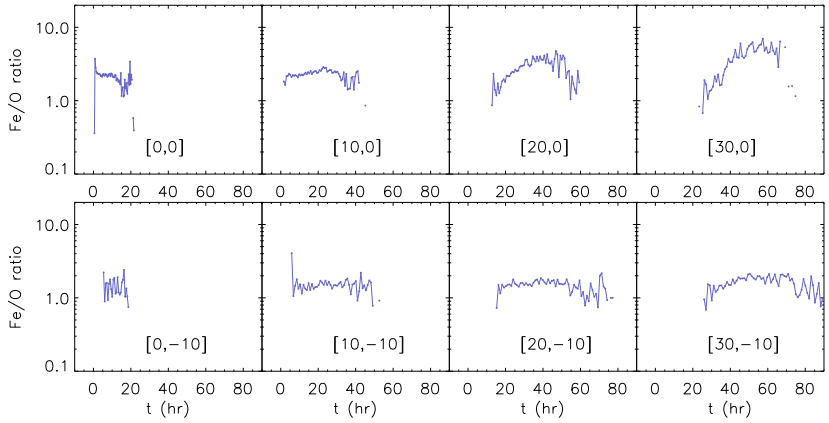

Fig. 6. Fe/O ratio versus time obtained by considering Fe in the energy range 10–30 MeV nucleon^{-1} and O in the range 30–50 MeV nucleon^{-1}, as in Fig. 5.

observe, by comparison with Fig. 1, that the difference in arrival time between Fe and O is no longer present. When the corresponding Fe/O ratio is calculated, as shown in Fig. 6, a decay in Fe/O is no longer visible, as was the case in the observations of Mason et al. (2006). Whether or not a completely flat profile is seen is dependent on the location of the observer.

4. Conclusions

Our simulations of SEP Fe and O propagation within a Parker spiral magnetic field in the presence of weak rigidity-independent scattering have shown the following:

- Significant drift is experienced by Fe and O ions away from the flux tube in which they were initially injected.
- Drift-associated propagation and deceleration result in a decay over time of the Fe/O ratio at a not well connected observer, in typical SEP energy ranges.
- The observation that the Fe/O decay is no longer present when O at double the average energy than that of Fe is considered, is reproduced by our simulations, showing that drift alone is sufficient to explain the effect.

We conclude that drift effects causing significant propagation across the magnetic field can qualitatively explain the observations of decaying Fe/O (Scholer et al. 1978; Mason et al. 2006, 2012; Zelina et al. 2015) and the disappearance of the decaying behaviour when higher energy O is considered (Mason et al. 2006). Therefore, here, we propose drift as a possible new mechanism that accounts for the observed features of Fe/O over time, alternatively to current models that explain them in terms of 1D rigidity-dependent propagation.

Our model contains a number of simplifications, which will need to be relaxed in future work to obtain a more realistic representation of SEP events. It will be necessary to move away from the simple unipolar IMF configuration and include two opposite polarities separated by a wavy heliospheric current sheet.

In addition, a model of field line meandering will need to be introduced (Laitinen et al. 2016), which most likely will have the effect of enlarging the range of heliolongitudes and heliolatitudes over which significant intensities are detected and ensuring earlier arrival times.

A simplification introduced in our simulations is the choice of a single charge state for each of the heavy ion species considered. We judged that this assumption allows us to visualise the qualitative behaviour of the Fe/O ratio in the clearest way. In reality, it is likely that Fe will be injected into the interplanetary medium with a range of charge states, although there is little observational information available on the charge profile at the acceleration site. In a related paper (Dalla et al. 2017) we analysed the propagation of Fe ions injected with a range of charge states and demonstrated that drift processes result in an energy distribution of charge states at 1 AU that increases with energy, as observed in many SEP events. Therefore, a single mechanism, drift, is able to explain both the time decay in Fe/O and the energy dependence of charge states at 1 AU, two key features of heavy ion SEP observations.

Acknowledgements. This work has received funding from the UK Science and Technology Facilities Council (STFC) (grant ST/M00760X/1) and the Leverhulme Trust (grant RPG-2015-094). S.D. and T.L. acknowledge support from ISSI through funding for the International Team on "Superdiffusive transport in space plasmas and its influence on energetic particle acceleration and propagation".

References

Cane, H. V., von Rosenvinge, T. T., Cohen, C. M. S., & Mewaldt, R. A. 2003, Geophys. Res. Lett., 30, 8017
Dalla, S., Marsh, M. S., Kelly, J., & Laitinen, T. 2013, J. Geophys. Res. (Space Phys.), 118, 5979
Dalla, S., Marsh, M. S., & Laitinen, T. 2015a, ApJ, 808, 62
Dalla, S., Marsh, M. S., Laitinen, T., & Zelina, P. 2015b, in International Cosmic Ray Conference, ed. A. van den Berg, Proceedings of Science
Dalla, S., Marsh, M. S., & Battarbee, M. 2017, ApJ, 834, 167
Laitinen, T., Kopp, A., Effenberger, F., Dalla, S., & Marsh, M. S. 2016, A&A, 591, A18
Luhn, A., Hovestadt, D., Klecker, B., et al. 1985, Int. Cosmic Ray Conf., 4, 241
Marsh, M. S., Dalla, S., Kelly, J., & Laitinen, T. 2013, ApJ, 774, 4
Mason, G. M., Desai, M. I., Cohen, C. M. S., et al. 2006, ApJ, 647, L65
Mason, G. M., Li, G., Cohen, C. M. S., et al. 2012, ApJ, 761, 104
Ng, C. K., Reames, D. V., & Tylka, A. J. 1999, Geophys. Res. Lett., 26, 2145
Scholer, M., Hovestadt, D., Klecker, B., Gloeckler, G., & Fan, C. Y. 1978, J. Geophys. Res., 83, 3349
Tylka, A. J., Malandraki, O. E., Dorrian, G., et al. 2013, Sol. Phys., 285, 251
Zelina, P., Dalla, S., & Laitinen, T. 2015, in International Cosmic Ray Conference, ed. A. van den Berg, Proceedings of Science